Author:
Reader, Madeleine J

Title:
Detection and quantification of volcanic ash for aircraft hazard mitigation

Detection and quantification of volcanic ash for aircraft hazard mitigation

By

Madeleine J. Reader

Supervisors: Matthew Watson, Richard Brooker, Rory Clarkson

School of Earth Sciences
University of Bristol

A dissertation submitted to the University of Bristol in accordance with the requirements of the degree of Doctor of Philosophy in the Faculty of Science.

October 2023

Word count: approx. 25,500

Acknowledgements

A PhD is project that is ultimately handed in and defended by only one person, but many people have been involved with its completion over the last four years.

To G32: Amelia, James, Joel, Katie, Lorena and Maddy, thanks for welcoming me into the office even though I arrived a year late, I was lucky there was a space left tucked away in the corner. Thanks again to Amelia for also being my fellow volcanologist in the office and for the many harbour walks, dinner club evenings and PhD chats, I know I've made a friend for life. Thank you also to the other volcanologists in the department: Alison, Pete, Sam, Alisa, Frankie, Mark, Stanley and Josh, it's been fun getting to be a part of this community in the last five years (and see all the cool research) and I hope to have the opportunity to return for volc coffee at somepoint. Charles and Gerald, your help was instrumental in the design of Ash Box 2, and it wouldn't have existed without your input. Thanks also for the more general talks about experimental design, they were always very useful. Thanks also to Stu for teaching me to use the SEM and for always being patient and helpful when I had questions. Thanks also to Mary for letting me demonstrate on Arran, those trips really helped remind me what I love most about being a geologist.

To my original volcano pals: Ash and Eva, I'm lucky to have remained friends with you over the years and to have had the opportunity to travel to amazing places with you both, due to our shared love for volcanoes. Eva, thank you also for the chats about PhDs, they helped me see the bigger picture. Ash, there's no one I'd rather listen to boygenius on loop with whilst driving around South Island.

To Sarah who's been my best pal since our very first geology lab at Edinburgh, thanks for constantly having my back and for always being available for long phone calls.

To Rory Clarkson, thanks for having me at Rolls-Royce and for all the interesting chats about ash and engines. I'm also looking forward to reading your book, the part I've already read has left me intrigued to know the rest of the story.

Thank you to Jonathan, Rachael and Kate for providing support and encouragement throughout the CDT process, and for making sure that biscuits were always available.

To my supervisor Matt Watson, who has been unfathomably kind, unwaveringly patient and unbelievably supportive; thank you for your guidance over the last five years and for taking me on as a student.

A big thanks also to my parents for continuously supporting me throughout my education. Thanks also to the Relphs for letting me work in the conservatory and to Midge and Edal for constant moral support.

Finally, thank you to Peter, you were the first person I met when I moved to Bristol, so you've really been here from the very start of this process. You've put up with my innumerable (daily in the last few months) PhD worries and for that I owe you many many thanks. I'm also lucky enough to now get to spend the rest of my life with you and I'm looking forward to where we go next.

Abstract

This thesis is focused on characterising volcanic ash clouds via the design of a novel ash-box in the laboratory and uncrewed aerial vehicle (UAV) flights which were carried out at Volcán de Fuego, Guatemala. Scanning electron microscope (SEM) stubs and an optical particle counter were used to look at particle distrubutions and concentrations in both situations, with the limitations of these sensors being explored. Using the ash-box allows particles to be contained within an enclosed space and their dispersion to be analysed, whilst also providing a testing place for sensors before deployment in the field. The UAV flights conducted at Volcán de Fuego collected data on the use of an aerodynamic baffle to enhance very fine particle (<1 micron) collection, and sampled both proximal and distal ash clouds. Never seen before, fast forming volcanic ash aggregates were also collected on two of the SEM stubs deployed at Volcán de Fuego. The potential processes involved in their formation are discussed, along with possible implications for ash dispersal models. Overall, combining laboratory techniques and the collection of in-situ data has led to new methods for understanding volcanic ash clouds. These sensors, or similar, could potentially be used by aircraft when in-flight to alert pilots to any potential dangers. Further understanding ash cloud characteristics is also beneficial to ash dispersal models, which can help prevent aircraft from coming into contact with harmful concentrations of ash.

Author's Declaration

I declare that the work in this dissertation was carried out in accordance with the requirements of the University's Regulations and Code of Practice for Research Degree Programmes and that it has not been submitted for any other academic award. Except where indicated by specific reference in the text, the work is the candidate's own work. Work done in collaboration with, or with the assistance of, others, is indicated as such. Any views expressed in the dissertation are those of the author.

SIGNED:..... DATE:.....

Contents

List of Figures

List of Tables

Chapter 1

Introduction

1.1 Ash Clouds and aviation

Characterising the properties of volcanic ash clouds is vital to the safety of aircraft, and to our understanding of ash dispersal. Volcanic eruptions can inject large quantities of ash into the atmosphere, making the risk to aviation from volcanic ash a world-wide hazard. A number of aircraft have had direct contact with volcanic ash and some of these encounters resulted in complete engine failure (Casadevall, 1994; Guffanti et al., 2009). Even if engines do not fail, significant damage can be done to engines, airframes and electronic systems which increases both risk of failure and the cost of ownership.

Whilst both remote sensing and dispersion modelling of volcanic ash clouds have decades of research, in-situ measurement does not. This is due to the inherent risks of entering an ash cloud which, until recently, required the use of crewed aircraft. The development of Uncrewed Aerial Vehicals (UAVs) has facilitated the detection, measurement and capture of ash within volcanic clouds.

Dispersion modelling requires a number of a priori assumptions and source terms (Mastin et al., 2009) of which the particle size distribution has the most control of the fate of volcanic ash particles (Beckett et al., 2015). Remote sensing can provide some of these source terms, including cloud height, mass eruption rate and, to a lesser extent, some indication of particle size and composition. However, neither remote sensing nor dispersion modelling can provide data in real-time and cannot determine the particle size distribution, complete compositional analysis and any analysis of other parameters that describe volcanic ash, such as shape, crystalinity or vesicularity. On-wing sensors could, and should, augment current research into

volcanic ash and could provide additional information to reduce the risk of ash to aviation in both real-time and after detailed analysis in the laboratory.

1.2 Motivation

The eruption of Eyjafjallajökull in 2010 led to loses within the aviation industry of values around $1.7 billion, as well as highlighting the lack of understanding around how much ash can enter a jet engine before there is the potential for serious consequences. These safety issues combined with financial loses if air space is closed for extended periods of time mean further research into the detection and quantification of volcanic ash is vital.

1.3 Thesis aims and outline

There are three main aims relating to this thesis:

1. To design a system capable of simulating an ash cloud in the laboratory, where multiple sensors can be tested. This will facilitate improved understanding about how ash-clouds behave as well as testing the abilities and limitations of the sensors present.
2. To collect in-situ data from an active volcano using a suit of sensors mounted on an unmanned aerial vehicle and to further develop methodologies for analysis of collected samples and their relationship to real-time observations.
3. To evaluate the properties of ash clouds which are able to be determined from the use of these sensors, and to investigate atmospheric process, such as aggregation, and the change in particle size distribution over time.

The following chapters of this thesis are outlined as follows:

Chapter 2: An overview of the literature related to these thesis aims covering jet engine damage, previous ash encounters, the properties of ash clouds, ash dispersion models, particle characteristics, and the use of uncrewed aerial vehicles at volcanoes.

Chapter 3: A "box" was designed in which to simulate an ash cloud in the laboratory. This was a two step process with a initial prototype being developed, followed by a more sophisticated final design, capable of running multiple experiments. A mini wind tunnel is used to fire samples

of ash from Volcán de Fuego, Guatemala, into the box, with a PMS5003 (an optical counter sensor) and SEM stubs, to characterise the properties of the generated ash cloud.

Chapter 4: This chapter examines in-situ data collected via uncrewed aerial vehicle (UAV) flights, carried out in January 2022. These data are a combination of SEM stubs and particle sensor readings, looking at characterising ash clouds in new ways.

Chapter 5: Unique small scale aggregates were found on Scanning Electron Microscope stubs flown through an ash cloud at Volcán de Fuego. They have been processed in order to examine individual particle size, starting from their core to rim. These fast-forming aggregates have provided insight into processes occurring within volcanic ash clouds and have potential implications for forecasting models.

Chapter 6: This final chapter summarises the thesis, drawing conclusions from the previous sections. It also suggests ideas for future work.

This thesis was also completed as part of the Centre of Doctoral Training for Aerosol Science, which involved a three month sabbatical at the University of Manchester. During this placement particulate matter data collected at an urban site in Manchester was analysed, in order to ascertain reasons for the observed trends. This work was completed as a written report which is included in Appendix A.

Chapter 2

Background

Volcanic ash is an aerosol which comes in many shapes and sizes as a result of the variety of composition and eruption dynamics present at volcanoes around the globe. These characteristics can influence the transport of particles within ash clouds, dictating how far they will travel and where they are likely to be deposited. Fine ash (< 63 μm) can be suspended in the atmosphere for days to months, compared to courser ash (> 63 μm) which tends to undergo sedimentation within hours (Vogel et al., 2017). Tephra is divided into the following four size categories: Bomb or block ($\geq$ 64 mm), lapilli (2 - 64 mm), coarse ash (0.063 - 2 mm) and fine ash ($\leq$ 0.063 mm) (Langmann et al., 2012). In this thesis very fine ash is also defined as particles being <10 μm in size.

Understanding and characterising ash clouds is of particular importance to the aviation industry, as it has the potential to cause problems on both short and long term timescales. When suspended in the atmosphere ingested ash particles can quickly cause full engine failure, due to the temperature of jet engines being above the softening point of volcanic ash. They can also close large areas of airspace for long periods of time creating ongoing problems for the airline industry and billions of dollars worth of loses. Furthermore, airfall can shut airports for extended periods of time.

There are usually around 40-50 active volcanoes around the world at one given time, meaning they pose a constant risk to aviation. There are areas of the world where frequent flights paths are over regions which have many active volcanoes capable of producing large ash clouds. Once it reaches the troposphere this ash also has the potential to remain suspended in the atmosphere for a prolonged period of time, forming layers that can be kilometers in height (Guffanti and Tupper, 2015). The demand for passenger flights and the number of aircraft in

the air is also expected to increase, putting further people at risk of being effected by volcanic ash.

2.1 Volcanic Ash Distribution

The distribution, residence time in the atmosphere and ultimately deposition of volcanic ash is dependent on various factors. These factors include the mass eruption rate, height of the eruption column, eruption duration (Mastin et al., 2009), meteorological conditions (Poulidis et al., 2018), and the size, shape and density of the individual ash particles (Folch, 2012; Beckett et al., 2015) (Figure 2.1). Size and shape of the particles is controlled by fragmentation process which occur during the eruption with analysis of particles post-eruption giving valuable insights into conditions within the volcano pre-eruption (Dellino et al., 2012).

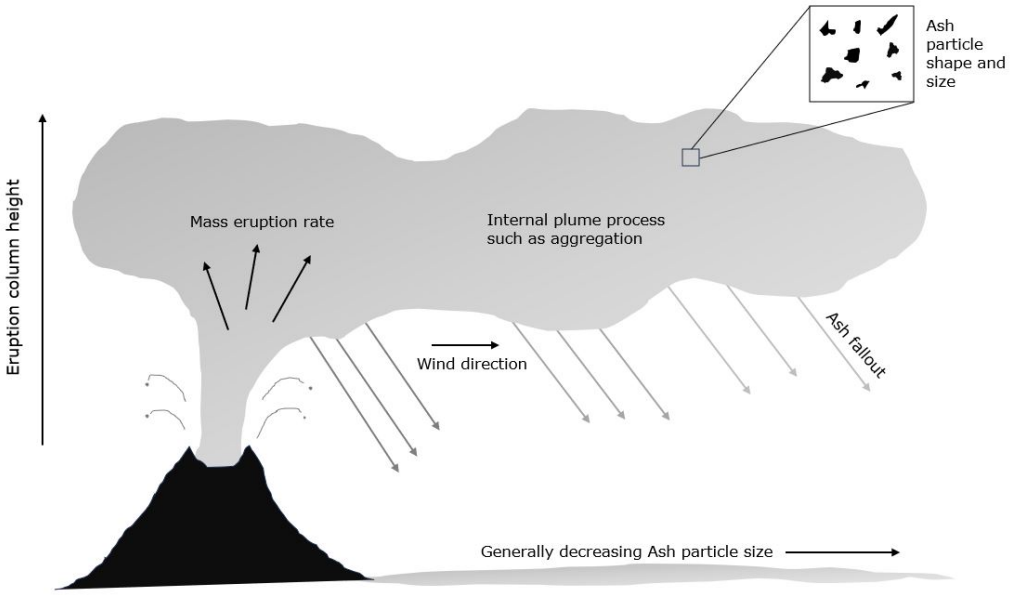

Figure 2.1: *This diagram highlights the main controls on volcanic ash dispersion: eruption column height, mass eruption rate, meterological conditions (wind direction), internal plume processes and, ash particle size and shape.*

The individual ash particle properties in turn effect the terminal settling velocity of a particle (Freret-Lorgeril et al., 2019) which helps to predict the thickness and location of ash deposits. Fine particles are able to be transported further as they have a lower terminal settling velocity, meaning they are more easily carried by any atmospheric wind (Dellino et al., 2012). Aggregation of ash particles can also play an important role in ash dispersal, with it potentially

causing premature removal of fine particles (Carey and Sigurdsson, 1982). The extent of aggregation within ash clouds is difficult to quantify though, with the nature of aggregation also potentially changing with distance from the eruption source (Brown et al., 2012). Also, not all aggregates which are produced within as ash cloud likely survive preservation on deposition, hence in-situ sampling of ash clouds is vital in order to help understand aggregation as an ongoing process.

2.2 Previous aircraft ash encounters

2.2.1 Damage to a Jet Engine

A jet engine consists of four major sections: the fan, the compressor, the combustor and the turbine (Figure 2.2). Air first enters the engine via the fan, then is passed into the compressor where pressure increases, with this high-pressure air then being ignited in the combustor before finally expanding and powering the turbine (Rolls Royce, 1996; Giehl et al., 2017). Temperatures within an engine can reach values as high as 2,000°C in the combustor region, which is above the softening point of volcanic ash, meaning if these particles are ingested they are able to become stuck to interior components and potentially block airflow (Song et al., 2016).

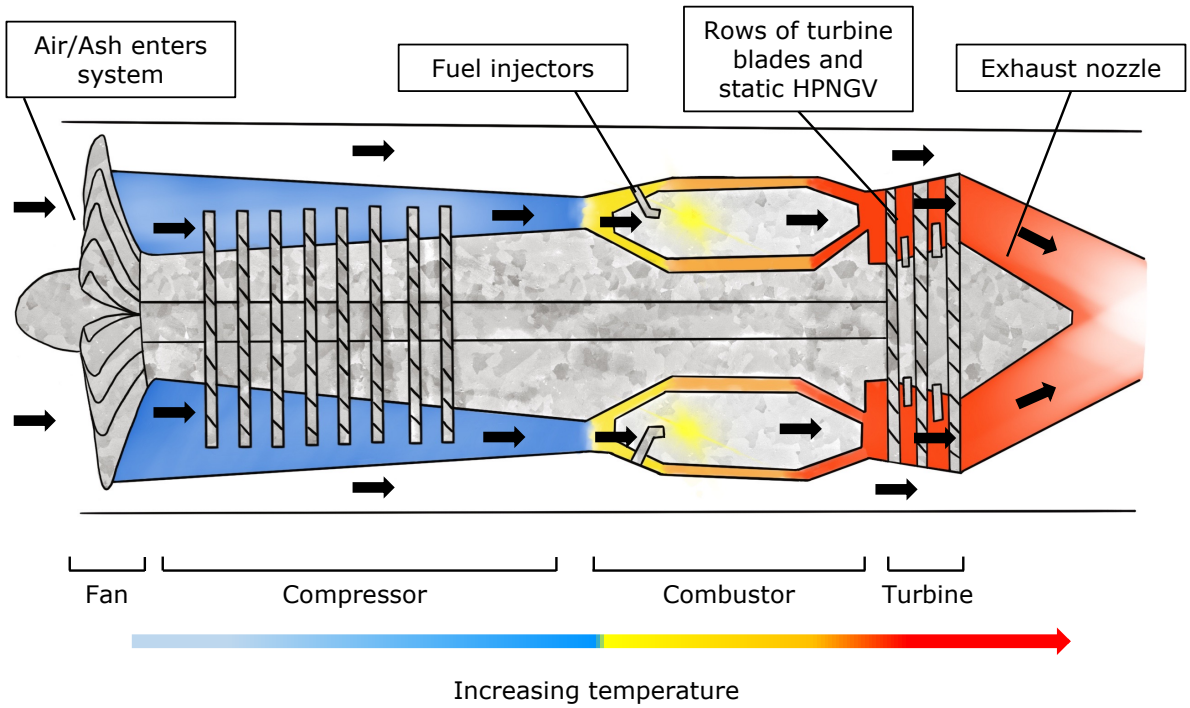

Figure 2.2: *A diagram of a turbofan jet engine showing the four major sections (fan, compressor, combustor and turbine), along with the black arrows showing the direction of air flow. Temperature increases through the engine, reaching it's peak in the combustor, however, due to their shape, HPNGVs are the area where ash deposits are most likely to build up.*

Rows of stationary high pressure nozzle guide vanes (HPNGVs) are used within the turbine to increase the speed of the high temperature/pressure gas and control its direction towards the blades (Chaharlang et al., 2019). The HPNGVs are particularly vulnerable to molten volcanic ash due to their unique curved shape, which is important to the performance of the engine; but if ash builds up in this area, restricting air flow, it can cause an engine to surge (Przedpelski and Casadevall, 1994; Pearson and Brooker, 2020). This surge can then further result in a loss of a power to the engine. In jet engines used today metal components in the highest temperature regions are also usually protected by thermal barrier coatings (Song et al., 2019; Müller et al., 2021a). However, due their rough texture, these thermal barrier coatings also potentially increase the ability of volcanic ash to stick to the inside of the engine (Pearson and Brooker, 2020; Müller et al., 2021b).

2.2.2 Examples of Engine Failure

There are two well-known encounters of volcanic ash with aircraft: Mt Galunggung (Indonesia) in 1982 (flight BA009) and Mt Redoubt (Alaska) in 1989 (flight KLM867). In both instances the aircraft involved was a Boeing 747, with four turbofan engines. The encounter over Indonesia in 1982 on the 24th of June resulted in power loss to all four engines at 37,000 ft (Webley and Mastin, 2009). However, on descent to 13,000 ft the engines were restarted in succession and three managed to restart, with one being shut down again due to a surge (Johnson and Casadevall, 1994). The plane then made a safe landing in Jakarta using the three working engines. There was also significant damage to the windscreen, making visibility from the cockpit difficult (Dunn, 2012). On this occasion, the pilots were unaware what had caused the engine failure and only once the plane was examined on landing, was it confirmed to have flown through an ash cloud (Prata and Tupper, 2009). This could be a result of the incident happening at night, meaning the ash cloud was not visible.

During the Mt Redoubt encounter on the 15th of December 1989, the aircraft lost power to all four of its engines at 27,900 ft after entering a climb in order to avoid the ash cloud (Davison and Rutke, 2014). After gliding for 4 minutes and reaching 17,200 ft, two engines were restarted and then finally at 13,300 ft the final two engines were turned on again and the plane landed safely in Anchorage 30 minutes later (Kienle et al., 1990; Casadevall, 1994; Waythomas et al., 1997). There were other encounters with the ash cloud on the same day and the following day, but there were no further engine failures.

The conventional wisdom around how jet engines manage to restart as a result of losing power is that on cooling, the ash sheds from the engine components, clearing blocked channels and allowing air flow. However there is little evidence that this is the case; the most likely reason that these engines were able to restart in both occurrences is that the descent of the aircraft meant it entered denser air, allowing the combustor to produce a stable flame (Clarkson and Simpson, 2017).

In both cases, the planes managed to land safely with no fatalities. However, these situations highlight the importance of understanding how volcanic ash interacts with jet engines, to prevent any future incidents leading to engine failure.

2.2.3 The 2010 Eyjafjallajökull Eruption

Despite the volcanological and aviation community having been aware of the hazards pose to aircraft from ash since the 1980s, the 2010 eruption of Eyjafjallajökull was a turning point for volcanic ash and aviation. The no fly zone implemented across most of European airspace resulted in losses to the aviation industry of $1.7 billion (Mazzocchi et al., 2010; Budd et al., 2011; Ulfarsson and Unger, 2011; Schmitt and Kuenz, 2015) along with millions of displaced passengers (Bolić and Sivčev, 2011). The eruption itself began as a new fissure, which opened up on the 20th of March, stopped on the 12th of April and did not prompt any airspace closure (Gudmundsson et al., 2010). However, on the 14th of April, there was an explosive eruption beneath the ice cap covering the volcano, which generated large volumes of fine-grained ash ($\leq$ 63 μm) (Petersen, 2010). An estimated 8.3 Tg of ash in the size range 2.8 - 28 μm being released (Stohl et al., 2011). This, combined with the prevalent north-westerly winds blew the material across Europe (Prata and Rose, 2015). During the eruption there was a total of 91 recorded instances of aircraft coming into contact with ash (Christmann et al., 2017), none of which resulted in engine failure.

Re-opening European airspace after the eruption was a complicated problem involving many stakeholders across a range of sectors, such as individual airlines, government institutions and engine manufactures (Reichardt et al., 2018). The International Civil Aviation Organization (ICAO) had a policy before the 2010 eruption of Eyjafjallajökull of any ash in the atmosphere being unsafe for aircraft (Woodhouse et al., 2013). As a result of the crisis which occurred after the eruption, a "Safe to Fly" chart was designed, which suggested that engines could withstand 2 mg/m^3 of ash for 2 hours (Clarkson et al., 2016). This led to flights resuming across most of Europe, and helped to end the crisis caused by the eruption. The values for the "Safe to Fly" chart were reached by examining photographs and written documents from past encounters, as well as reassessing strip reports from the BA009 and KLM867 encounters which allowed a greater understanding of how much ash was ingested and over what time frame damage occurred (Clarkson et al., 2016). This chart was then modified to show exposure duration vs ash concentration (Figure 2.3), to clearly define the maximum amount of time a plane can spend in an ash cloud of known concentration, along with where previous examples of aircraft encounters with ash fit within these bounds. There are large uncertainties associated with past eruption concentrations due to a lack of data, however duration of exposure is relatively well defined from pilot reports and ash dispersion models. The UK Civil Aviation Authority

(CAA) now has three defined levels of ash contamination to airspace: low (> 0.2 - < 2 mg/m^3), medium (> 2 - < 4 mg/m^3) and high (> 4 mg/m^3), with planes being allowed to operate in low conditions but requiring a safety case to be raised to fly within medium and high contamination areas (Civil Aviation Authority, 2015).

The Safe to Fly chart, does not consider the different compositions of volcanic ash (basaltic - rhyolitic), and there is increasing evidence that this has a significant impact on how well particles adhere to the engine components (Giehl et al., 2017; Pearson and Brooker, 2020).

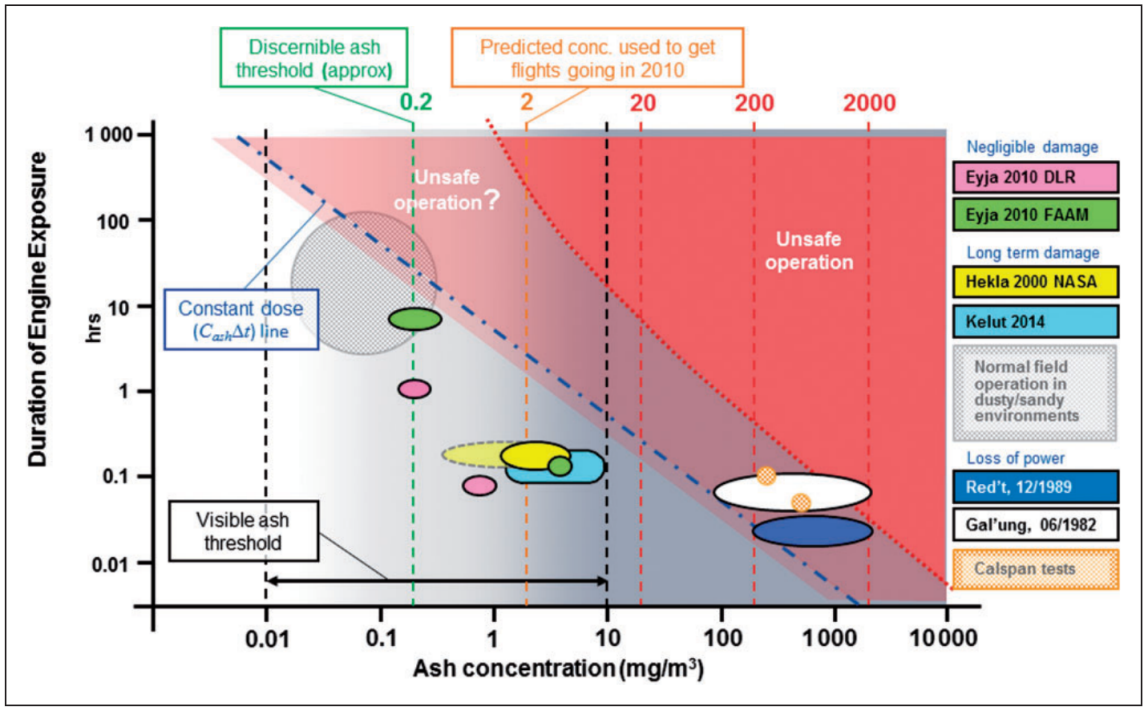

Figure 2.3: *The duration of exposure vs ash concentration chart (Clarkson et al., 2016), modelled off the Safe to Fly chart, shows the areas of unsafe operation as a function of duration versus ash concentration. The large ovals show the uncertainly associated with the ash concentrations of previous encounters, with the duration of exposure being relatively well defined, compared to ash concentration.*

Vehicle Integrated Propulsion Research (VIPR) III tests carried out in 2015, fired Mazama ash (ranging from 5 - 60 microns) into a jet engine retired from service, at speeds similar to those experienced in the atmosphere (Simon et al., 2015). Although these tests showed the build up of volcanic deposits on HPNGV, the reliability of the results are questioned as the ash had been collected from old deposits (Pearson and Brooker, 2020).

A Severity Index relating to ash encounters was developed which ranges from class 0

(ash reported by crew but no obvious damage) to class 5 (full engine failure leading to the aircraft crashing); within 1000 km of the source volcano the vast majority of encounters are above severity class 2 (Christmann et al., 2017).

Out of the 94 certain encounters of aircraft with ash from 1953 to 2009, there were 79 instances where there was some sort of damage to the plane or engine, nine of these resulted in engine failure mid-flight (Guffanti et al., 2011). Out of these nine flights, the longest time spent in the ash cloud was 13 minutes and the shortest just 2 minutes. From 2010 to 2016 there were 122 incidents; 22 of them caused damage to the plane (Christmann et al., 2017). Despite engine failure and damage, no fatalities have been associated with any of these incidents.

2.2.4 Volcanic Ash Advisory Centres

As a result of the significant encounters of aircraft with volcanic ash in the 1980s, Volcanic Ash Advisory Centres (VAACs) were created in the 1990s to prevent planes from coming into contact with dangerous concentrations of ash (Igarashi et al., 2018; Mastin et al., 2022). They act as a bridge between meteorological institutions, volcano observatories and airport air traffic control (Webley and Mastin, 2009). When there is a volcanic eruption that disperses ash into the atmosphere the VAAC for that region produces regular forecasts showing the likely trajectory of the particles. This involves the production of graphics and advisories which can show the location of volcanic ash up to 18 hours before it reaches the predicted area (Beckett et al., 2020). VAACs gather data from various sources (satellites, pilot and ground reports) and use atmospheric dispersion models to generate forecasts (Millington et al., 2012). Anchorage, Buenos Aires, Darwin, London, Montreal, Tokyo, Toulouse, Washington and Wellington are the nine functioning VAACS covering the entire globe (Figure 2.4). In the case of the 2010 eruption of Eyjafjallajökull, the London VAAC was responsible for updating the movement of the ash cloud, and they used the Met Office's Numerical Atmospheric-dispersion Modelling Environment (NAME) model in order to carry this out (Langmann et al., 2012).

Figure 2.4: *A projection showing the boundaries of the 9 VAACs around the globe.*

2.3 Aircraft and Ash Detection

2.3.1 Ash cloud properties and dispersion models

Understanding how ash disperses through the atmosphere is extremely important in aircraft hazard mitigation, due to the fact that ash cloud properties such as composition, particle size and concentration can all have an effect on the overall damage to a jet engine. Other factors such as ash aggregation within the cloud, which can change the particle size distribution, are also important to consider. Ash dispersion models will use a combination of factors to best predict the movement of an ash cloud including the eruption parameters, weather conditions and particle characteristics (Folch, 2012). Combining ash dispersion models with flight paths has also shown that effective re-routing can occur, in order to minimise the loses to the aviation industry and allow flights to continue in the crowded European airspace (Hirtl et al., 2020).

The NAME model, originally designed for modelling the spread of radioactive particles was first operational in 1988, having been developed as a result of the power plant incident at Chernobyl in 1986, however, it is now also used by the Met Office to simulate the dispersion of volcanic ash (Jones, 2004; Jones et al., 2007). The model is reliant on accurate input parameters

including; volcano location, eruption length, mass eruption rate, height of the plume, and particle properties including shape, size and density (Harvey et al., 2018; Saxby et al., 2020b). This is combined with meteorological data to produce an ash forecast. Initial particle size distributions which used in the model are critical to predicting how far particles will travel: 30μm diameter particles potentially travel five times further than a 100μm diameter particle (Beckett et al., 2015). Currently the model uses one of three standard particle size distributions (default, coarse or fine) (Figure 2.5), with coarse and fine options being introduced after the 2010 eruption of Eyjafjallajökull, and being based on the 1991 eruption of Hekla and 2010 eruption Eyjafjallajökull, respectively (Beckett et al., 2020). However with enough empirical data collected throughout an eruption, this can be altered as the volcanic event progresses (Witham et al., 2012). Only basing particle size distributions on ground collected samples, can also generate less accurate model results, as the smallest particles are potentially missing (Wilkins et al., 2016; Osman et al., 2020). The NAME model, when used in 2010, assumed all particles were spherical (Beckett et al., 2020), however, ash dispersion is sensitive to particle shape particularly for particles larger than 100 μm and in a vertical extent, with non-spherical particles having the ability to travel much further (Saxby et al., 2018). An aggregation scheme, developed for use with NAME, is sensitive to both particle density and the initial grain size distributions (Beckett et al., 2022).

Other VAACs use models such as MEDIA, CANERM and HYSPLIT to produce ash dispersion forecasts and, despite their different input parameters, they have been shown to generate closely aligned results when compared to one another (Witham et al., 2007).

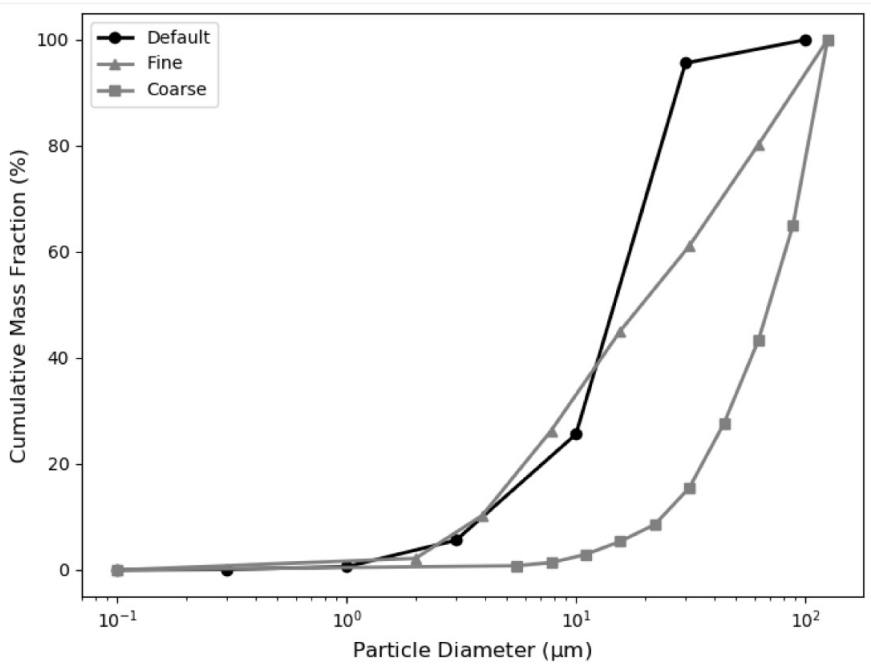

Figure 2.5: *This graph taken from Beckett et al. (2020) shows the three initial particle size distributions used in the NAME model: default, fine and course.*

2.3.2 Ash Particle Shape and Size

Defining the characteristics of an ash particle can be difficult due to their complex and variable shape; which is primarily a result of the eruption style which occurred when they were formed. There are many different parameters which can be used to describe the 2D shape of an individual particle, including maximum/minimum ferret diameter, convex hull perimeter, best-fit ellipse major axis, area-equivalent diameter and its bounding rectangle length (Riley et al., 2003; Liu et al., 2015) (Table 2.1). Choosing the best parameters to use is tied to the particles being examined and evaluating their shape, as there is no single best accepted parameter. Sometimes more than one parameter is needed to accurately quantify ash shape and size as it can show the irregularities associated with particle outlines (Liu et al., 2015). Using techniques such as X-ray computed tomography also allows the examination of particles in 3D (Saxby et al., 2020a). Ash shape is also a key parameter when evaluating the effect of abrasion on aircraft, with the sharpness of the particles potentially being more significant than the mass (Gislason et al., 2011). Aircraft are also more likely to come into contact with particles <100 μm as these will travel further from their source, with flight paths unlikely to be closely intersecting with volcanoes which are actively erupting large volumes of ash.

Particle Parameter	Description
Max Ferret Diameter	The longest particle axis between two parallel lines
Min Ferret Diameter	The shortest particle axis between two parallel lines
Convex hull Perimeter	The total length of lines drawn between the particles edges
Best-fit ellipse major axis	The longest axis of a best fit ellipse of equal area
Area-equivalent diameter	The circle equivalent diameter of the particle area
Bounding rectangle length	The length of a rectangle bounding the particle

Table 2.1: *Parameters often used to describe ash particles, adapted from Liu et al. (2015)*

Choosing which parameters to use when deciding how best to quantify ash particle size is an important consideration, and is often decided based on the shape of the ash particles being analysed (Riley et al., 2003). As previously mentioned though, initial grain size distributions play an important role when forecasting ash dispersal, with fine particles (<30 μm) travelling greater distances than those greater than 100 μm. There is evidence than individual ash particle composition (glass/crystal), can impact how far a particle will travel, however this is also linked to ash shape and density (Hornby et al., 2023). Generally though, volcanoes which produce basaltic, low-silica ash release a considerably lower percentage of fine (<4 μm), when compared to those of a andesitic or dacitic composition Horwell (2007).

2.3.3 On-wing ash monitoring devices

One solution to the problem of unknown in-flight atmospheric properties is external sensors on aircraft. On-wing devices can obtain real-time data, which helps inform pilots of current air conditions. Currently, other than what is visible, pilots have no way of knowing whether they have entered a volcanic ash cloud, or knowing the concentration of ash within the cloud through which they are flying (Liang and Xu, 2021). Such devices are particularly useful at night, when it is difficult to see ash in the atmosphere (Weinzierl et al., 2012). Many serious incidents associated with volcanic ash have occurred at night. Optical particle counters (OPCs) have been seen as a favourable instrument for on-wing use, as they usually have a lightweight design and produce concentration values which can be compared to the Safe to Fly chart (Eliasson et al., 2016). Collecting in-situ measurements can also confirm whether ash dispersion models are accurate, and help improve future model iterations. These measurements can also be used

to update ongoing eruption parameters (Witham et al., 2012).

The airline industry has often used the criteria of "avoiding visible ash" to prevent pilots from encountering ash clouds (Clarkson et al., 2016). However, during daylight hours there are multiple variables determining how easy it is to identify particles in the air: particle shape, particle size, particle concentration, and the colour contrast between the ash particles and their background are all important factors that influence whether pilots can see volcanic ash (Weinzierl et al., 2012). As well as ash properties being important, the colour of the background itself can improve or reduce ash visibility, with both the presence of meteorological cloud or flying over a large urban area having an influence. Human factors such as whether a pilot has encountered volcanic ash in the atmosphere before, or been trained on detection, can also affect the ability of pilots to observe and avoid ash clouds.

Whilst ash continued to disperse around Europe in April-May 2010 during the eruption of Eyjafjallajökull, 12 manned flights were carried out by the UK facility for Airborne Atmospheric Measurements (FAAM) to collect in-situ information about the volcanic ash cloud (Johnson et al., 2012; Dacre et al., 2013). Johnson et al. (2012) found that the majority of ash particles that reached European airspace, at altitudes between 2-8km, were in the size range of 1 - 10 μm, with a brief peak in concentrations between 2000-5000 $\mu m/m^3$. The graph in Figure 2.6, taken from Turnbull et al. (2012), highlights the abundant presence of material detected during these FAAM flights which is <10 μm in size. Very fine particles are transported the furthest from source, and represent a significant hazard to aircraft.

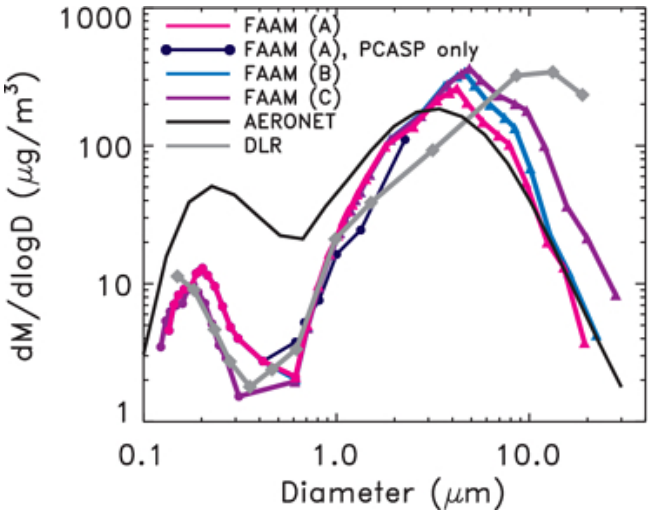

Figure 2.6: *This graph highlights the extensive detection of particles <10 μm in size, with a peak in measurements at a 6 μm diameter, during the FAAM flights conducted over European airspace (Turnbull et al., 2012).*

A total of 17 flights in planes with a piston motor engine occured over Germany by the Duesseldorf University of Applied Sciences during the eruption, as well as over western Iceland with the University of Iceland (Weber et al., 2012). Some of the latter flights directly entered the eruption plume. The onboard OPC found similar particle concentrations as those predicted by the London VAAC over Germany, however there was evidence for the presence of discrete layers within the ash cloud; the flights which directly entered the plume in Iceland found peak concentrations of 2000 μg/m^3 (Weber et al., 2012; Eliasson et al., 2016). These flights also found that ash plumes were just visible when slanted during daylight hours at concentrations below 0.1 μg/m^3 (Schumann et al., 2011).

The data collection campaigns were valuable for collecting in-situ data during the 2010 Eyjafjallajökull eruption to confirm model outputs, however there were safety concerns as the aircraft entered areas that had potentially higher ash concentrations than the recommended levels (Turnbull et al., 2012). This meant that they were restricted to areas with lower concentrations (Beckett et al., 2015).

In 1978, eleven pioneering flights were carried out over three volcanoes (Fuego, Pacaya and Santiaguito) in Guatemala, collecting in-situ gas measurements as well as individual ash particles, which reached sizes down to <1 μm (Cadle et al., 1979; Rose et al., 1980). These early studies into the ash particles emphasised the need to study in-situ fine particles (< 20 μm), which can be difficult to sample once deposited. The ash cloud from the 1980 eruption of Mount

St. Helens was also sampled with crewed aircraft, and collected volcanic gas measurements and individual ash particles ((Chuan et al., 1981; Farlow et al., 1981; Bandy et al., 1982)). The flights sampled distal clouds over Montana, and directly over the crater of Mount St. Helens.

2.4 The use of uncrewed aerial vehicles (UAVs) in remote sensing at volcanoes

2.4.1 Types of UAVs

UAVs can be divided into four categories: fixed-wing, single-rotor, multi-rotor and hybrid models (vertical take off and landing) (Figure 2.7).

Fixed-wing aircraft generally have the advantage of being able to travel large distances efficiently (up to approximately 15 km) and complete longer flight times (as long as 60 minutes) (James et al., 2020). They are however limited by the need for a clear, long, runway for take-off and landing, and their inability to hover (Tmušić et al., 2020). They are harder to pilot, and require more skill and training to safely complete take-off and landing. Single and multi-rotor UAVs have a shorter battery life but can carry heavier payloads and perform a stationary hover (Antoine et al., 2020; James et al., 2020). Multi-rotor UAVs also can come in a variety of sizes, with small systems becoming increasingly available and popular for use in volcano monitoring due to their ease of use and portability (Jordan, 2019). Relatively new hybrid UAV models have fixed wings for when they are in-flight but use rotating propellers to allow a stationary hover along with a vertical take-off and landing (De Wagter et al., 2018), eliminating the need for a runway, which is particularly useful in some locations due to access to a runway being challenging. This combines the benefits of an increased flight time and speed from a fixed wing aircraft, with the hovering abilities of a single/multi-rotor unit (David et al., 2021). Most UAVs are powered by batteries, however, some are driven by combustion engines (e.g. Yamaha RMAX-G1, (Ohminato et al., 2017)), which can carry heavy payloads but have the disadvantage of causing potential data contamination, especially when sampling volcanic gases (Kazahaya et al., 2019).

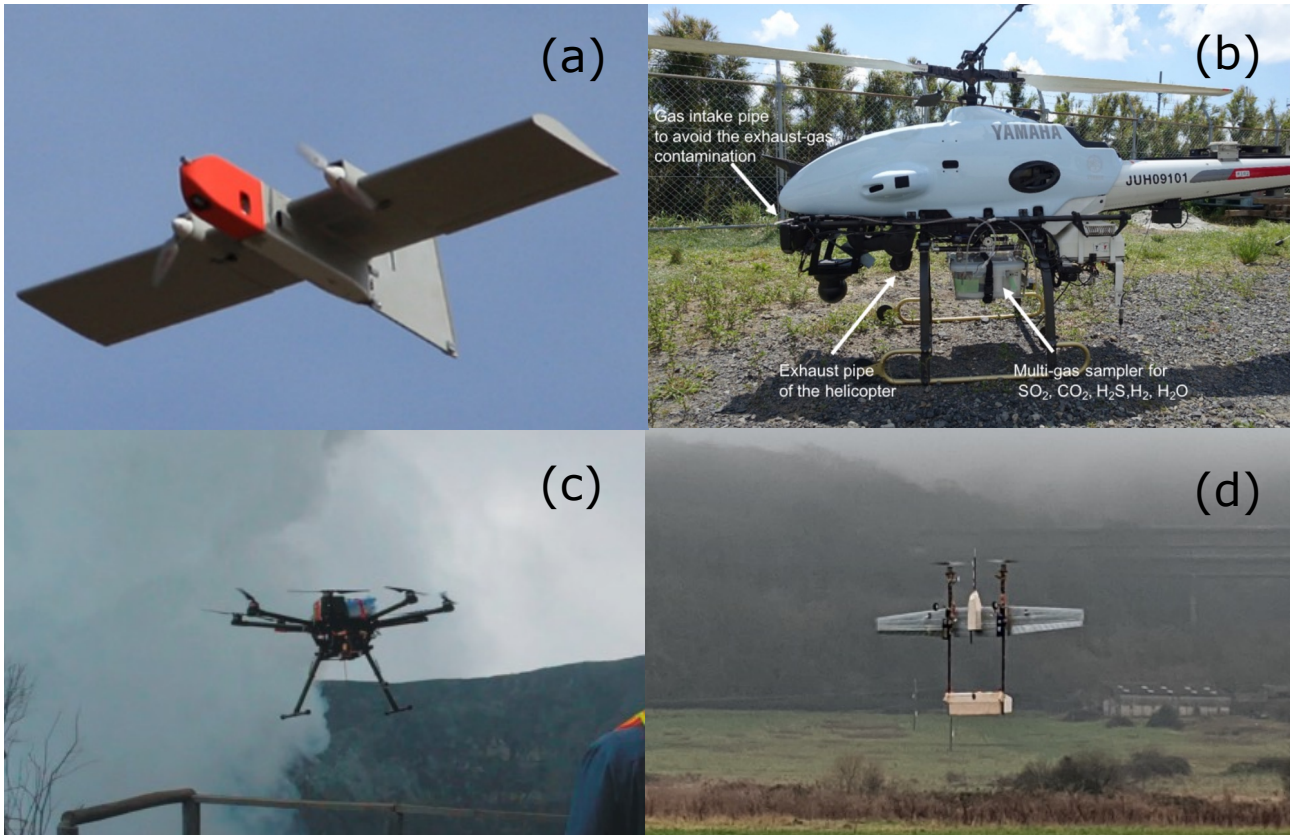

Figure 2.7: *(a) A fixed-wing NASA Dragon Eye (Pieri et al., 2013) (b) A single-rotor combustion powered Helicopter Yamaha RMAX-G1 (Ohminato et al., 2017) (c) A multi-rotor DJI S1000 octocopter (Stix et al., 2018) (d) The hybrid system BUDDI (Bristol University Drone Design Initiative) (David et al., 2021).*

2.4.2 Data Collection Via UAVs

UAVs allow the collection of real-time data close to erupting volcanoes, with minimal risk to individuals involved (Liu et al., 2019). They can carry payloads both horizontally and vertically, and transport them a range of distances, during flights lasting hours to minutes. One of the earliest uses of a UAV for volcanological monitoring was at Vulcano in Italy, where a single-rotor UAV was used to collect in-situ measurements of carbon dioxide and sulphur dioxide emissions (McGonigle et al., 2008). Since then the use of UAVs at volcanoes has increased dramatically and they have been used for wide applications such as water sampling (Terada et al., 2018), thermal infrared imaging (Wakeford et al., 2019), and high resolution digital elevation model (DEM) creation (De Beni et al., 2019). UAVs also can collect in-situ airborne particles (Schellenberg et al., 2019b), that are otherwise unobtainable due to their proximity to the eruption source. This is advantageous to understanding volcanic plume

properties because ground samples may exclude certain particles which travelled further, or were deposited sooner, and therefore do not give an accurate representation of the distribution within the original plume. UAVs have also been used to reestablish monitoring equipment on the ground where it has been destroyed by an eruption and access is unsafe (Ohminato et al., 2017). The combination of measurements taken from ground monitoring and UAV systems can also offer new insights into ongoing processes at volcanoes (Pering et al., 2020).

Collecting data using UAVs can also be separated into the categories of Visual Line of Sight (VLOS) and Beyond Visual Line of Sight (BVLOS), with the later usually requiring higher permissions from local governments or organisations to be undertaken (Terkildsen et al., 2021). The UK CAA, for example, has restrictions in place that mean all UAVs must fly below 120 m and remain in visual line of sight at all times. Flyer IDs are required for UAVs over 250g (Civil Aviation Authority, 2023).

Most UAVs use the global navigation satellite system (GNSS) to navigate and record the time at which data is collected. Accuracy is dependant on what is being surveyed (James et al., 2020). UAVs can be pre-programmed with flight paths using way-points, which help to reduce pilot error and allow missions to be pre-planned (Bonali et al., 2019; De Beni et al., 2019). There are a range of mission planning packages (e.g. Mission Planner, Pix4Dcapture, DJI GS Pro), depending on the type of UAV and the application (James et al., 2020; Tmušić et al., 2020). Another aspect to consider when collecting in-situ data close to volcanoes is that when mounted on a drone and flown through an ash cloud sensors can be exposed to many environmental extremes including high temperatures, corrosive gases and particles, and unpredictable winds (Jordan, 2019; Schellenberg et al., 2019a; Brosch, 2022). Weather conditions also have to be favourable for data collection as poor circumstances can cause damage to UAVs systems and potential loses.

2.5 Conclusions

Volcanic ash poses a constant threat to aircraft, with past encounters confirming that it has the potential to cause damage along with full engine failure, endangering the lives of the pilots and passengers on board. It is well understood that this happens as a result of volcanic ash reaching temperatures above its melting point in the combustor and then building up on components within the turbine, eventually restricting airflow within the system.

The eruption of Eyjafjallajökull in 2010 was a catalyst in the last ten years for further research on how volcanic ash effects jet engines and mitigation strategies, due to the wide problems it caused across the busy European airspace. However, with the continued risk of further eruptions effecting large areas of air traffic there is still a need for research efforts into this area. Examples of direct research outputs from the eruption of Eyjafjallajökull include the development of the "Safe to Fly" chart (Clarkson et al., 2016), which incorporates an increased understanding of engine tolerance to ash, along with the inclusion of fine and coarse particle distributions within the NAME model (Beckett et al., 2020).

Ash dispersion models are reliant on a thorough understanding of initial ash cloud properties when a volcano erupts, along with how these properties can evolve with time from an eruption. How to incorporate aggregation into these models is also still poorly understood with potential solutions only beginning to be developed, due to the complex nature of understanding how and when particles aggregate within the plume. If the location of volcanic ash in the atmosphere can be narrowly defined, then flights could be re-routed rather than airspace having to be closed or restricted.

Although on-board sensors located on manned aircraft were useful in analysing the spread and concentration of the ash cloud during the 2010 Eyjafjallajökull eruption, they also highlighted the risk posed to aircraft and potentially put people in a dangerous environment.

The use of UAVs to complete volcanological field work has increased exponentially over the last 10 years, due to their ability to collect in-situ data from hostile environments, significantly reducing the risks to scientists involved. If these could be developed and used entirely in place of manned aircraft during future events where ash clouds are threatening airspace, this would be very advantageous as it could provide continued information as to the properties of the ash cloud aircraft may be encountering.

Overall the need to further understand and define in-situ properties of volcanic ash clouds is crucial to the safety of aircraft when in-flight. This is important to both improving ash dispersion models, as well constraining the potential damage that ash can cause within the engine. Combining research into these areas will continue to dramatically reduce the volcanic ash risk to aircraft whilst in flight.

Chapter 3

Creating a Volcanic Ash Cloud

3.1 Introduction

Understanding and characterising ash clouds is important to the long and short term safety of aircraft. Short term consequences include the stalling of engines in-flight, abrasion to windshields, and damage to external components (Hufford et al., 2000); whereas long term repercussions include grounding of flights or the necessity of alternative routes, and continued damage to aircraft due to frequent ash exposure.

Although ash clouds have been sampled in-situ before using both UAVs and manned aircraft (Johnson et al., 2012; Macleod et al., 2022), there are few examples in the literature of the attempt to generate one within the laboratory. One example is a 0.6 x 0.6 x 0.6 m cube into which ash was dropped in front of a fan which then circulated the particles around the box; this was used to test what happens ash comes into contact with computer components (Gordon et al., 2005). Another similar example was conducted by Wilson et al. (2012), which looked at how volcanic ash effects laptops by again encouraging the ash to circulate by using fans and introducing it to the 'box' over a constant rate. Both studies concluded that volcanic ash is damaging to components of computers and laptops, reducing their functions, both mechanically and computationally. A more recent development was the design of a 0.3 x 0.3 x 0.3 m cube into which ash was dispersed via the use of small (0.08 m) fans, in order to test how ash damages a UAV propeller blade (Brosch, 2022). These three boxes are pictured in Figure 3.1 ((a) - (c)). They have also highlighted key challenges around box design: how to disperse/circulate ash within a confined space, how to allow ventilation but not ash escape and how to deliver the ash into the system?

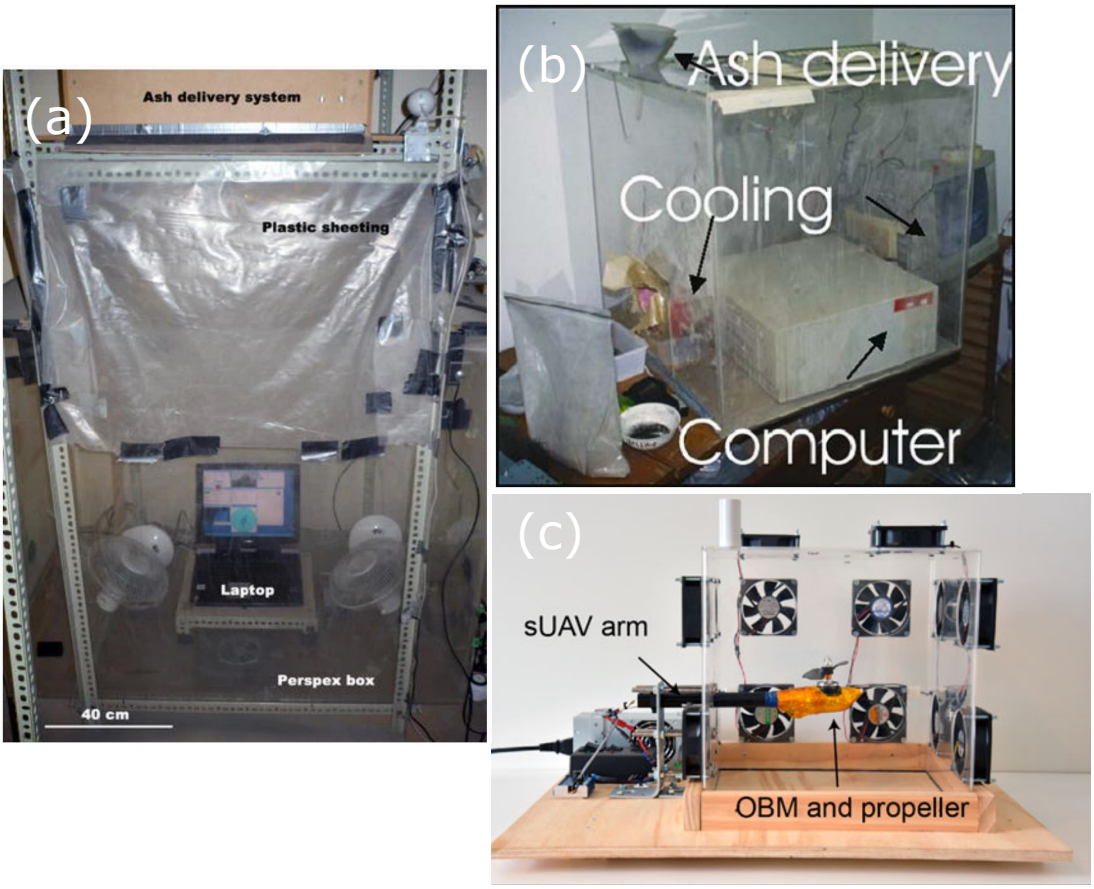

Figure 3.1: *(a) A box to test how ash interacts with computer components (Gordon et al., 2005) (b) Another example of a box looking at the interaction of ash with computers (Wilson et al., 2012) (b) A more recent example of a box designed to look how ash damages UAV components (Brosch, 2022).*

The ability to generate an ash-cloud in a laboratory allows multiple sensors to be tested and parameters explored, before their use in more challenging real-world environments and without the challenge of integrating sensors onto UAVs. A laboratory environment allows for great control, more adroit investigation of parameter space and potentially prevents damage to the sensors themselves as well as potentially helping save time when conducting expensive field work, as the most optimal way to use the sensors can be configured beforehand. It also helps gain understanding of how ash circulates when confined and exposed to an air flow. Within this chapter a novel ash-cloud box is designed and tested by looking at ash particle distributions and concentrations, using SEM stubs and a particulate matter sensor.

3.2 Sensors

Two types of sensors were used within the developed Ash Box 2 (AB2) to analyse the dispersal of ash in the system, as well as test out their individual capabilities and develop an appropriate processing method.

3.2.1 Scanning Electron Microscope (SEM) Stubs

The SEM stubs used in these experiments measure 12 mm in diameter and are composed of an aluminium pin with an adhesive carbon sticker. They can be inserted into the airflow and capture volcanic ash particles through sticking. After use they are carefully removed from the experimental set-up, making sure the carbon sticker is not touched, and stored in a sealed chamber to prevent any further contamination (Figure 3.2 (b)). The SEM stub allows the collection of in-situ ash within the box, and as outlined later in this chapter they can be processed to show captured particle size number distributions.

3.2.2 The Plantower PMS5003

The Plantower PMS5003 is a small (5 cm x 3.5 cm x 2 cm) (Figure 3.2 (a)), light-weight, affordable sensor used in air quality studies to look at particulate matter concentrations (Johnston et al., 2019; Masic et al., 2020), such as urban pollution. It is capable of measuring PM1, PM2.5 and PM10: particles having an aerodynamic diameter of 1, 2.5 and 10 or less microns, respectively. However, according to the "PMS5003 product data manual" in the case of this sensor, PM1 is defined as particles between 0-1 μm, PM2.5 is defined as particles between 1-2.5 μm and PM10 is defined as particles between 2.5-10 μm. Once particles enter the PMS5003, the device works by detecting light from a small laser scattered by particles which then transforms this into an electric pulse, which is used to determine the size of the intervening particulate matter value at any given time (Sayahi et al., 2019). This sensor has been used in previous studies mainly to look at urban pollution and is most accurate for detection in a range of 0-500 $\mu g/m^3$ (Wang et al., 2020; Johnston et al., 2019). However, it is more accurate when compared to similar sensors such as the Sesirion SPS30 and Amphenol SM-UART-04L (Nguyen et al., 2021). For PM1 particles though, all sensors showed the potential for large errors with the PMS5003 producing a percentage error of up to 126.7% at high concentrations (Nguyen et al., 2021). No studies, however, have yet evaluated its use in relation to analysing volcanic ash.

The data collected via the PMS5003 can be transmitted to a storage device or, as was the case for the ash-box experiments, stored locally on a raspberry pi.

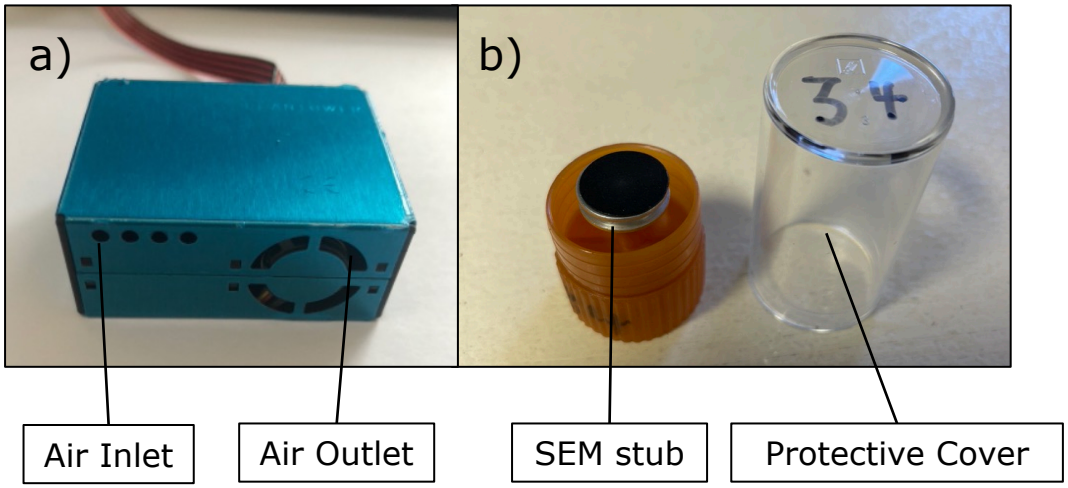

Figure 3.2: *(a) The PMS5003 (5 cm x 3.5 cm x 2 cm), highlighting the four holes where air is drawn in and the air outlet where it leaves the system (b) An example of a SEM stub (12 mm diameter) used in the experiments; it has been placed in the stub holder post exposure with the protective cover seen to its right.*

3.3 Methods

3.3.1 The Mini Wind Tunnel

The 69cm long mini wind tunnel was designed to be portable for use in a laboratory. It consists of three major components: the motor which powers the unit, an impeller which generates the airflow and an injection nozzle into the "ash box". The ash is added into the wind tunnel, before it is switched on, via a funnel which through a plastic tube, feeds into the impeller. This was chosen for use as it allows fast delivery of ash into the system, which is more comparable to speeds reached by UAVs when sampling at volcanoes. It also allows the ash to disperse and potentially circulate without the need for any further apparatus within the box, such as fans. Where the wind tunnel meets the box, there is a plastic ring which allows a seal to be created with the injection nozzle, and reinforces the point where they connect.

3.3.2 Ash Box Mark 1

Two boxes were designed in the process to create a suitable environment in which to generate an ash cloud, their major differing qualities are summarised in Table 3.1. The first box (henceforth referred to as AB1) was created from stiff cardboard with a folding top and three circular air vents (20 cm diameter) in its roof to prevent over pressurization. Once shut AB1 was sealed using duct tape along its seams. Early test experiments were run in AB1 to see if it was possible to generate a cloud. These tests, using stubs, generated promising results prompting the development of an improved box model. The negatives of this system were its sealing mechanism, fragile and damageable nature and the limited access to cleaning. Using duct tape to seal AB1 was a lengthy and expensive process and its removal after each use of AB1 increasingly created tears in the cardboard. The box was also difficult to clean after each run because many areas were folded, or ash because ash stuck to the duct tape. It was also difficult to access the experimental set-up as because it opened via folding panels on the top of AB1, and it had to be removed from the table after each run to clean and remove the sensors. When returning AB1 to the table, sealed with sensors present, there was also the possibility they could become damaged or moved within AB1 during transport.

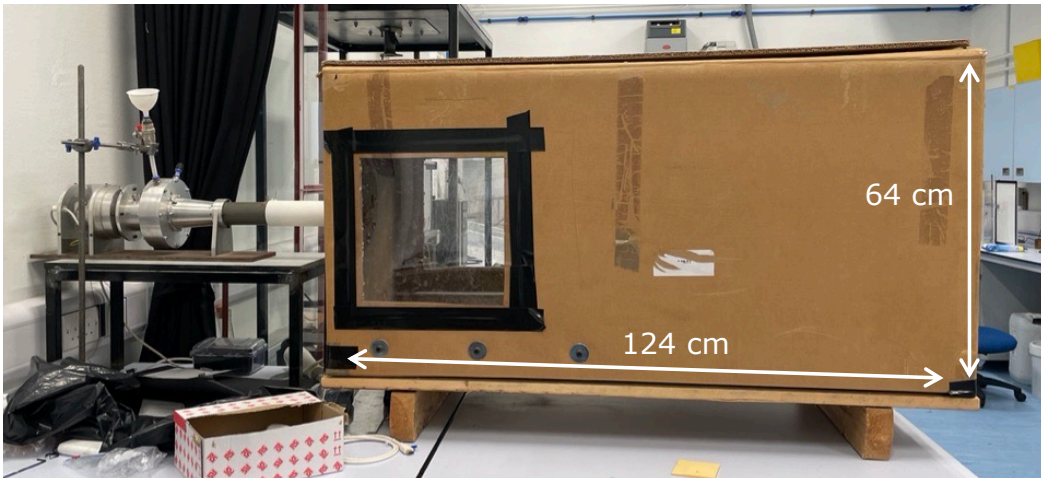

Figure 3.3: *A photograph showing the cardboard AB1. In this picture it has not yet been sealed, but duct tape can be seen holding on the observation window. AB1 is sat on a table, raising it approximately 1 m above the floor.*

3.3.3 Ash Box Mark 2

The second ash box (henceforth referred to as AB2) was an improved design, with an enhanced sealing system and easier cleaning capabilities (Figure 3.4 and Figure 3.5). When closed it is 139 cm in length, 89.5 cm in height and 63.5 cm in depth, and when opened the cavity inside is 128 cm in length, 79 cm in height and 53.5 cm in depth. The sealing system and cleaning abilities allow the experiments to be conducted faster and with less contamination between runs. AB2 is composed of stiff plywood with a hinged side panel; this allows it to be opened toward the user and the door propped up with a metal rod, which creates easy access for experimental set up and post-experiment cleaning, without removal from the table. There are three observation points as before; two near the round opening for the wind tunnel and one in the rear of AB2. These are screwed to the main frame of the box to create a good seal. Three large (27.5 x 31 cm) holes in the roof of AB2, covered with vacuum filters, permit ventilation, stop the build-up of pressure, and prevent particle escape. Once AB2 is shut it is sealed via fourteen screws around the door; a rubber seal within the frame creates an effective barrier to particles and increases the overall air-tightness. There is also a small hole (10 x 10 cm) near the base of AB2, to allow any cables to be run out of AB2 if necessary when powering sensors; this was sealed with a panel which screwed in place.

All the results from the following experiments in this chapter were generated in AB2, due to its increased capabilities and ease of use.

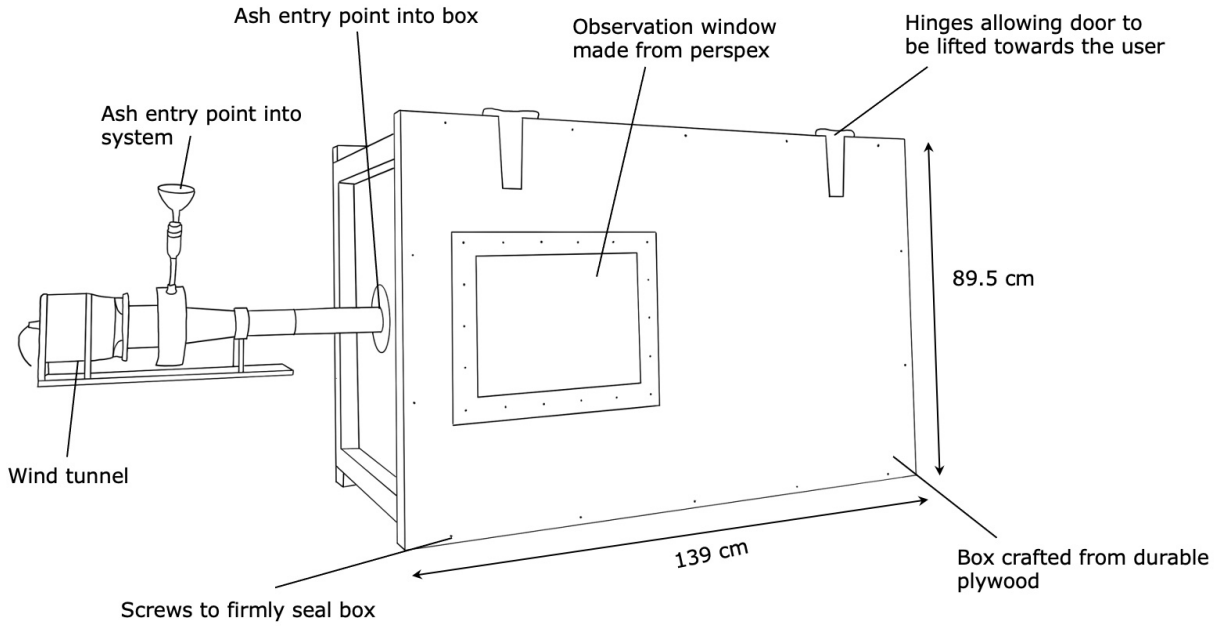

Figure 3.4: *A diagram showing the major components of AB2, as well as the wind tunnel.*

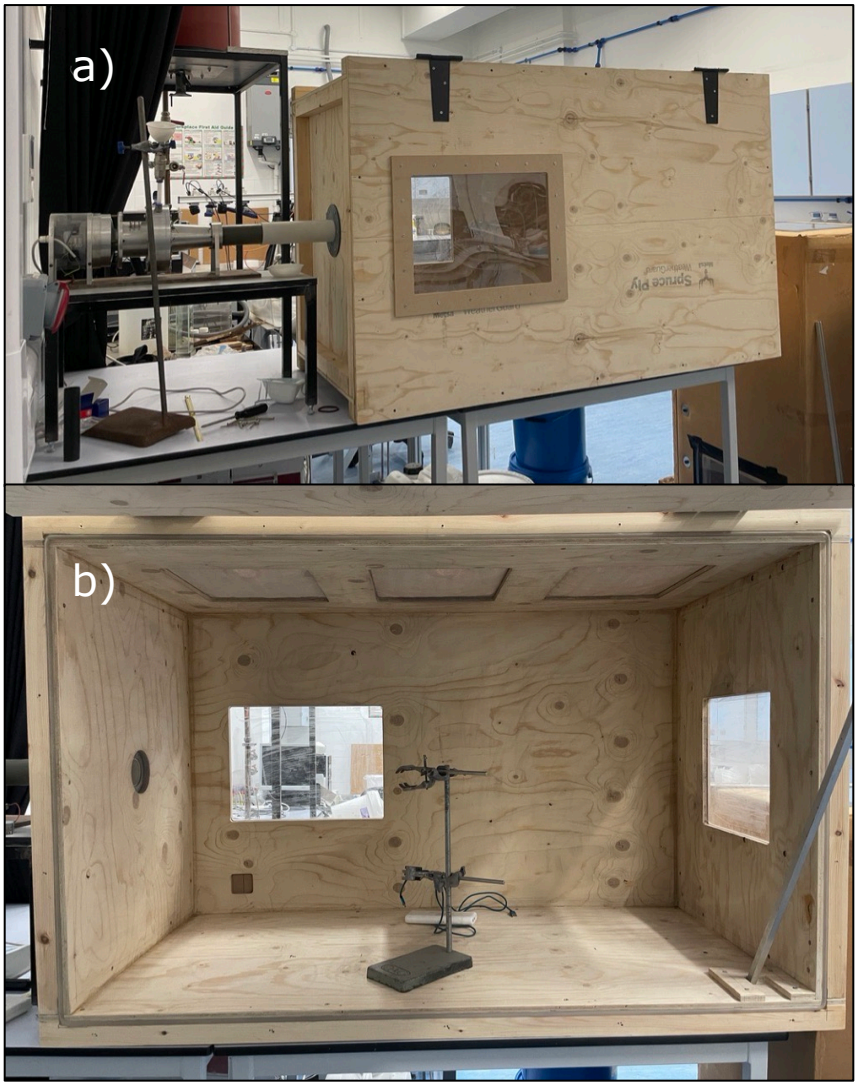

Figure 3.5: *(a) A photograph of the exterior of AB2, with it raised on a 1 m high table. The wind tunnel can also be seen connected to AB2. (b) The interior of AB2, with a clamp stand present, which is used in the experimental set-up. The wind tunnel entry point can be seen on the left hand side, as well as two of the viewing windows.*

Feature	AB1	AB2
Building Material	Cardboard	Stiff Plywood
Sealing System	Duct tape	Screws and rubber seal
Air vents	Three circular (20cm diameter)	Three rectangular (27.5 x 31cm)
Size	124 x 64 x 64 cm	139 x 89.5 x 63.5 cm

Table 3.1: *A table comparing the features of AB1 and AB2.*

3.3.4 Sample Preparation

The ash used in these experiments was collected on the flanks of Volcán de Fuego, North of San Miguel Los Lotes at a location of 14.41015 N, 90.82292 W.

Ash from this location was used throughout the experiments due to the accessibility of samples and the ash having the ability to potentially impact airspace when the volcano is undergoing a paroxysm (Naismith et al., 2019). In order to be an appropriate size for comparisons and processing it was ground using a ball mill at 450 rpm for 10 minutes. Two samples were made due to an insufficient volume of Fuego 1 being available to complete the experiments. This milled ash was then analysed using a CAMSIZER X2 in X-jet mode, to confirm the particle size distribution (Figure 3.6). The ash was milled due to the fact that most ash that reaches the combustion chamber within a jet engine is less than 100 microns in size (Clarkson et al., 2016). The CAMSIZER X2 confirms that 99% of the ash is $<$ 100 microns, with 50% of it being approximately $<$ 25 μm. The modal value, however, is at $\sim$ 50 μm, with between 3.9 - 4.8% of particles being this size.

The bulk composition of Volcán de Fuego ash is basaltic to basaltic-andesite with 53-56wt% Si (Liu et al., 2020) with a bulk density (DRE) of 2,750 kg/m^3 (Rose et al., 2008).

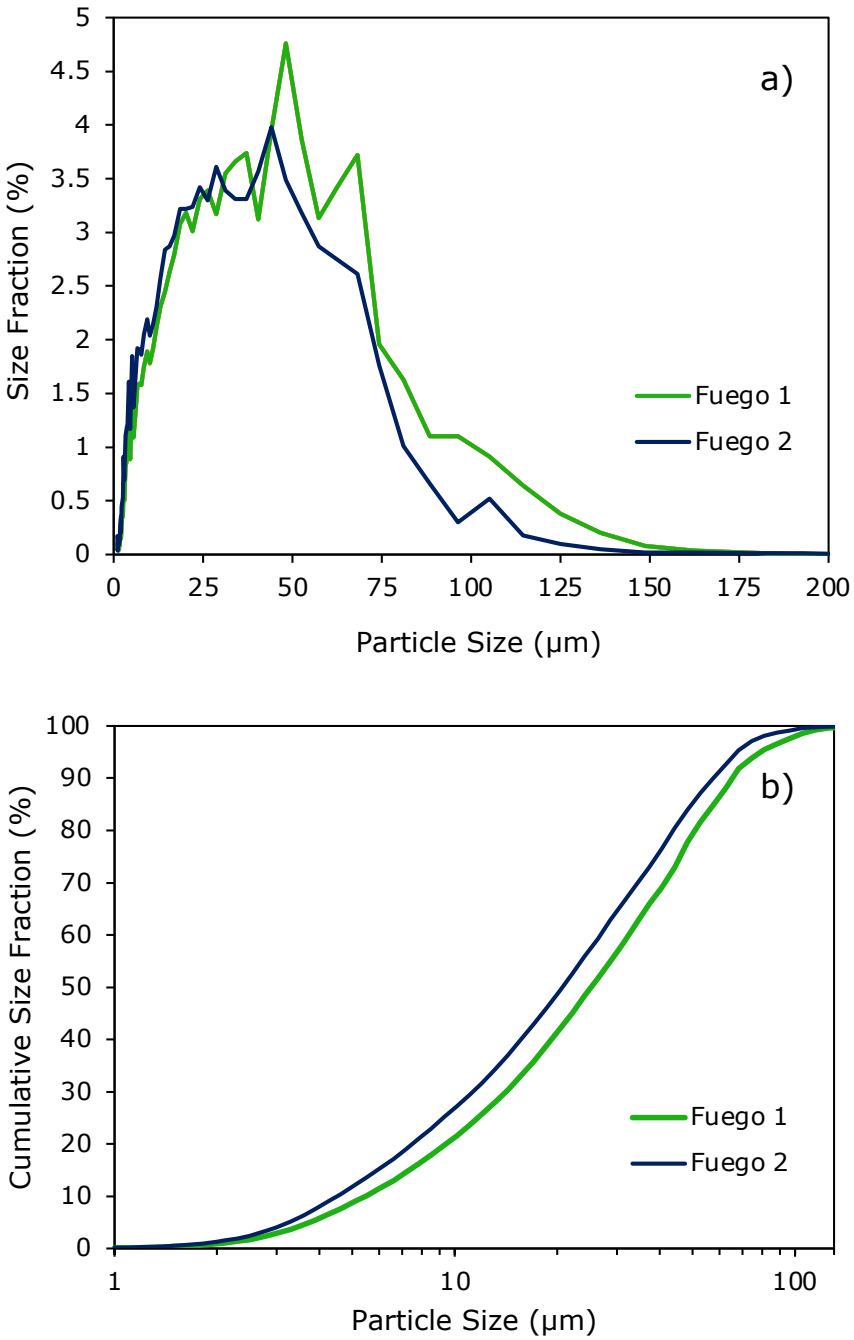

Figure 3.6: *a) Absolute percentage fraction of the two samples. b) Cumulative percentage fraction of the two samples*

3.3.5 Ash Cloud Generation

Before setting up each experiment, the wind tunnel was first run into the sealed AB2 for a minimum of 10 minutes to clear both itself and AB2 of any leftover contaminating particles. AB2 was then opened and thoroughly hoovered out to ensure there was a minimum amount of

contamination from previous runs or external airborne particles. The SEM stub was held in place using a clamp stand, making sure it is level with the wind tunnel inlet. The SEM stubs' adhesive label was removed last, before closing and sealing of AB2 to try prevent the exposed clean surface from coming into contact with any particles. When using the PMS5003 it is controlled via a raspberry pi, which is powered via an external battery pack. The raspberry pi is connected to over Wifi with a laptop by using VNC Viewer; this prevents the need for cables to be run out of AB2, which can decrease its ability to seal efficiently. Once the PMS5003 was connected to the external computer it was held in place using a clamp stand, facing the wind tunnel inlet: a second clamp held the battery pack steady. All experiments took place at either 30 cm, 45 cm, 60cm or 90 cm from the inlet. After the sensor had been set up, AB2 was then sealed and the ash sample put into the wind tunnel through the attached funnel, shaking it at regular intervals to ensure it all enters the system. At this point the experiment is ready to be started. 5g of Volcán de Fuego ash was used in every experiment that was run using an ash sample.After an experiment had finished AB2 was left for a further 5 minutes before being opened, to allow any suspended particles to settle, making them easier to capture with the hoover.

Wind speed was also measured inside AB2 at varying intervals of 15, 30, 45, 60, 75 and 90 cm using a hand held anemometer (Figure 3.7). As expected the speed decreases with distance from the wind tunnel entry point, starting at a value of 12.65 m/s at 15 cm when the door is closed and decreasing to 4.42 m/s at 90 cm. The other important distances to note are 30, 45 and 60 cm and the wind speeds with the door closed at those points are 11.50, 8.13 and 7.64 m/s, respectively. These compare well with the ground speed at which the UAV entered the ash clouds (see Chapters 4 and 5) which range from 12-20 m/s.

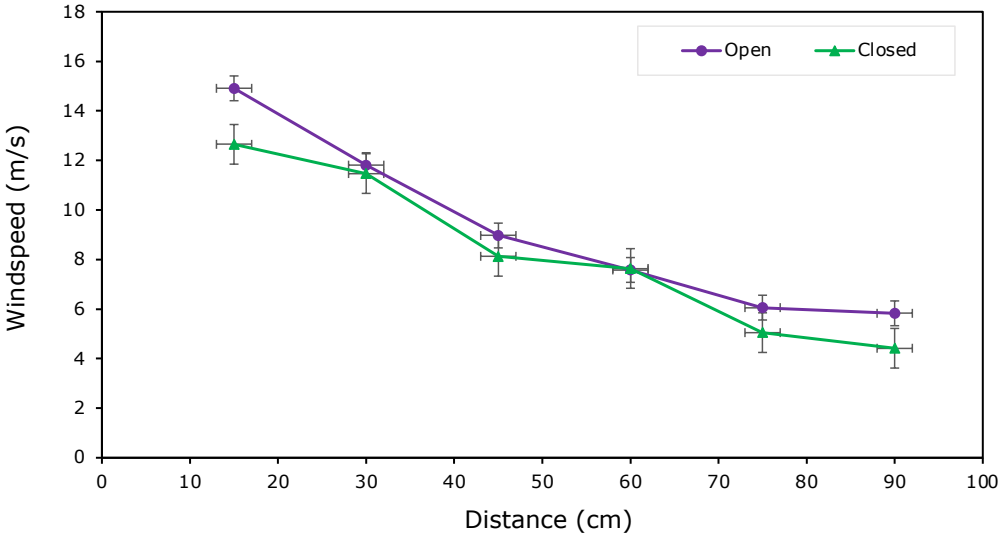

Figure 3.7: *A graph plotting wind speed (m/s) against distance (cm) from the wind tunnel opening. The two lines show the wind speed when the door is open (purple) and when the door is closed (green).*

Figure 3.8 shows high speed camera images of a large ash particle hitting a stub in AB1; it can be seen approaching the stub in the second image, then sticking in the third image. Although this footage was captured during an experiment with a different sample of Fuego ash (containing much larger particles), it also showed a proportion of fine particles being expelled from the wind tunnel, before the rest of the sample. The fine particles were too small to be captured individually hitting the stub.

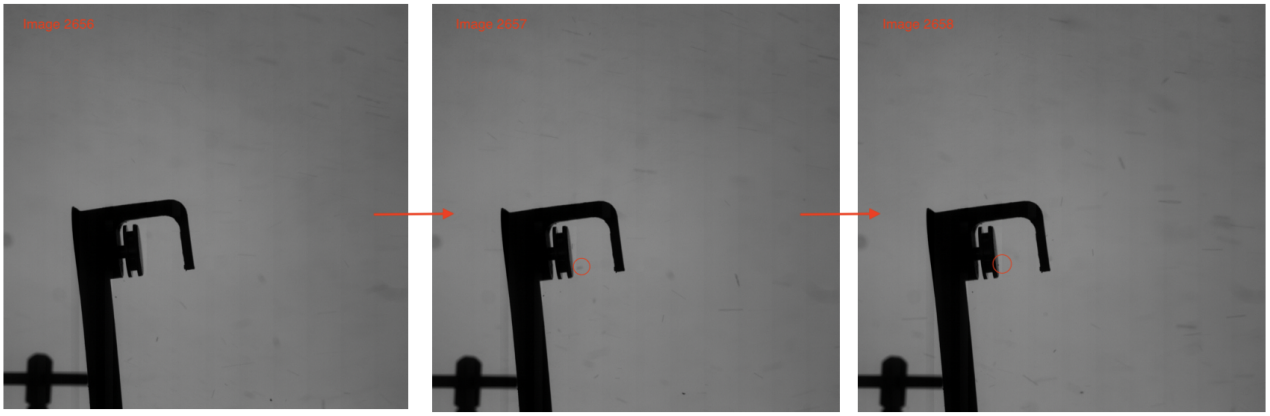

Figure 3.8: *These high-speed camera images show a particle hitting the stub within AB1. In the second image a particle can be seen approaching the stub and then sticking to it in the third image. In both cases the particle is highlighted by a red circle.*

3.3.6 SEM Stub Analysis

A Hitachi S-3500N SEM was operated in low vacuum (50 Pa) conditions and in backscattered electron (BSE) mode, with a working distance of 17 mm and at a magnification of x1000 to image the stub, post ash exposure in AB2. Due to the high magnification a 1mm square located at the centre of each stub was imaged by setting a pre-defined grid in the SEM. An overlap of 30% was used when defining the grid, to make stitching the collected images together easier, and to ensure none of the 1mm area was missed. The high magnification of x1000 was used as it allows the individual ash particles to be well resolved in the next processing step. A 1mm square was used in analysis as a representative of the stub, as the further manual processing carried out in Imagej would be extremely time consuming for a larger area. Using the centre of the stub as a target was also advantageous as it was easier to consistently analyse the same area on each stub.

3.3.7 Further Image Processing of the SEM Stubs

Once the individual images making up the 1mm grid were captured in the SEM they were stitched together using Image Composite Editor (ICE). This software looks for the similarities between the images to create a complete 1mm square.

The 1mm images were then further processed in Imagej to extract particle size distributions, as well as other particle characteristics. The processing in Imagej involved first carrying out thresholding, to create a 2D black and white image, altering the balance to prevent loss of particles or the gaining of extra particles. This was done by comparing the image that was being thresholded with the original SEM image. Following this the particles which are overlapping or touching each other were manually separated, by using the pencil tool in Imagej. This was a time consuming process but is necessary, as otherwise touching particles will be counted as one larger particle. Once this had been completed a macro (Liu et al., 2015) was used in Imagej which analyses every particle present in the image and produces a map numbering each particle along with a table containing the following particle properties: particle area, particle perimeter, convex hull area, convex hull perimeter, solidity, convexity, concavity index, form factor, major axis of best fit ellipse, minor axis of best fit ellipse, axial ratio, bounding box width, bounding box height, ferret diameter, and minimum ferret diameter. This table is used to carry out further processing discussion in the next section.

The steps in processing are summarised as follows and in Figure 3.9:

1. Ash covered stub collected
2. A 1 mm grid of 30% overlapping images is produced using the SEM at 1000x magnification (140 individual images produced)
3. These images are stitched together using ICE to produce a complete 1 mm square
4. The 1mm square is opened in Imagej and a scale is set by using an un-stitched image
5. Thresholding is carried out to produce a black and white image
6. Touching or overlapping particles are manually separated by hand comparing the black and white image with the original SEM stitched image
7. A macro (Liu et al., 2015) is run, producing a table with a range of particle properties and a 'particle map', which corresponds to each particle in the table.

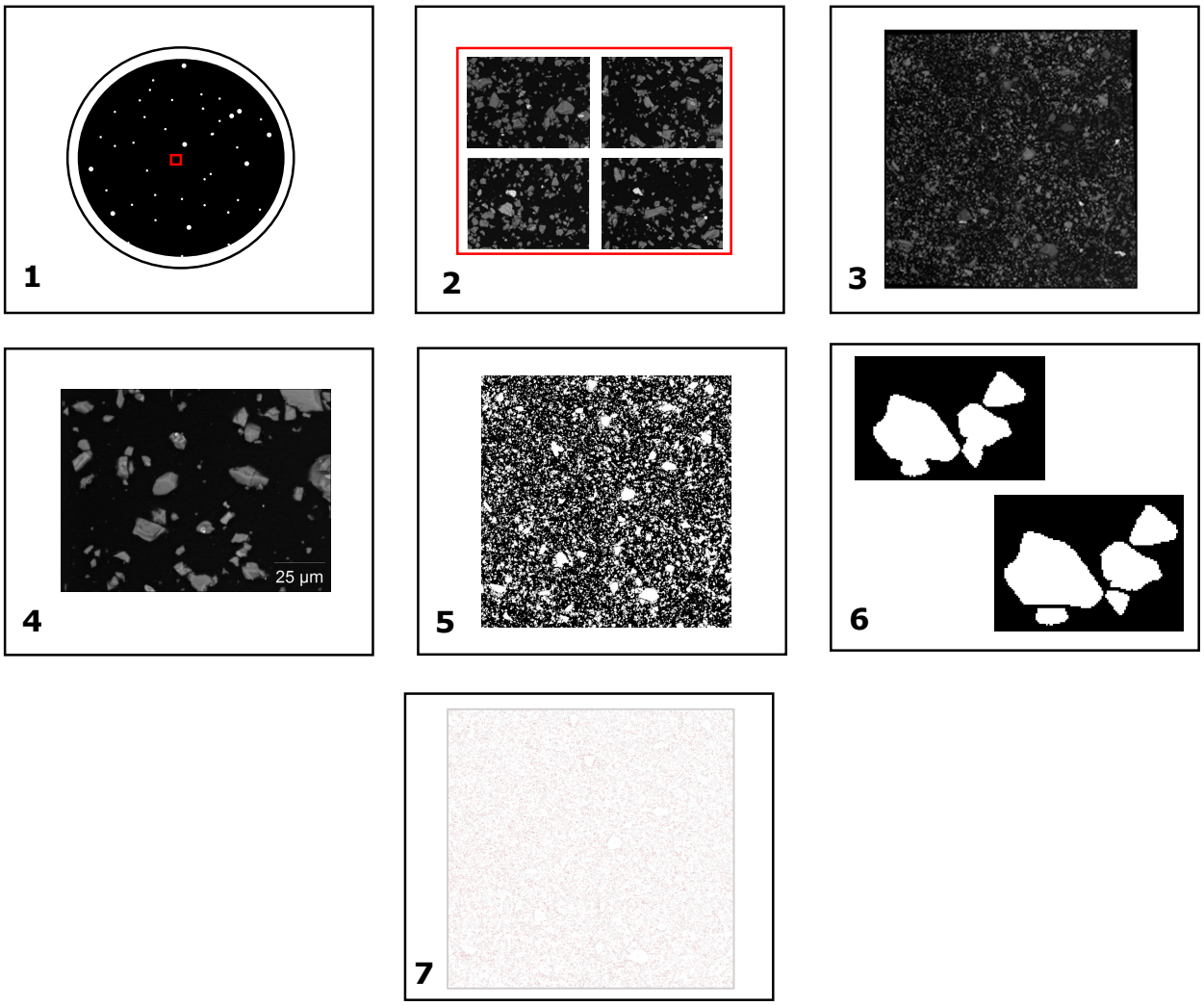

Figure 3.9: *This sequence of images shows the steps involved in processing a SEM stub from the raw data collection to the generating a particle map, as previously described. (1) Is the collected stub, with the red box highlighting the area imaged for the AB2 experiments (2) This represents 4 overlapping individual images captured at x1000 magnification in the SEM (3) The complete stitched 1 mm square (4) An indivdual image which is used to set the scale (5) The complete 1 mm square having been thresholded (6) An example of particle separation being carried out (7) The particle map, which is produced after the macro has been run on the separated image.*

3.4 SEM Stub Results

Table 3.2 shows a summary of the experiments carried out with SEM stubs present in AB2. It lists experiment number, ash type (Fuego 1, Fuego 2), stub distance from ash entry point, wind tunnel run time, number of particles present on the 1mm square, % of particles < 10 µm

on 1mm square and the mean particle size on the 1mm square. A calibration experiment with no ash in the wind tunnel was also carried out, and when imaged the stub was found to have almost no ash present. Data is missing at 30s for distances of 60 and 90 cm (experiments 3 & 4) due to it not being possible to stitch the grid of images together, as there are too few particles present for similarities to be found in overlapping images. The same applies to the calibration experiment.

3.4.1 Raw Images

The first stage in processing was to compile the raw 1mm squared images, correlating wind tunnel run duration with distance from where the wind tunnel enters AB2. Figure 3.10 shows the images once they have been stitched together in ICE. There are no images present at 30 seconds for 60 cm and 90 cm (experiment 3 & 4) due to the aforementioned fact there were too few particles present on the stubs in order to complete the stitching step. There is generally more ash present as wind tunnel run time increases, with the black carbon stub most noticeable in experiments 8 and 12. It is also possible to see larger particles sitting on top of smaller particles, particularly from experiments 9 and 13. Looking at the original SEM stubs before processing, can also highlight interesting features of the individual particles themselves, such as evidence for small particles sticking to larger particles or 'gathering' around the larger particles - potentially a sign of deposition in eddies and/or aggregation occurring. However, due to the sample having been ball-milled this may have effected the particles, altering their shape from when they originally formed. It is also possible to estimate how coated the stubs are with ash before SEM processing, as the stubs which are extensively covered (experiments 9 & 13) have a dusty appearance.

The resolution for these images varies slightly, with twelve stubs having a pixel resolution of approximately 8000 x 8000 and two stubs having a resolution of approximately 16000 x 16000. As the scale is set using a separate image from the SEM though, this should not effect the particle sizes measured. It will however, mean the edges of the particles on the higher resolution images are moderately more defined.

Experiment no.	Ash Type	Time (s)	Distance (cm)	No. of Particles	% Particles < 10 μm	Mean Particle Size (μm)
1	Fuego 1	30	30	31726	98.5	2.2
2	Fuego 1	30	45	7191	93.6	3.3
3	Fuego 1	30	60	N/A	N/A	N/A
4	Fuego 1	30	90	N/A	N/A	N/A
5	Fuego 2	60	30	16527	94.6	4.2
6	Fuego 1	60	45	8328	86.3	5.7
7	Fuego 2	60	60	7617	92.8	4.0
8	Fuego 1	60	90	3137	84.7	5.4
9	Fuego 2	300	30	36895	96.6	3.5
10	Fuego 1	300	45	10310	86.4	5.5
11	Fuego 2	300	60	10889	87.4	5.6
12	Fuego 2	300	90	3113	89.6	5.0
13	Fuego 2	600	30	34466	97.0	3.4
14	Fuego 1	600	45	8686	86.8	5.8
15	Fuego 2	600	60	11663	88.7	5.4
16	Fuego 1	600	90	5732	81.1	6.0

Table 3.2: *The SEM stub experiments.*

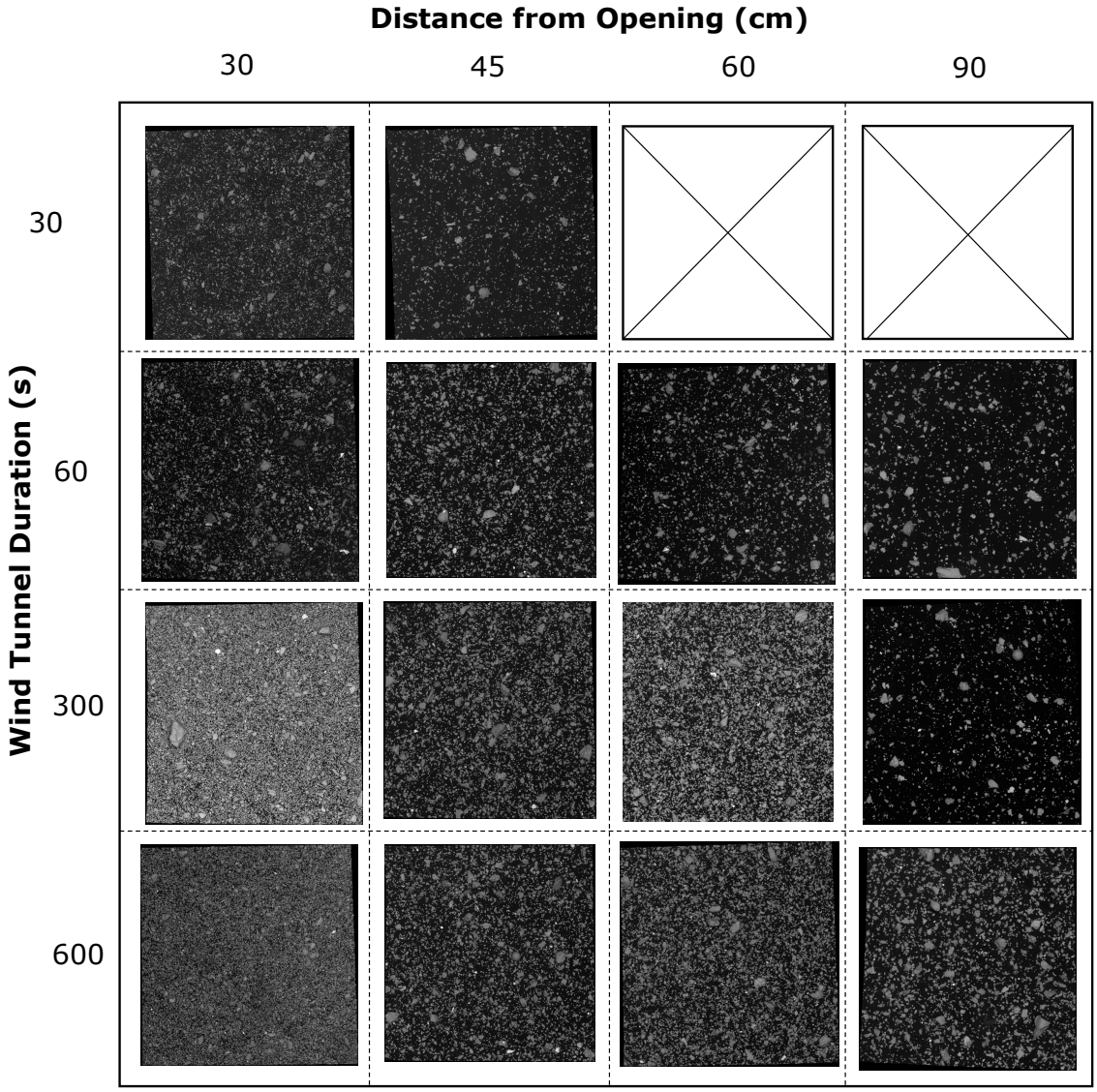

Figure 3.10: *This grid shows the raw 1mm squared images taken from the centre of the SEM stubs, across the various experiment distances and run times.*

3.4.2 Percentage Particle Cover

Percentage particle cover was worked out for each stub in Imagej, by first thresholding the image, then working out the percentage of black area (stub) compared with white area (particles); this is presented as pie charts in Figure 3.11. The highest percentage particle cover of 55.9% is observed from experiment 9 (30 cm, 300s), and the lowest of 10.0% during experiment 12 (90cm 300s). The only experimental runs where the particle percentage cover goes above 50% are observed at a distance of 30 cm for 300 and 600 s. These charts also show that generally as wind tunnel duration increases, particle coverage increases, with little difference being seen

between 300 and 600s at 30, 45 and 60cm. However, at 90cm there is a marked increase in coverage between 300 and 600s, with it changing from 10.0% to 29.4%. There is also a particularly dramatic change at 60 cm between 60 s and 300 s with coverage increasing from 17.3% to 42.3%. Interestingly, the particle coverage also increases to a higher value at 60 cm for 300 and 600 s, when compared to the same runs times at 45 cm.

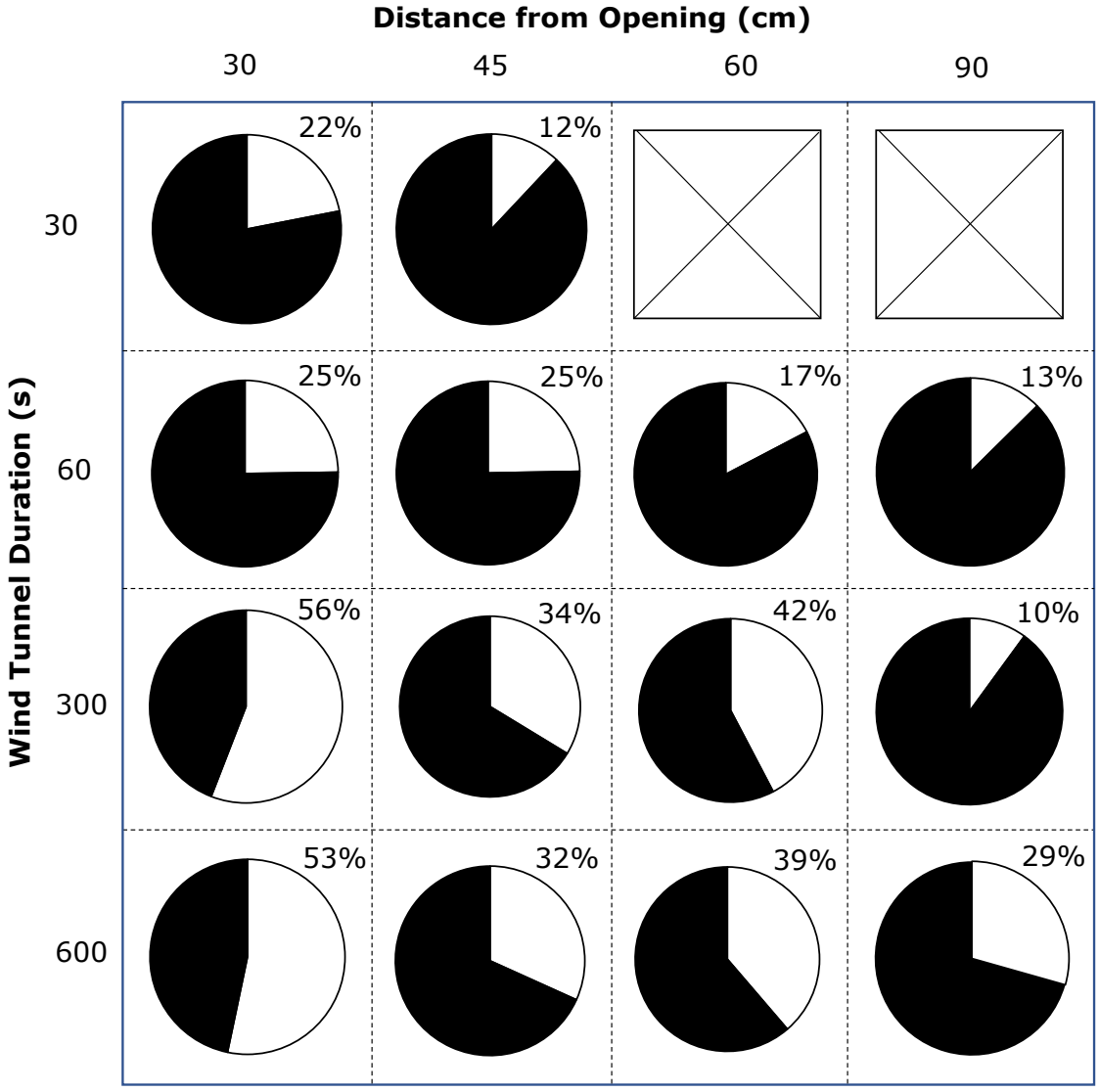

Figure 3.11: *These pie charts show the percentage particle cover across the stubs, taken from the 1mm squared raw images. The white segment represents the percentage of space the particles are taking up, compared to the black background of the carbon stub.*

A repeat of experiment 6 was run (45cm, 60s) to look at particle percentage coverage repeatability. On visual inspection, once the repeat SEM images were stitched, the two stubs

looked to have a similar coverage of particles; this was confirmed to be 21% on the repeat versus 25% from the original experiment. This implies that the experiments are repeatable as 21% is still above the 12% particle coverage from experiment 2 (45cm, 30s) and is within 4% of the original experiment. Slight variation is likely to occur as some particles will stick more efficiently to the stub than others; this could be a result of shape or speed at which the particle hits the stub.

3.4.3 Particle Size Distributions

In order to produce particle size distributions for each stub, the area equivalent diameter was first calculated for each particle. This meant that for a given particle, it was assumed to be spherical and a diameter for that equivalent circle was used to look at particle size. This value was chosen for this analysis due to the irregularities in shape observed across the particles. A python code (Appendix B) was written to simplify this process, which takes the area for each individual particle from the table of particle properties produced using the Liu et al., 2015 macro, and after calculating the area equivalent diameter, generates the particle size distributions. This was also used to look at the number of particles on the stub, mean particle size and percentage of particles < 10 μm present.

The very fine particles were then put into 1 μm sized bins from 0-10 μm, showing the number percentage for each size category (Figure 3.12), with the maximum value on the y-axis being 50%. The two stubs which were run for 30 s at 30 and 45 cm from the wind tunnel opening contain the highest percentage of < 1 μm material, with the highest value of 48% being reached during experiment 2. Experiment 1, however, had the highest percentage value of particles < 10 μm, with a value of 98.5%. For the stubs at 30 cm, when the wind tunnel was run for 60s , 300 s, and 600 s, there was little difference in the number percentages observed, particularly between 300 and 600s. There is a spike of 27% in the 0-1 μm bin observed during experiment 10, whereas this bin remains low (12.5%) during experiments 6 and 14. At 90 cm from the wind tunnel opening there were some changes between the varying run times with the 0-1 μm bin remaining similar ($\sim$ 20%) at 60 and 600s, but decreasing to 14% at 300s. These two runs also correspond to the lowest percentages of particles < 10 μm, with values of 81.1 and 84.7%, respectively.

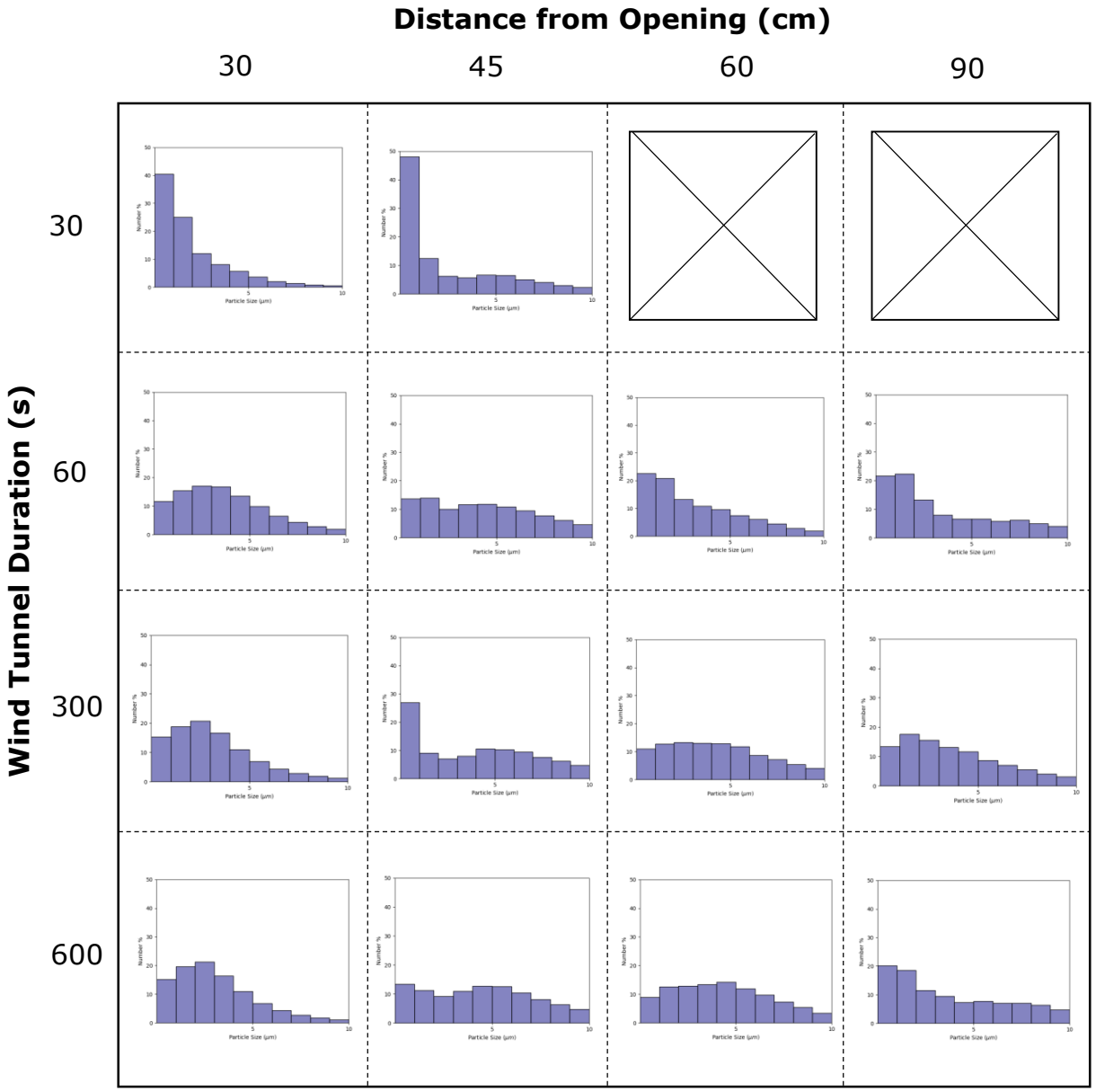

Figure 3.12: *These graphs show the percentage number of particles in bins ranging from 1-10 µm, across all the experiments, excluding the two where the images were not able to be stitched together.*

3.5 PMS5003 Results

Table 3.3 lists the experiments carried out involving the PMS5003, showing ash type or no ash present, wind tunnel run time and distance from wind tunnel entry point. PM1, PM2.5 and PM10 data are collected simultaneously during each experiment.

Experiment no.	Ash Type	Time (s)	Distance (cm)
17	Fuego 2	600	45
18	Fuego 2	600	60
19	Fuego 2	600	90
20	No ash	600	45
21	No ash	600	60
22	No ash	600	90
23	Fuego 2	600 (60s intervals)	45
24	Fuego 2	600	45
25	Fuego 2	600	45
26	Fuego 2	600	60
27	Fuego 2	600	60

Table 3.3: *The PMS5003 experiments.*

3.5.1 Calibration Experiments

The wind tunnel was run with the PMS5003 at 45, 60 and 90 cm with no ash present, to allow for comparisons with experiments containing ash. Looking at the PM1 values in Figure 3.13 ((a) – (c)), it can be seen that across all the experiments there are similar values of PM1 regardless of whether there is ash present or not. Experiment 19 (90 cm, ash present) does however show a strong initial reading of ash over the first 120 s, before it begins to overlap from with the data from experiment 22 (90 cm, no ash). The readings from experiments 19 and 20 are also generally lower, only reaching a high of 288 $\mu g/m^3$, compared to 356 $\mu g/m^3$ at 45 cm and 342 $\mu g/m^3$ at 60 cm. At 60 cm, there are also only two very short sections where the data for ash being present are higher than that where no ash was present; these both occur near the start of the wind tunnel being run (between 0 - 14 s and 43 – 53 s).

The PM2.5 (Figure 3.13 (d) – (f)) readings are quite different from the PM1 readings, with there being a strong spike in the values where ash was present, across all three distances as the ash leaves AB2. There is also considerably less overlap seen in these data between the ash and no ash experiments, when compared to PM1. The overlap is particularly minimal for 45 cm with, there only being a very short section where the no ash readings are higher than the ash readings; this is between 552 s and 561 s. There is slightly more overlap at 60 cm,

however, with the data where ash was present showing a very different pattern from the no ash data, with the no ash data being fairly constant at a value between 750-1000 $\mu g/m^3$ and the ash data showing an initial spike, followed by a decrease and then a second increase over a longer time frame, before decreasing again. During the first decrease in the ash readings, they begin to overlap with the no ash readings. At 90 cm the no ash data again has a relatively constant value between 400 -504 $\mu g/m^3$ and begins to overlap and stay close in value with the ash data after the initial spike as ash leaves AB2; this starts to happen at 228 s. There is however a small increase in the ash readings at 90 cm between 324 s and 410 s

The PM10 data (Figure 3.13 (g) – (i)) are very similar to the PM2.5 data, with almost exactly the same patterns being observed, except that the values reached are higher.

Overall, the PM2.5 and PM10 values at 45 cm show what would be expected: a strong increase as ash enters AB2 and reached the PMS5003, followed by a gradual decrease in values as it begins to disperse within the space, eventually overlapping with the no ash readings. The readings of PM1 and PM2.5 at 60 cm and 90 cm, however, show evidence for a potential re-circulation of ash within AB2 as it interacts with the back wall, as they display a more atypical pattern.

3.5.2 Distance Sensitivity

The PMS5003 was run over 10 minutes at 45, 60 and 90cm, to analyse the distance sensitivity within AB2. The PM1, PM2.5 and PM10 data are re-plotted here (Figure 3.14 (a) - (c)) from the calibration experiments to make it easier to see the difference between readings for each distance. Looking at all three PM readings, the highest concentration is always reached at 45cm: for PM1 a concentration spike of 356 $\mu g/m^3$ is reached after 404 seconds, for PM2.5 the highest value of 2200 $\mu g/m^3$ is reached after 15 seconds, and for PM10 the maximum concentration of 4600 $\mu g/m^3$ is also seen at 15 seconds. Graph (a) also shows that the value of PM1 is continuously quite low and has a fairly constant value of around 200-300 $\mu g/m^3$ across all three distances. There appears to be a second wave of particles at 60 cm as the concentration begins to rise again for PM10 and PM2.5 after $\sim$ 110 s, until $\sim$ 400 s, reaching a value not dissimilar from the original peak as the particles entered AB2. When the PM10 and PM2.5 readings reach this second peak at 60 cm, this series also surpasses the synchronous values being collected at 45 cm. After 400 s the concentration continues to decrease until the wind tunnel is switched off. As mentioned in the previous section there is also a short second

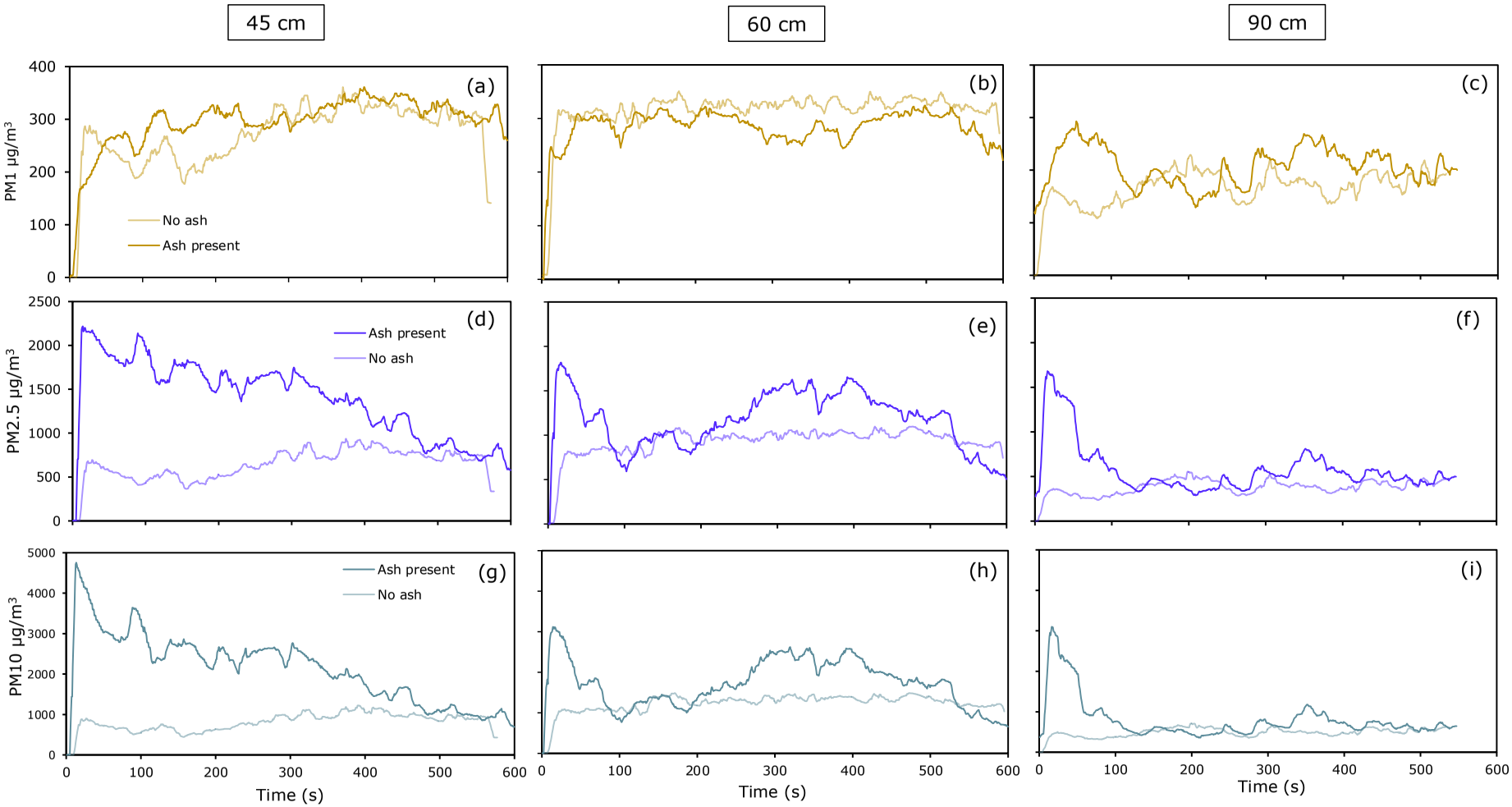

Figure 3.13: *These graphs show the comparisons in data between running the wind tunnel over 600 s, with ash both being present and absent. (a) - (c) show the PM1 values, (d) - (f) the PM2.5 values and (g) to (i) the PM10 values.*

spike in the PM2.5 and PM10 readings at 90 cm between 324 s and 410 s. These "second waves" seen at a similar point in the data for both 60 cm and 90 cm (the "second wave" at 60 cm, however, being much longer and more significant), show strong evidence for re circulation of ash within AB2.

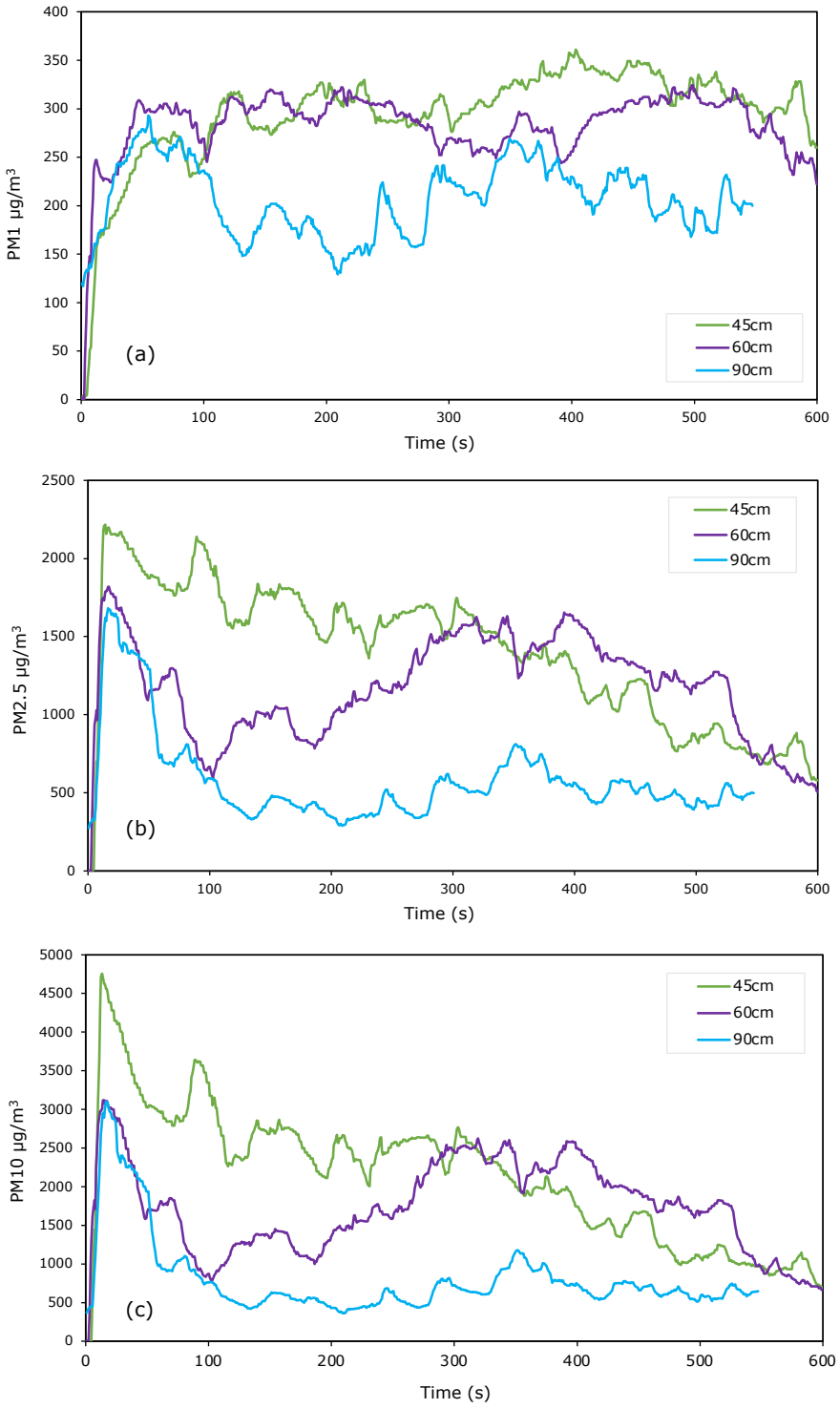

Figure 3.14: *a) Time series showing the PM1 readings over 10 minutes in AB2 at 45 cm from the opening. b) Time series showing the PM2.5 readings over 10 minutes in AB2 at 45 cm from the opening. c) Time series showing the PM10 readings over 10 minutes in AB2 at 45 cm from the opening.*

3.5.3 PM1, PM2.5 and PM10 Comparisons

Values of PM1, PM2.5 and PM10 were also plotted together for easier comparison at 45, 60 and 90 cm (Figure 3.15). As seen in the distance sensitivity experiments (Figure 3.14) the values of PM1 are fairly similar for all three distances suggesting strong and consistent recirculation of the smallest size fraction. At 45 cm there is a relatively large difference between PM10 and PM2.5 potentially implying that larger particles (between 2.5 and 10 μm) are present in greater concentrations at this point. This is particularly noticeable when the wind tunnel is initially switched on as this is where the gap is largest. At 60 cm there is the same initial larger gap, which then closes to a difference of only ∼100 μg/m^3, However when concentrations begin to increase again during the strong reciruclation event at ∼300 s this gap increases again, perhaps implying that the second wave is occurring due to an influx of particles in the 2.5-10 μm range.

At 90cm there is again the initial larger gap, but this time it is followed by very similar readings of PM2.5 and PM10 after 60 s, perhaps indicating that the particles reaching this distance overall have a lower diameter. Again this gap increases slightly as the small second spike is reached at ∼ 340 s.

These graphs highlight the similarities in the shape of the PM2.5 and PM10 readings across all three distances, with the data series almost mimicking each other perfectly. However, at different distances circulation of ash clearly varies. At 45 cm there is an initial increase in concentration followed by a relatively stable coda, of a form that is also broadly captured in the 90 cm experiments. However, at 60 cm there is significant recirculation peaking at 300-400 s after initial injection of ash. This is likely to be due to the position of the sensor relative to the back wall (see discussion).

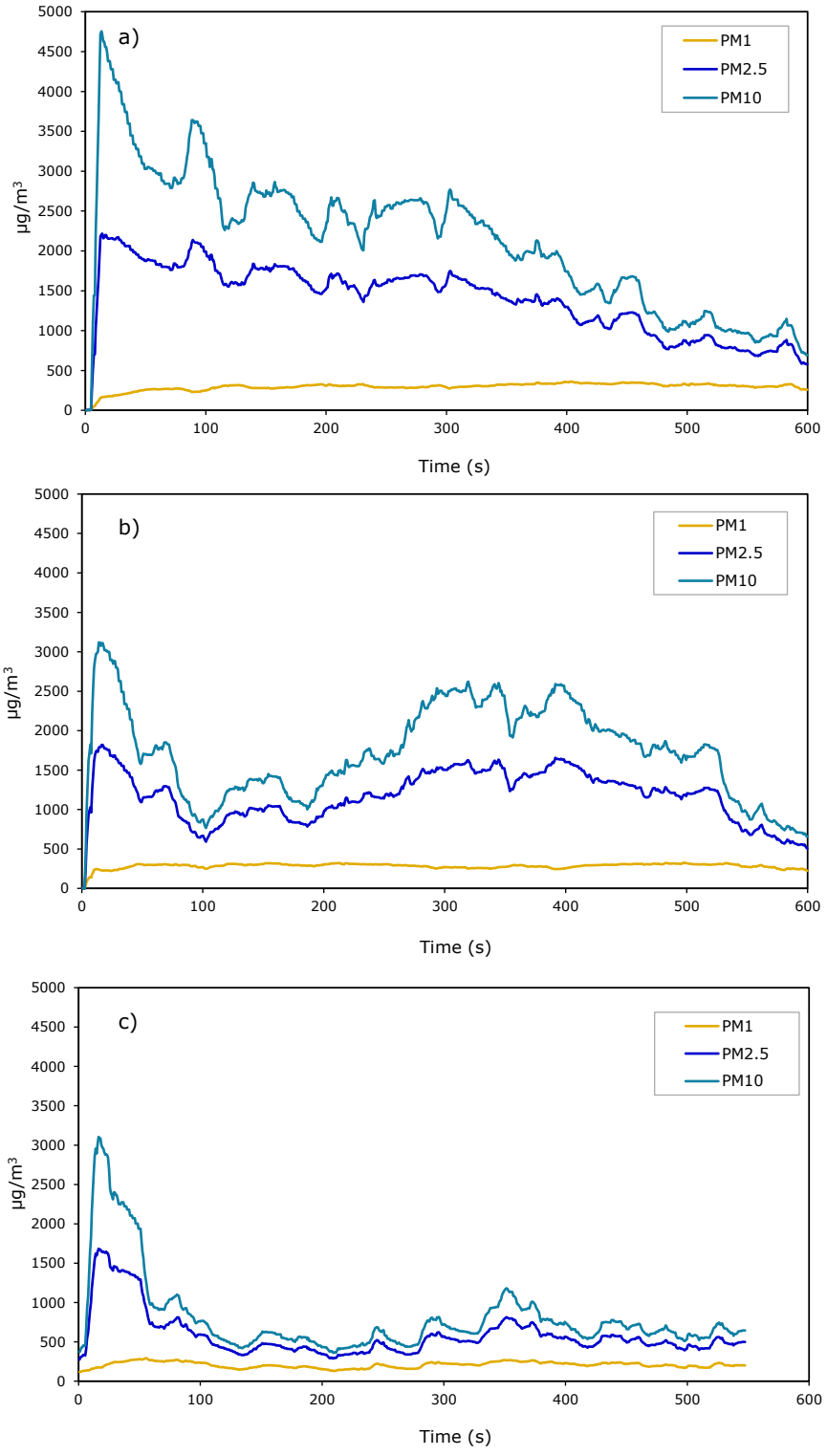

Figure 3.15: *Values of PM1, PM2.5 and PM10 plotted together at distances of (a) 45 cm, (b) 60 cm and (c) 90 cm.*

3.5.4 Intervals

With the PMS5003 located at 45cm within AB2, the wind tunnel was run at 60s intervals (60s on, 60s off), over 600s. Looking at Figure 3.16, this showed a particular decrease in PM10 and PM2.5, when the wind tunnel was stopped for 60s, but a less marked decrease in PM1. In fact, the spike in PM1 reading seems to increase to the same value (approximately 400 $\mu g/m^3$) every time the wind tunnel is switched on, indicating that PM1 is consistently recirculated during and after activation of the wind tunnel. In contrast, PM2.5 and PM10 concentrations decline during the wind tunnel's activation and inactivity suggesting both fallout and a greater activation energy for resuspension as a function of their increased mass.

As was seen in the distance sensitivity experiments, PM10 and PM2.5 also seem to show a very similar pattern, mimicking each other almost perfectly, perhaps implying that a large majority of particles are within the 1-2.5 μm diameter range. This data also shows that the fallout rate of PM10 is greater than that of PM2.5, as can be seen when the PM10 concentration drops faster than PM2.5, each time the wind tunnel is switched off for 60 s.

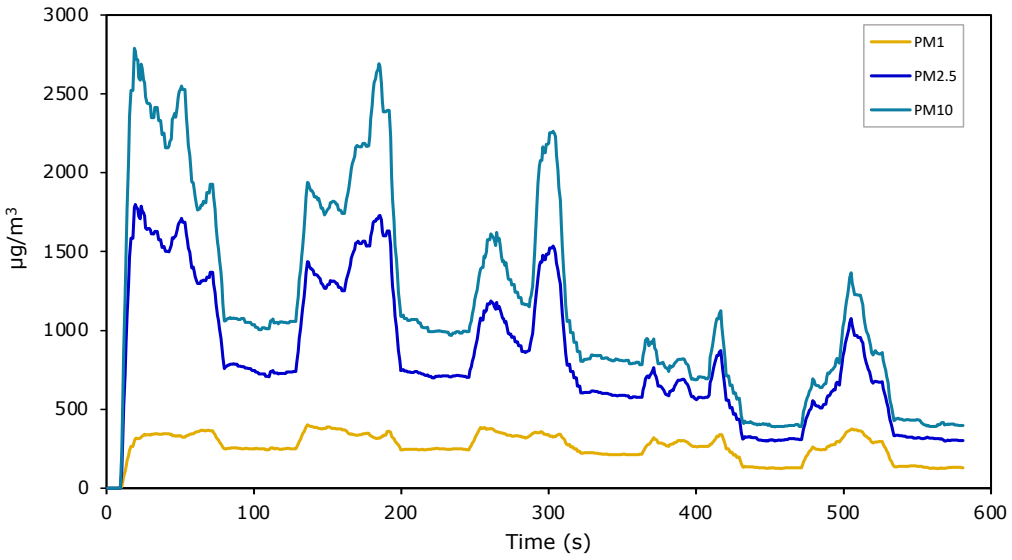

Figure 3.16: *This graph shows PM1, PM2.5 and PM10 data collected at 45 cm, with the wind tunnel being run at 60 s intervals.*

3.5.5 Repeats

Repeats were carried out at 45 cm and 60 cm within AB2, with the wind tunnel being run for 600s. At 45 cm (Figure 3.17 (a)) all three repeats showed an initial spike in PM10 concentration,

with run 3 reaching the highest initial value of ∼4800 μg/m^3, however, after this the values vary in places across the different experiments. Runs 2 and 3 show a relatively consistent pattern, reaching their peak concentration within the first 120 s then gradually decreasing in value to around 1000 μg/m^3 over the subsequent 480 s. The two runs begin to overlap particularly closely after 300 s. Run 1 is unusual in that after an initial spike in concentration, it reaches a maximum concentration of 5543 μg/m^3 after 141 s, which is also a much higher peak than is reached during any other run. It does overlap with runs 2 and 3 between 350 and 450 s, but then the data increases in value to finish at a value of ∼ 1900 μg/m^3 after 600 s.

At 60 cm the repeats are more consistent (Figure 3.17 (b)), also showing an initial spike when the wind tunnel is switched on, this time followed by a dip in concentration which begins to rise again after ∼ 100 s for run 2 and after ∼ 200 s for runs 1 and 3. Run 3 in fact, rises to a concentration of 2939 μg/m^3 after 489 s, which is higher than its initial spike of 2556 μg/m^3, when the ash first entered AB2.

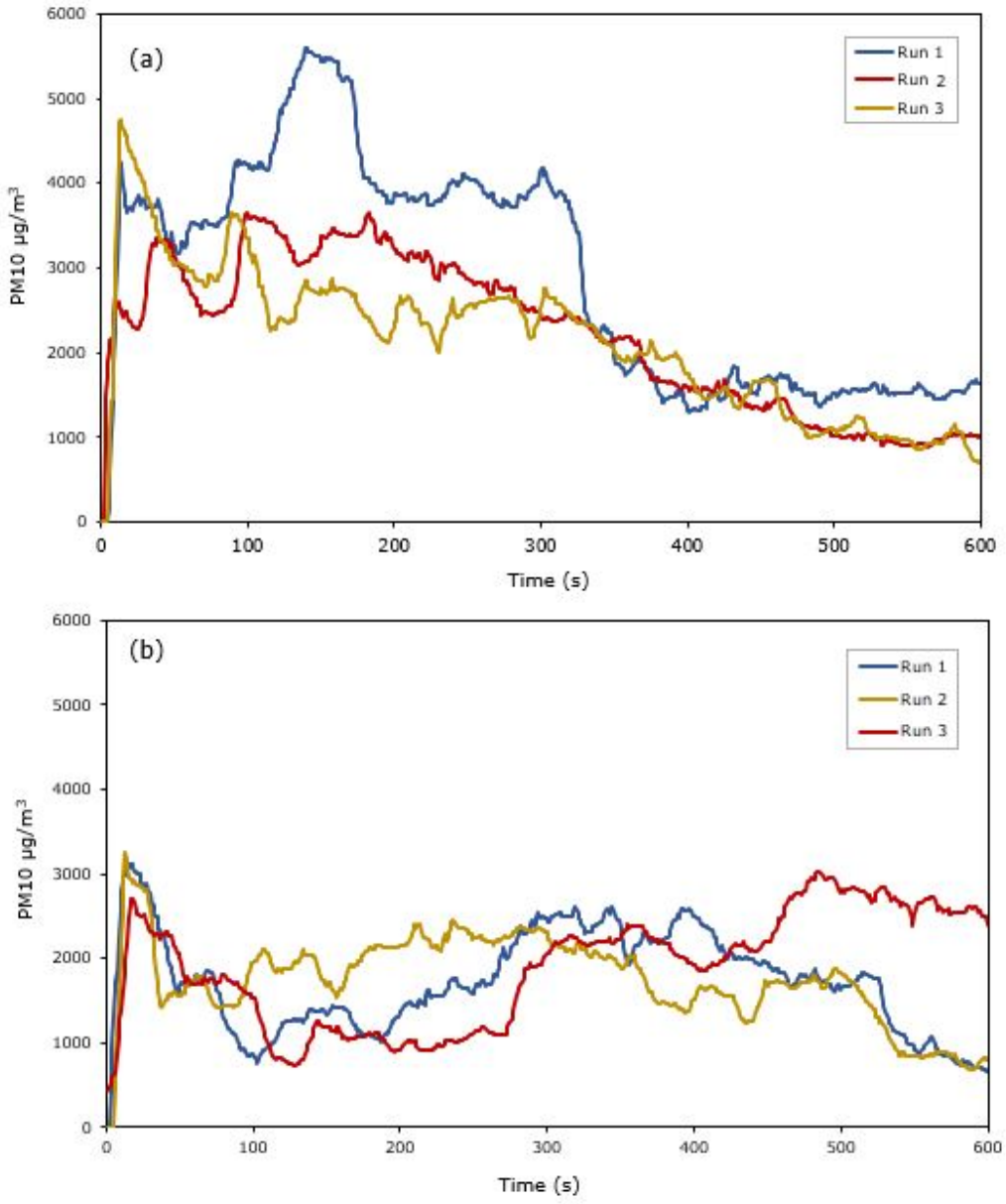

Figure 3.17: *These graphs show three repeats run at (a) 45 cm and (b) 60 cm, all over 600 s.*

3.6 Discussion

AB2 is capable of generating a testable ash clouds in the lab. However, observations suggest that the experimental data need careful consideration. There is the potential for remobilisation of material from previous experiments if not completely clean, and there is a sensitivity to particle size as a function of distance from the back wall.

3.6.1 Percentage Mass Calculations

The data collected via the PMS5003 show concentrations as a function of mass per unit volume, whereas the particle size distributions calculated from the SEM stubs are concerned with number of particles present at each size, with size having been calculated from their area. This makes comparing the data between the two sensors challenging as large quantities of PM1 will only contribute to a small amount of the overall mass. In order to investigate this further and help with comparisons, the percentage mass for each stub was calculated. This was done by converting from size (f(r)) to mass (f(r^3) using the average particle diameter from each bin, the number of particles within each bin and the density (Rose et al., 2008) and assuming the particle is spherical. Figure 3.18 shows the percentage of the distribution (number & mass) for each stub, plotted against the average radius of each bin. These graphs clearly all show that the mass percentage increases as particle diameter increases, and that the opposite is true for the number percentage, with its value decreasing as particle diameter increases. This is especially emphasised in experiments 1 and 2, where $\sim$ 40-48% of the particles on each stub are $<$ 1 μm, with these large spikes in number concentration only accounting for a very small percentage of the mass ($<$ 2%). The cross over point for each graph (where number and mass concentration equal each other), tends to happen at a diameter between 3 and 6 μm, with this value increasing as there is a larger percentage of particles with a greater diameter.

These graphs help to explain why particularly the PM1 readings from the PMS5003 are much lower than PM10, despite there being large quantities of PM1 present on the stubs. They also emphasise the importance of comparing number and mass concentrations to gain an overall understanding of the ash present.

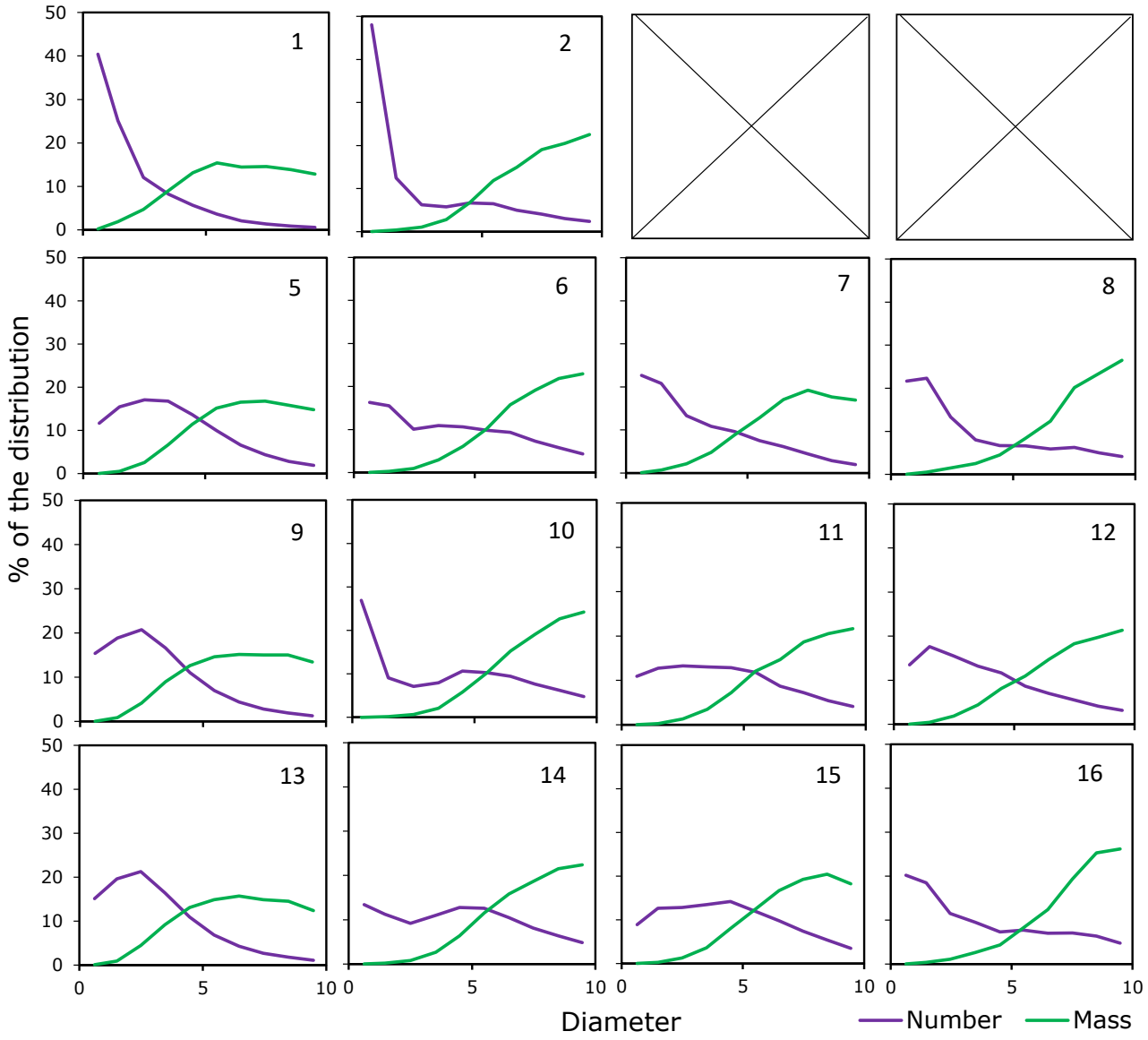

Figure 3.18: *These graphs show the size (purple) and mass (green) fraction of the particles collected on the stubs during the experiments (number given in top right of each box, positions of experiments unchanged from previous figures).*

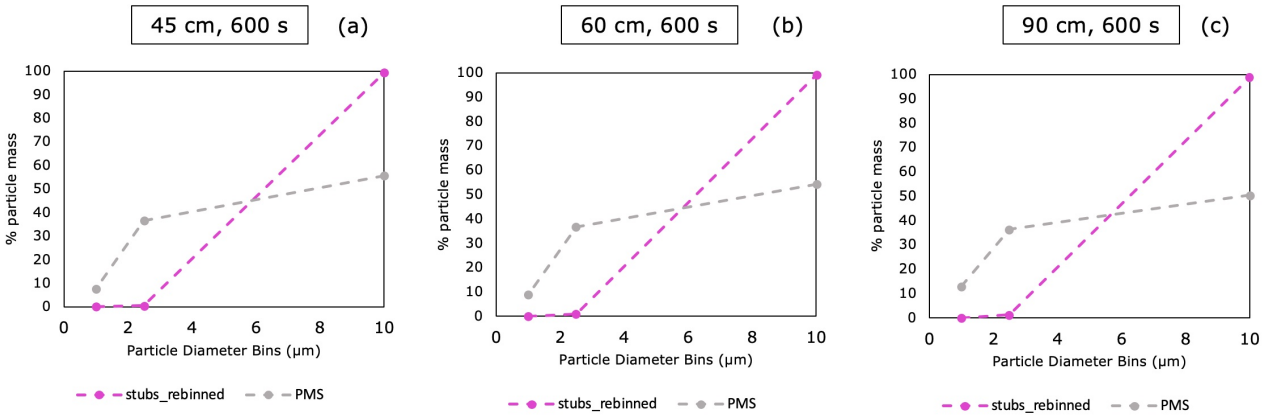

Figure 3.19: *These graphs show the percentage mass comparisons at 600 s between the PMS 5003 and the stubs for distances of (a) 45 cm, (b) 60 cm, and (c) 90 cm.*

In order to compare more directly with the PMS5003 data the number percentage values for the stubs from experiments 14, 15 and 16 (45, 60 and 90 cm; all 600 s exposure) were re-binned into PM1 (0-1 µm), PM2.5 (1-2.5 µm) and PM10 (2.5 - 10 µm); these were then converted to mass percentages as previously described. This re-binning of the stub data from 0-10 µm bins (as is seen in the previous graphs) to bins of PM1, PM2.5 and PM10, allows easier comparison with the PMS5003 as it only captures data in those three size fractions.

An average of the PMS5003 readings across 600 s at 45, 60 and 90 cm, for PM1, PM2.5 and PM10 was then also calculated and then worked out as a percentage of the overall mass. These values were then plotted on Figure 3.19, and show that despite the actual masses being different, the percentage masses across all three distances are quite similar. Looking at the PMS5003 data PM1 and PM10 show the greatest change in percentage mass across the distances of 45, 60 and 90 cm, with PM1 increasing by ∼5% from 45-90 cm and PM10 decreasing by ∼5%; PM2.5 remains constant across the distances.

Comparing the two lines for each sensor though show that the PMS5003 is assuming there is a higher presence of PM1 and PM2.5 than the SEM stubs. This could be a result of poor collection efficiently of very fine material on the stubs, which has been shown to be the case by previous fluid dynamic models (Macleod et al., 2022), where very fine particles are pushed around the stub, rather than sticking to it. This could also help explain why the percentage value is considerably higher at PM10, because at diameters in this range, the collection efficiency begins to increase with a better chance of particles sticking. This idea is further explored in Chapter 4.

The percentage mass of the original 5g of Fuego ash which entered AB2 and adhered to the stub was also calculated for each experiment and is summarised in Table 3.4. These results show that for a duration of 30 and 60 s the percentage adhering to the stub, continuously decreases from 30 cm to 90 cm. However, for 300 and 600 s, this percentage decreases till 45 cm then increases again at 60 cm, before significantly decreasing again at 90 cm. This is indicating that there are processes (most likely recirculation) occurring at 60 cm in AB2, after 300 s.

Wind Tunnel Duration(s)	**Distance (cm)**	**% original Fuego ash adhered**
30	30	11.17
30	45	5.61
30	60	N/A
30	90	N/A
60	30	15.64
60	45	8.91
60	60	6.41
60	90	3.27
300	30	25.83
300	45	13.94
300	60	14.27
300	90	3.33
600	30	23.17
600	45	12.77
600	60	15.51
600	90	6.72

Table 3.4: *This table shows the percentage of the original 5g of Fuego ash which adhered to the stubs at the across the various distances and run times.*

3.6.2 Further SEM Stub and PMS 5003 discussions

The particle number distributions (Figure 3.12), show that it is likely a large proportion of the very fine material (< 2 μm) is expelled from the wind tunnel almost immediately after it is switched on. This is seen in the graphs for experiments 1 and 2 (30 s at 30 cm and 45cm), which

show a high percentage of this material. Although the high speed images (Figure 3.8) were taken with a different sample, they also helped to confirm that a proportion of fine material exited the wind tunnel before the coarser, more visible particles. Some of this material may be present on the other stubs but is potentially being masked by larger particles sitting on top which are not present on the stubs from experiments 1 and 2. The PMS5003 experiments, however, do imply that a large concentration of PM10 leaves the wind tunnel within 10 s of it being switched on, perhaps implying that these larger particles take longer to stick to the stubs. It is also confirmed from the PMS5003 experiments that there can be a second wave of particles or a continued release of material over 600 s (Figure 3.15). This second wave of particles is particularly seen at 60 cm, which can also be tied to the percentage coverage graphs which show a large increase in coverage for the stubs present at 60 cm after 300 and 600 s (Figure 3.11). The particle number distributions also indicate that at 60 cm after 300 s and 600 s the number of particles below 2 μm has considerably decreased, which could also be indicative of a second wave of particles bringing an influx of larger particles.

The previously discussed mass/number percentage graphs also highlight that fact that although the PM1 concentration never reaches values close to those for PM2.5 or PM10, it does not mean there is a large number of PM1 particles present, just that their concentration appears to be lower because of their minimal mass. The PMS5003 results for PM1 also introduce uncertainty as the value of PM1 is very similar regardless as to whether AB2 contains ash or not. Clearly though, there is a significant percentage of PM1 present as can be seen from the SEM stubs.

The inconsistent results collected at 45 cm (Figure 3.17 (a)) imply that perhaps the ash sample is not exiting the wind tunnel at a constant rate, instead sometimes becoming trapped and leaving in smaller bursts. They could also imply that if the ash exists the wind tunnel in a fan shape, it does not create this shape perfectly each time. Perhaps also there is ash present from previous runs which has not fully exited the wind tunnel. Furthermore it could be evidence of re-circulation if AB2 had not been thoroughly enough cleaned from the previous run.

The percentage particle cover (Figure 3.11) shows, as expected, that with increasing wind tunnel duration, there is an increased particle coverage on each stub, with this being particularly marked after 300 s, except for 90 cm, where this change is only seen after 600 s.

The interval data (Figure 3.16) is interesting because it gives an indication of fallout

rates of ash in AB2, confirming that PM10 is falling out of suspension faster than PM2.5 or PM1. During the 60 s when the wind tunnel is switched off though, the PM readings never reach 0, implying that the particles remain in suspension longer than this time. Future experiments could look at this fallout rate, testing how long it takes for readings to return to 0. It is also interesting that the PM1 values always return to the same level each time the wind tunnel is switched on; this could potentially be a result of PM1 being more mobile, due to its low mass, meaning it all gets re circulated within AB2.

3.6.3 Particle Circulation

Analysing the SEM stubs and PMS5003 data together also shows evidence for a circulation pattern of ash within AB2. Due to there being a prolonged second spike in concentration at around 300s at 60cm, as well as a large increase in particle coverage, this is suggestive of circulation occurring as a result of particles interacting with the back wall of AB2. The fact that there are more particles present on the stubs at 60 cm after 300 and 600 s, than those at 45 cm, also potentially indicates that these stubs are receiving a second influx of ash, compared to the stubs at 45 cm. When cleaning AB2, particles are also found on the back wall, confirming that they are travelling the whole length of AB2.

Figure 3.20 shows a proposed circulation scheme for ash within AB2 when the wind tunnel is switched on. As the ash sample leaves the wind tunnel it initially diffuses, with some of it hitting the stub directly, but other fractions of it travelling up to the ceiling of AB2 and to the base. This ash then potentially hits the back wall and circulates round to 60 cm again, where it has a second chance to adhere to the stub. The PMS data also seems to infer that a large fraction of these re circulated particles are in the 2.5-10 μm range, as the PM10 values increase more significantly when re circulation is proposed to start taking place.

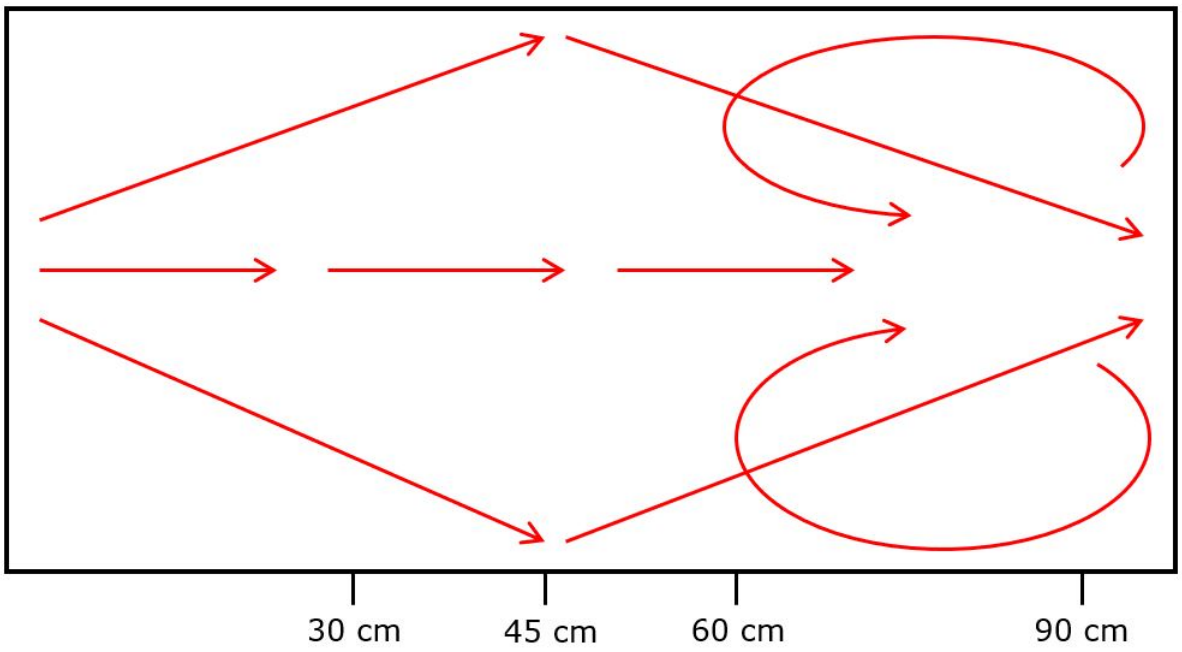

Figure 3.20: *Proposed circulation within AB2, with the red arrows showing the direction of travel for ash particles. Once these particles hit the back wall, it is proposed they begin to circulate back towards 60 cm.*

Particle sticking might also be effected by what angle and speed the particles hit the stub at. Some particles which bounce (hit the stub and not stick), may be more likely to stick a second time as they have lost kinetic energy. Very fine particles could also be potentially blown off as a result of prolonged exposure to the wind tunnel air flow. Contrary, larger particles may also struggle to stick efficiently to the stub as they may be travelling faster than the very fine material. The re-circulation of ash could also effect the angle at which the particles are hitting the stub, when they approach it for a second time. This could also help explain why there is a significant drop in the number of particles <2 μm after 300s.

3.6.4 Errors and Uncertainties

Experimental uncertainty includes potential contamination in AB2, either from insufficient collection of particles via hoovering or leftover sample still be present in the wind tunnel. The rough surface of the wood within AB2 is also causing some particles to become stuck to its surface, which can be seen by darker areas within AB2 being present, that are unable to be removed by hoovering. Contamination of the stubs could also occur once the wind tunnel is switched off and particles are left to settle before AB2 is unsealed, especially as the very fine

particles are likely to stay mobilised for a longer duration. However, it is very difficult to prevent any contamination at this point as opening AB2 prematurely could also cause further particles to stick to the stub.

There is also potential error introduced during further processing of the ash exposed SEM stubs. During the step where individual particles are separated from one another (either touching or overlapping) (Figure 3.9 (6)), there is a proportion of human error introduced as this this step is done manually. This could lead to the possibility that some particles have been missed or are separated incorrectly. This could lead to an increased average particle size as particles which should be two individual shapes are being analysed as one larger unit. There is also loss of smaller particles which are lying on top of larger particles, as they cannot be separated. This error will tend to increase with percentage coverage, as when there are more particles present, they are packed closer together on the stub.

Some error is also introduced by particles which threshold poorly due to their colour or shape, as this has the possibility of creating a "blurred" area which can be counted as a collection of small particles. Thresholding also further introduces the error that very small particles may be missed out or particles become artificially enlarged. Increasing the brightness and contrast prior to thresholding can help with this, but there are often still particles present with "blurred" edges or very small particles missed.

A comparison of the macro output was also run on the separated and non-separated images, with the non-separated images generally tending to show an increase in very fine particles (<1 μm). This could be a result of, by carrying out separation, more particles are being shifted into the larger size bins, reducing the percentage number of particles in the smallest bin. Figure 3.21 shows this for experiments 6, and 14, with the most noticeable difference occurring for experiment 6 where the percentage number of particles between 0-1 μm changes from 41% when separation has occurred to 45% when separation has been carried out. The overall percentage of particles < 10 μm changes by about 1% on each occasion: 97.7% (not separated) to 98.5% (separated) for experiment 6 and 80.0% (not separated) to 81.1% (separated) for experiment 14.

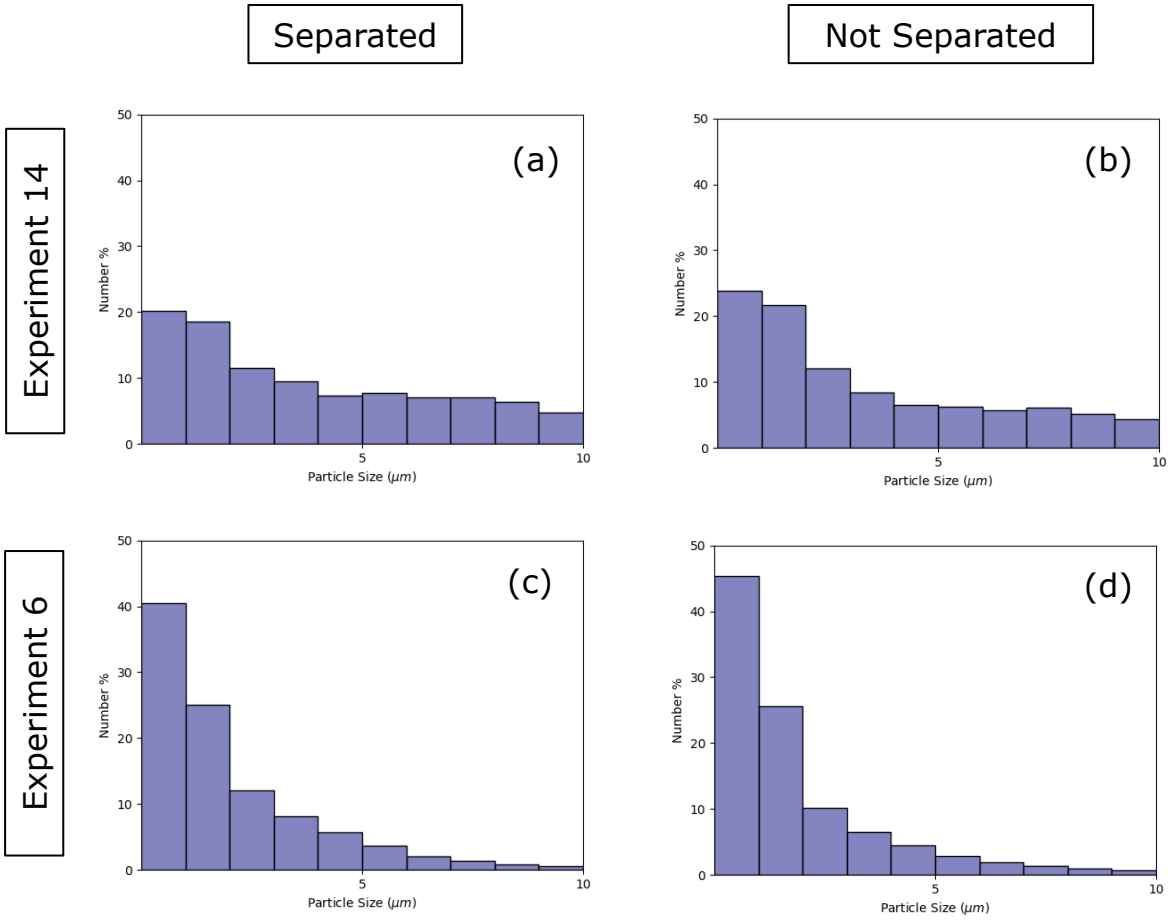

Figure 3.21: *These graphs show comparisons between the separated and not separated number percentage values from the SEM stubs, for experiment 14 (a) - (b) and experiment 16 (c) - (d).*

3.6.5 Further Work

Further sensors could be tested within AB2 to understand more about the sensors themselves as well as continuing to ascertain how particles are moving around the space. AB2 could also be used to explore the ability of UAV components to withstand damage from volcanic ash, as was carried out by Brosch et al., 2022. This could help prevent the loss of these vehicles in volcanic areas as a result of interactions with potentially damaging ash. It would also be interesting to put the PMS5003 sensor in areas where it is hypothesised there is very little ash likely to be present; such as near the wind tunnel opening but not in its direct path. Placing stubs and the PMS5003 facing the back of the wall, particularly at 60 cm, may also yield interesting results which could help further understand the re circulation of ash in AB2. Future experiments with an SEM stub and the PMS5003 being placed simultaneously in AB2 could

help with characterising particle movement.

Due to this being the first time AB2 has been used to carry out experiments, there are some areas of experimental design which could be improved to reduce error. Ash entering the system after the impeller could help prevent any damage to the particles within the wind tunnel and may also allow particles to enter AB2 more smoothly. There is potential evidence on the stubs that some particles may have been broken or splintered before entering AB2. Improved calibration of the PMS5003 sensor with known concentrations of volcanic ash would also be advantageous as well as spherical particles of a similar size. Further ash samples from volcanoes which are likely to cause a hazard to aviation could also be tested to see if their dispersion pattern within the box is different from the Fuego samples.

Other areas of improvement for AB2 could also include a using clamps rather than screws for sealing; this would increase the speed for each experiment whilst still preventing ash particles from escaping. Painting the inside of the box white would also allow for easier cleaning and location of ash within AB2, as well as creating an environment where water could be introduced to change relative humidity levels.

With the SEM stub processing, if particle separation could become automated this would dramatically increase the speed at which data is generated. This is particularly true as the stubs become increasingly coated with ash. This however may be difficult to achieve as it would require a macro being able to differentiate and pick out ash particles that are often overlapping.

3.7 Conclusions

The following conclusions can be drawn from this chapter:

- This experimental set-up is a valuable way of testing sensors with volcanic ash before deploying them in the field. It is also useful in assessing which parameters are most beneficial to retrieve in order to make data collection increasingly streamlined. Although the maximum wind speed generated by the wind tunnel (12.65 m/s), is not as high as the speeds at which UAVs can fly, it still gives the advantage of being able to inject ash into the system at greater speeds than previous ash box examples, exposing sensors to conditions they are more likely to encounter in the field.

- The percentage particle coverage graphs show that as wind tunnel duration increases there

is increased coverage on the stubs (Figure 3.11). The particle number distributions (Figure 3.12) revealed that a large quantity of very fine material (< 2 μm) is being expelled from the wind tunnel within the first 30s, whilst for 60s and beyond this fine proportion has dramatically reduced. There is however the potential for larger particles to be masking smaller particles below, particularly at 300 and 600s, where percentage particle coverage is much higher. The PMS5003 experiments provide evidence for circulation within the box which is clear in Figure 3.15 (b), where at 60 cm from the wind tunnel inlet there is a second prolonged peak in particle readings across PM1, PM2.5 and PM10.

- AB2, when combined with the wind tunnel, has been characterised to show the movement of ash in the system. This led to a proposed circulation (Figure 3.20), whereby ash disperses as it leaves the wind tunnel, interacting with the ceiling and the back wall of AB2, before re-circulating to 60 cm again.

- There is some debate as to the accuracy of the readings below 1 micron for both the stub analysis and the PMS5003. This is due to the fact that the readings of PM1 from the PMS5003 are similar whether there is ash present in AB2 or not; this could be a result of contamination or it could be the accuracy of the sensor itself decreasing at the lower PM reading. However, there are high percentage values of PM1 present on some of the SEM stubs and as shown by the percentage mass calculations, they would produce low readings of PM1 concentration (Figure 3.18).

Chapter 4

In-situ Collection of Volcanic Ash from a Fixed-Wing UAV at Volcán de Fuego

4.1 Introduction

Uncrewed aerial vehicles (UAVs) are an important technological enabler, allowing collection of in-situ data from active volcanoes. Their use significantly lowers the risks to scientists in the field by allowing data to be collected safely from previously inaccessible places, helping to advance scientific knowledge and our understanding of processes occurring within volcanic systems. This is particularly true close to volcanic vents where conditions are harsh and sometimes unpredictable but many important processes are most effectively studied. The longer any ash cloud interacts with the ambient atmosphere the less information about the initial conditions is retained. Using UAVs removes the need for manned aircraft to be flown through, or close to, ash clouds, to collect data, which puts human lives at risk. Collecting in-situ video and photography data is also vital to aircraft safety as it allows conditions pilots may face, such as a reduction in visibility, to be more thoroughly understood.

An advantage of collecting particle size data using UAVs is it allows certain parts of the plume to be targeted where ground samples or manned flights cannot access, at a spatio-temporal resolution that remote sensing cannot replicate, collecting data which is representative of proximal conditions. This is potentially useful for volcanoes which are not currently posing a risk to aircraft, in order to help plan for future eruption scenarios. However, if these UAV systems are refined and improved, they could be deployed quickly in the event of an eruption, especially when close to airports, which threatens aircraft safety, to generate real-time data

which can be used to drive dispersion models (Wilkins et al., 2016).

Volcán de Fuego is a 3768 m stratovolcano located in Guatemala (Figure 4.1), which exhibits strombolian activity (Lyons et al., 2010), regularly erupting with low-energy ash laden explosions. On the 14th of October 1974 there was a subplinian eruption which generated a 18 km high ash-cloud and ejected material over a five hour period (Riley et al., 2003). Following this eruption there was minimal activity at the volcano until 1999 when paroxysms began to occur again (Liu et al., 2020). An eruption cycle has been proposed which begins with lava flows from the summit, followed by strombolian activity which eventually finishes with a 1-2 day paroxysm (Lyons et al., 2010). This activity increased dramatically in 2015 and eventually culminated with an eruption on the 3rd of June 2018, which produced large pyroclastic flows down the flanks of the volcano resulting in a large number of deaths in surrounding communities (Naismith et al., 2019; Flynn and Ramsey, 2020). Understanding more about eruptive sequences at Volcán de Fuego itself is also of vital importance to those living in its vicinity, who are constantly at risk from these large paroxysms. Characterising eruptions can help with prediction and understanding of whether the volcano is entering a new eruptive phase (Liu et al., 2020).

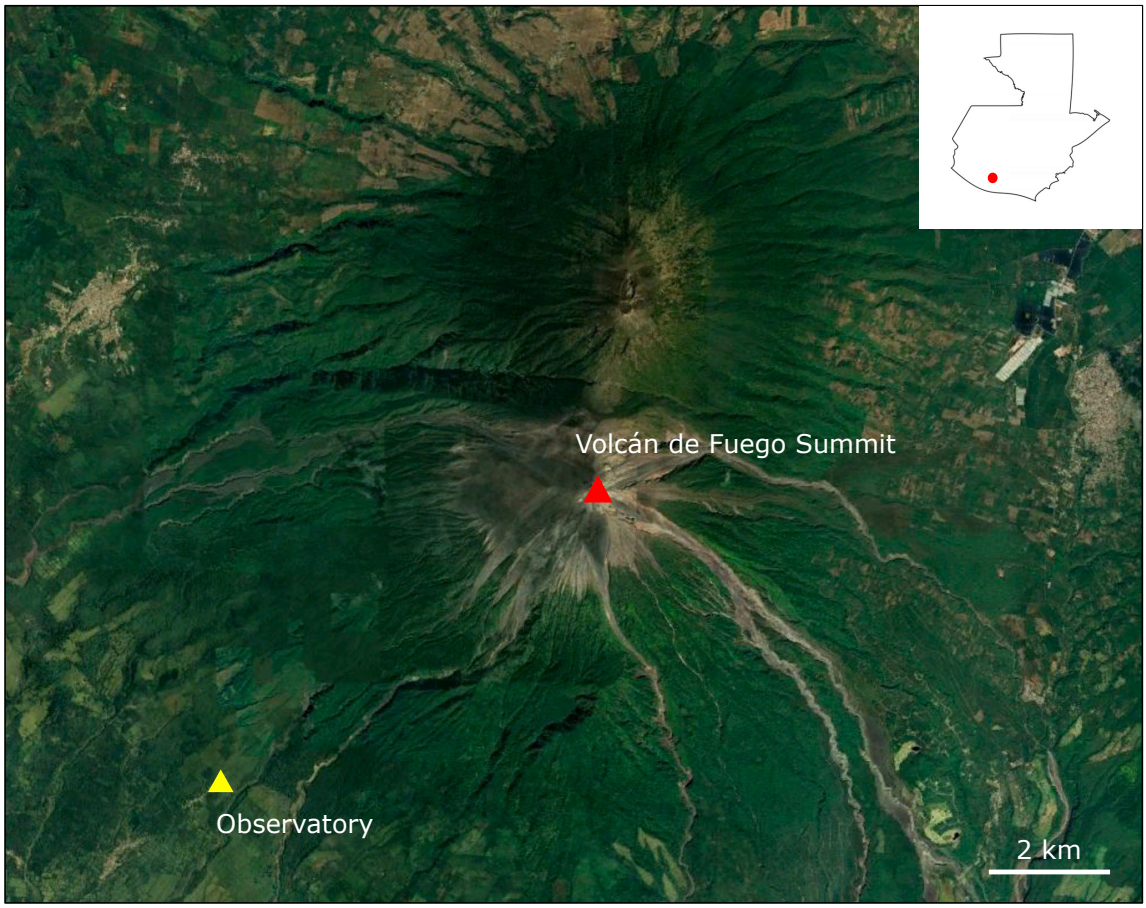

Figure 4.1: *A Google Earth map showing the location of Volcán de Fuego summit (red triangle) and the Fuego observatory (yellow triangle).*

Distally deposited Fuego ash samples (approximately 100 km from the vent) from the 14th of October 1974 have a medium grain size of 33.5 μm (Riley et al., 2003). Further samples from this eruption collected between 8 km to 60 km from the vent showed a decreasing medium particle diameter from roughly 3 mm down to 200 μm, however a few samples showed a small spike of particles sized between 16-63μm (Rose et al., 2008). Due to Fuego being located close to the coast of Guatemala, collecting distal deposits can be challenging as a large percentage of material can fallout over the sea.

Since 2018 there have been fewer paroxysms and currently at Fuego small eruptions occur roughly every 20 minutes. These eject enough ash to create conditions conducive to UAV ingress into the subsequent ash cloud, but do not limit operations. The University of Bristol also has a long standing relationship with the National Institute for Seismology, Volcanology, Meteorology and Hydrology (INSIVUMEH) of Guatemala, and the General Directorship of Civil Aviation (DGAC), making any legal and safety requirements around the use of UAVs

in the area easier to meet. These factors help make this volcano an ideal place to attempt collection of in-situ data from within a volcanic ash cloud.

There are a few previous studies which have been carried out using UAVs at Volcán de Fuego, these include: analysing the change over time of lahar channels by using a UAV to collect DEMs (Mock et al., 2023); looking at vertical wind-profiles from ground level to the summit of Volcán de Fuego (McConville and Richardson, 2023); using BVLOS (beyond visual line of sight) techniques to collect volcanic gas measurement (Wood et al., 2018); developing real-time planning routes for BVLOS UAVs (Schellenberg et al., 2019a) and using these techniques to collect ash (Schellenberg et al., 2019b); and finally the development of a "disruptor" to be used onboard an UAV to help with the collection of ash (Macleod et al., 2022) (the results of which are further discussed in this chapter).

During January 2022, fixed-wing UAV flights were carried out in Guatemala over Volcán de Fuego. On board the UAV was a Plantower PMS5003 sensor, able to capture PM1, PM2.5 and PM10 concentrations, as well as scanning electron microscope (SEM) stubs. The UAV was flown from the Volcán de Fuego observatory, climbing towards the volcano's summit and then circling through the ash cloud which is present, before returning to its launch/landing site. All flights lasted approximately 1 hour from takeoff to landing. This Chapter presents data from these flights, combining the SEM and PMS results to look at proximal and distal ash clouds, as well as analysing the effectiveness of the use of a "disruptor" when sampling particles on the SEM stubs. Figure 4.2 shows a view of the volcano on a clear day, taken from the observatory; the currently erupting plume can be seen as well as previous plumes which are still dispersing within the atmosphere.

Figure 4.2: *This photograph, taken from the observatory, shows an eruption occurring at Volcan de Fuego. An ash cloud from a previous eruption, still dispersing in the atmosphere, is outlined by a red dashed line.*

4.2 Data Collection

The uncrewed aerial vehicle used to collect data was a Skywalker X8 (Figure 4.3). It can take off with a total mass of 4.2 kg, reach speeds of 26 m/s and is able to fly to heights above 4000m. It also can have a GoPro attached to its body and front, allowing in-flight video to be captured. The PMS5003 and SEM stubs used in data collection during January 2022 are the same sensors as described in Chapter 3.

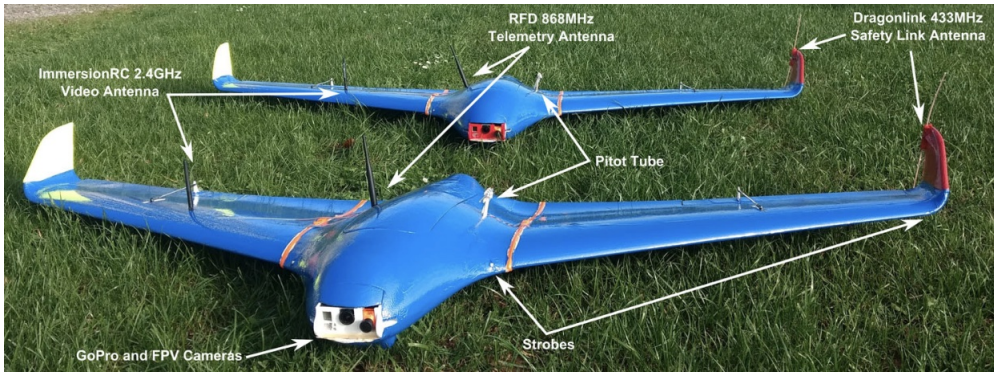

Figure 4.3: *An photograph of two Skywalker X8s taken from Schellenberg et al. (2019b). This is a large fixed-wing UAV, having a wingspan of 1.2 m. When attached, the stubs and PMS5003 are located on the top of the fuselage.*

All flights took off from the Fuego Observatory, as there is a field located next to the building which provides a relatively unhindered landing and take-off area. The UAV is launched by catapult and landed on a grassy airstrip. The rest of the surrounding area is densely vegetated making fixed-wing UAV operations difficult.

When the UAV was airborne the PMS5003 was run throughout the flight, continuously collecting data. However, the stubs are only exposed once the UAV has entered the targeted ash cloud and on leaving the ash cloud they are then returned to the fuselage to protect them from any further contamination. This can be seen in Figure 4.4, where two stubs have been deployed out of the fuselage; the PMS5003 is also present, having been attached to the front of the UAV. The two stubs can be deployed both simultaneously and individually, to allow different areas of the dispersing ash cloud to be sampled on each flight.

The flights analysed in this chapter are in summarised in table 4.1, which highlights how many stubs were collected from each flight, whether a disruptor was present, what area of the plume was sampled (proximal/distal) and whether the PMS5003 was present. The proximal cloud was always sampled close to the summit, as soon as possible after an eruption. The distal cloud varied in location as a result of wind influence after an eruption. If wind speeds were low, the distal ash cloud would be sampled closer to the volcano summit (as seen particularly during FL8). The distal cloud likely also contains ash from previous eruptions, whereas the proximal cloud should only contain ash from the most recent eruption. A reasonable estimate for proximal and distal ash sampling times after an eruption are < 8 minutes and > 30 minutes, respectively.

Flight no.	**No. of stubs collected**	**Disruptor (Y/N)**	**Proximal/Distal**	**PMS5003 Present (Y/N)**
FL5	2	Y and N	Both proximal	N
FL3	2	Y and N	Both proximal	N
FL15	2	Y and Y	1 proximal, 1 distal	Y
FL14	2	Y and Y	Both distal	Y
FL16	1	Y	Proximal	N
FL8	2	N and N	1 proximal, 1 distal	N

Table 4.1: *The flights conducted to collected PMS5003 and stub data during January 2022.*

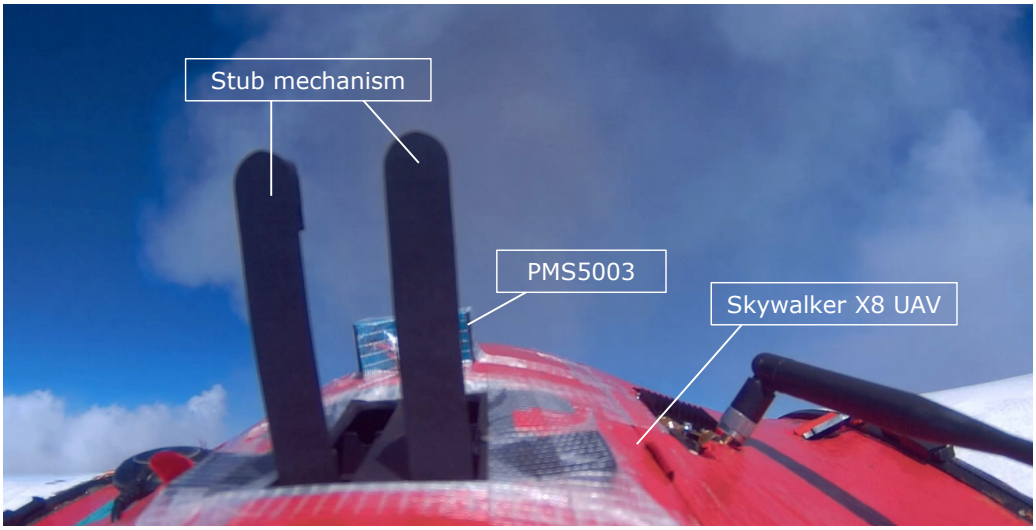

Figure 4.4: *This video screenshot shows the Skywalker X8 UAV mid-flight, with the stub mechanism having been deployed, as well as the PMS5003 attached to the front of the UAV.*

4.3 SEM Stub Analysis

The SEM stubs were processed in the same way as described in Chapter 3, starting with imaging in the SEM, following by stitching to create a full image, then processing in ImageJ. However, the locations of the 1 mm sub-samples differed slightly from the AB2 experiments where the centre of the stub was always used. The presence of the aerodynamic "disruptor" rendered this choice impossible due to a shadow created (see discussion). Through the steps carried out in ImageJ, this again allowed particle number distributions to be produced as well as a variety of other particle properties.

4.3.1 The Disruptor

As a standard the SEM stubs are directly exposed to the air flow during a UAV flight. However, some of the flights were carried out using an aerodynamic "disruptor" in front of the SEM stubs to interrupt the air flow, creating a baffle, as the UAV travels through the atmosphere (Figure 4.5).

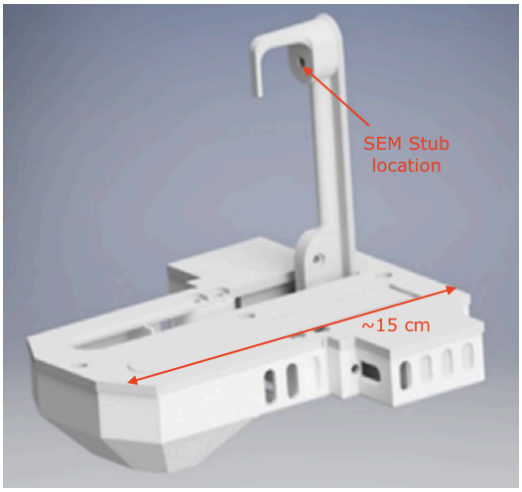

Figure 4.5: *This edited image from Macleod et al. (2022) shows a single disruptor mechanism, with the disruptor having been deployed. The mechanism can be designed to release two stubs together either both with the disruptor, both without or one with the disruptor and one without. The mechanism is attached to the top of the fuselage when in-flight.*

Fluid dynamics modelling has demonstrated (Macleod et al., 2022) that the disruptor can increase the chance of very fine (sub 3 μm) particle collection, as there is evidence for under-sampling of smaller particles when the stubs are directly exposed to the air flow. The disruptor allows eddies or vortexes to form behind it, encouraging particles to stick more efficiently to the stub. This is particularly noticeable at particle sizes of $\sim$ 1 μm (Figure 4.6), as it can be seen that collection efficiency of particles is dramatically increased from close to 0, to a value of 0.2 by the presence of a disruptor. As particle diameter increases, the collection efficiencies of the normal stub versus the disruptor converge, becoming the same at a diameter of $\sim$3 μm. Beyond this the collection efficiency is slightly higher for a normal stub compared to the disruptor stub, likely to be due to collisions between the stub and particles, until $\sim$10 μm, where the they become very similar, reaching a high collection efficiency of almost 1.

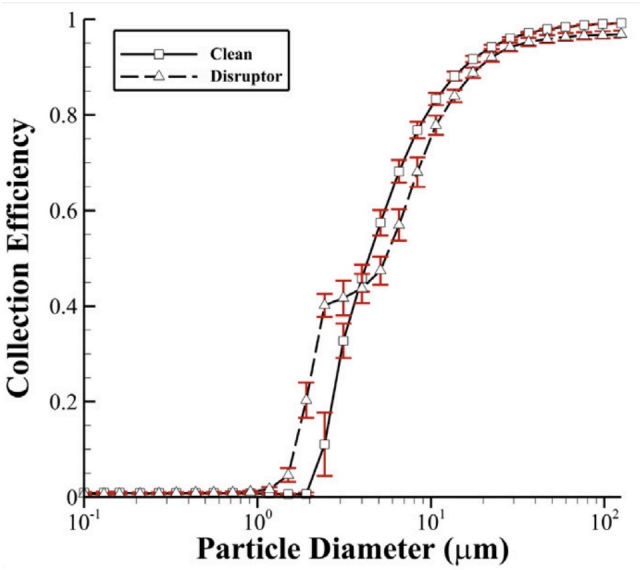

Figure 4.6: *This figure take from Macleod et al. (2022), shows the collection efficiency of particles, when there is disruptor present in front of the stub, versus there being no disruptor present.*

Flights 3 (FL3) (Figure 4.7) and 5 (FL5) (Figure 4.8) were carried out to allow a comparison between two stubs: one with a disruptor present and one without a disruptor present. The overall goal being to test whether a disruptor present in front of the SEM stub improves the efficiency of very fine particle collection, particularly those with a diameter of <3 μm. During these flights the two stubs were deployed simultaneously on entry to a proximal ash cloud. During FL3 the stubs were exposed for a total duration of 42 s and during FL5 they were exposed for 30 s. However, the exposure during FL5 was slightly different, as the stub mechanism was deployed twice, with a total exposure of 30 s.

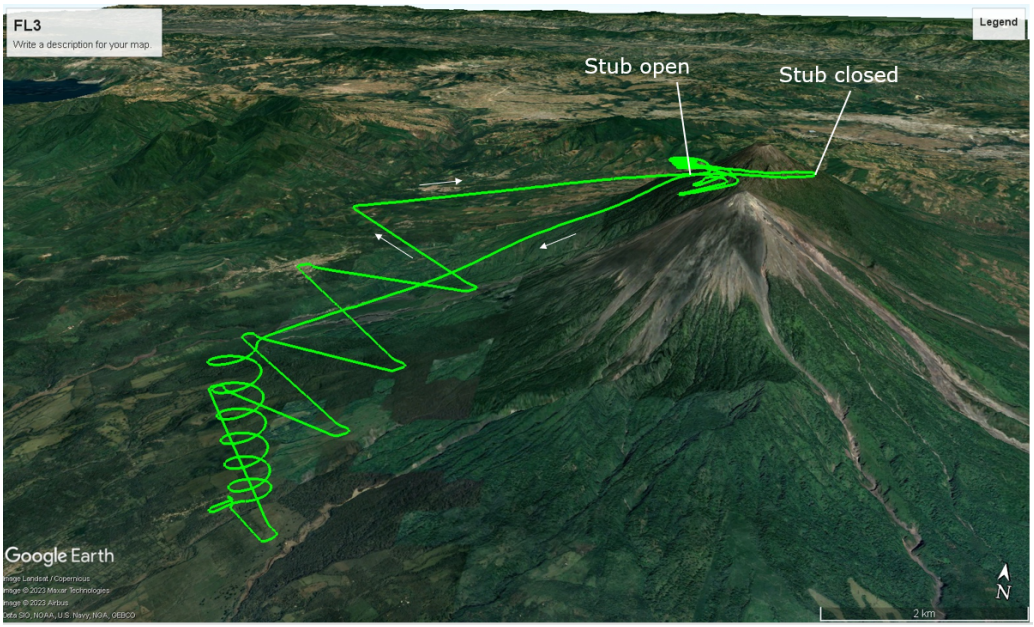

Figure 4.7: *The green line shows the UAV flight path for FL3, highlighting where stub was exposed.*

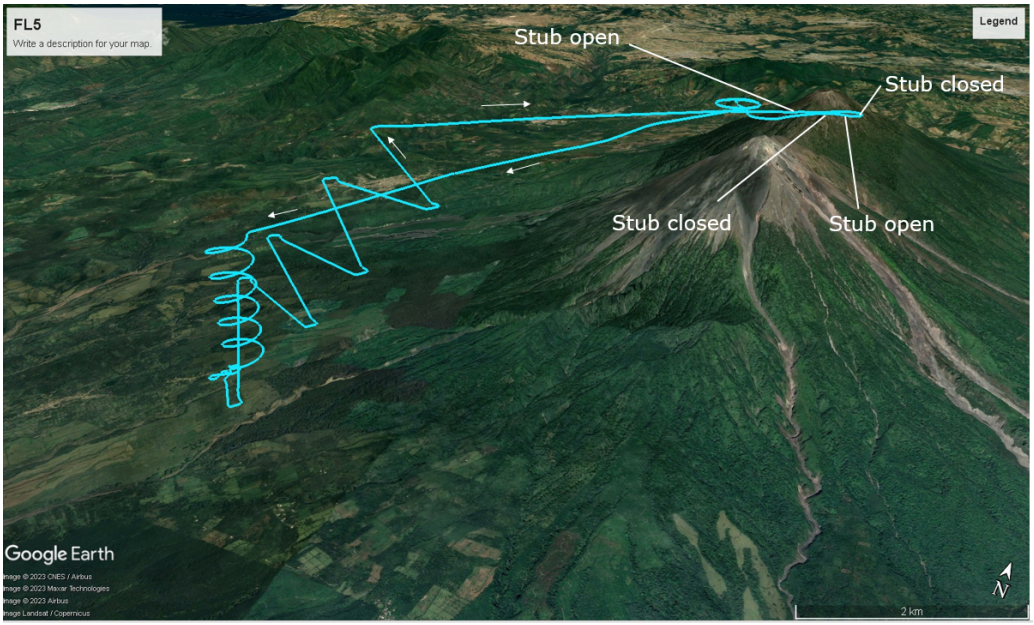

Figure 4.8: *The light blue line shows the UAV flight path for FL5, highlighting the multiple locations where the stub was exposed.*

Once the SEM stubs were acquired for FL3 and FL5, they were analysed to asses the impact of the disruptor. The section of the SEM stub imaged, at a magnification of x1000 from FL5, was taken from an area close to the disruptor shadow, but not within it, and from the same area on the stub where no disruptor was present. However, in order to look at a

different area of the stub from FL3, a 1 mm square was imaged closer to the edge of the two stubs. Figure 4.9 shows these stubs fully imaged in the SEM, with the disruptor shadow being highlighted in (b) and (d), as well the rough locations where the x1000 images were collected.

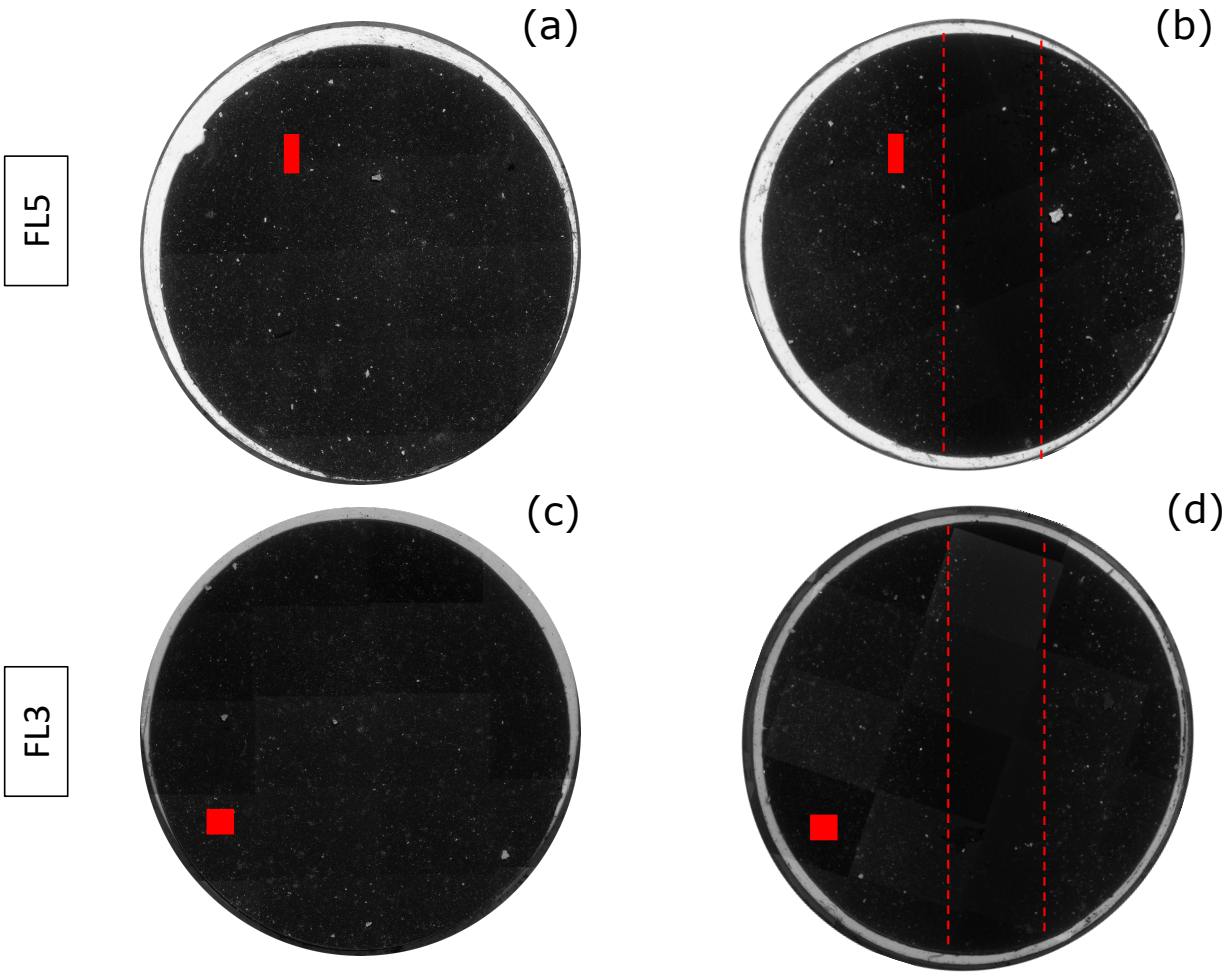

Figure 4.9: *The four stubs collected during flights 5 and 3, (a) and (c) show the stubs with no disruptor present; (b) and (d) show the stubs where the disruptor was present, with the shadow being highlighted by the red dashed lines. The red boxes present on the stubs show the rough area that was imaged in the SEM at a magnification of x1000, with the area imaged from FL5 being closer to the disruptor shadow, than the 1 mm square imaged closer to the edge of the stub from FL3.*

Flight	No. Particles on stub	Mean Diameter (μm)	% particles <10μm
FL5 (D)	12976	2.15	99.49
FL5	13741	1.73	99.43
FL3 (D)	16800	1.89	99.53
FL3	19882	1.71	99.66

Table 4.2: *Particle comparisons between the disruptor and no disruptor stubs from FL5 and FL3.*

By first visually inspecting the stitched images it could be seen that the disruptor stub from FL5 contained less particles and this was confirmed during further processing, with a difference of 12976 compared to 13741. For all the stubs almost 100% of particles present were < 10 μm. More particles were present on both the stubs from FL3, when compared to FL5, but as seen before, there was a greater number on the stub exposed without the disruptor. The total number of particles strongly relates to the exposure times of the two flights with the ratio of average number of particles (1.37) being close to the ratio of the amount of time the stubs were exposed for (1.4) for the two flights. The mean diameter was also higher for both stubs exposed with a disruptor present, but the values for FL3 were very similar, only being fractionally lower for the no disruptor stub.

Figure 4.10 shows the number percentage graphs for FL5 and FL3 for the distruptor and no disruptor stubs. Looking at FL5 it can be seen that the no disruptor stub has a larger percentage of particles in both the 0-1 μm bin and the 1-2 μm bin. However, FL3 does show a slight increase in the percentage of particles in the 0-1 μm bin when the disruptor is present, from 36% to 38%. There are however, a greater percentage of particles present in the 1-2 μm bin on the no disruptor stub (35%), compared to the disruptor stub (30%). Number % (size fraction) is often challenging to interpret as changes to the larger diameter bins also influences the smaller ones.

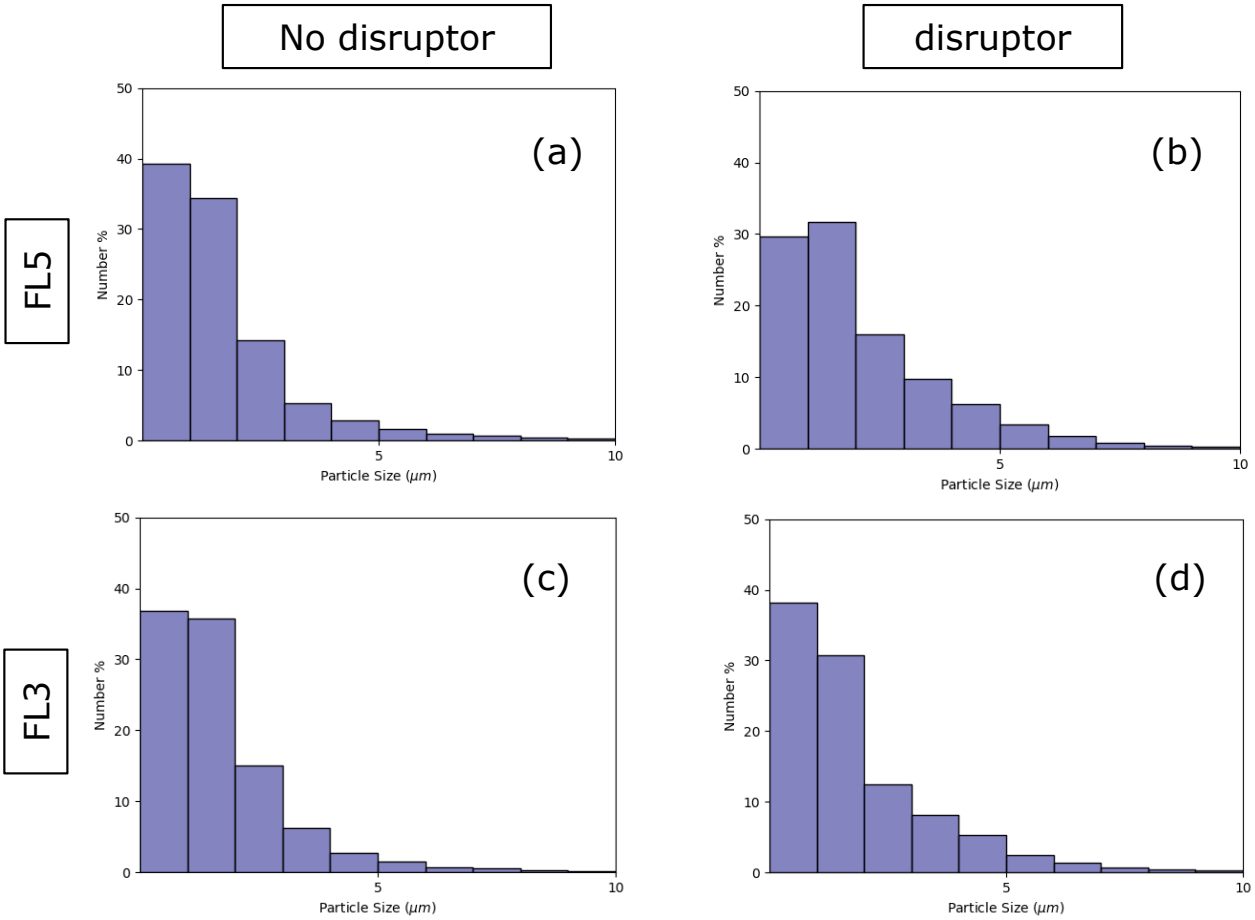

Figure 4.10: *These graphs show the number percentage of particles in bins from 0-10 μm from the four stubs analysed over flights 3 and 5. (a) shows results from FL5, no disruptor, (b) FL5 with the disruptor, (c) FL3, no disruptor and (d) FL3 with the disruptor.*

Given that sensitivity, the number of particles present in each bin for the four stubs was also analysed to see if, despite the percentage of very fine particles being less on the disruptor stub, there were more particle present overall in the very fine bins. Looking at Figure 4.11, it can be seen that this is not true with the no disruptor stubs always having a larger number of very fine (<1 μm) particles present. There is a significant decrease across all four stubs in the number of particles present between the 1-2 and 2-3 μm bins, with at least 60% of material always being below 2 μm diameter.

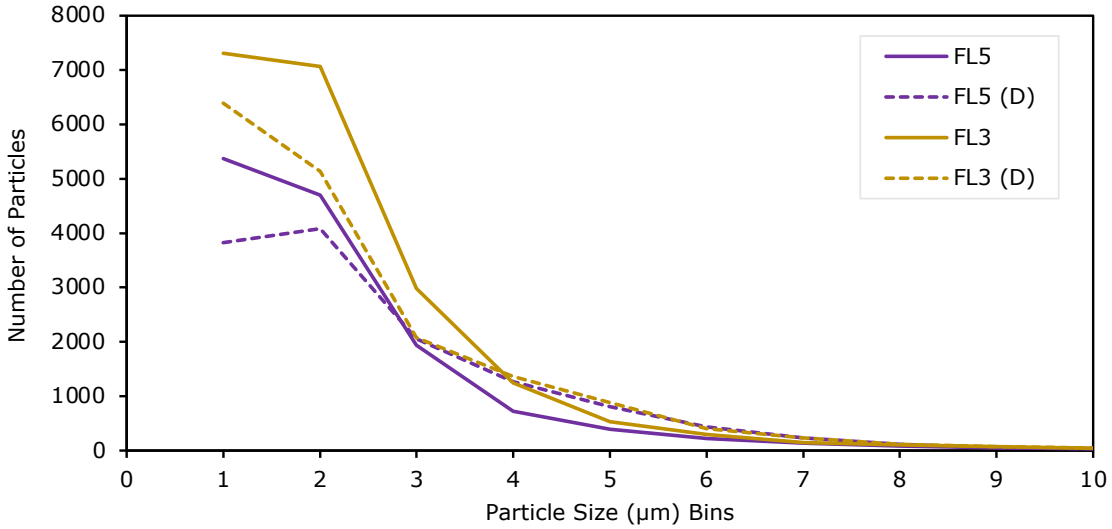

Figure 4.11: *This graphs shows the number of particles plotted against the particle size bins, with the purple lines representing FL5 and the yellow FL3. The solid lines and dashed lines show the presence and absence of the disruptor, respectively.*

Fluid dynamic models suggest that the presence of a distruptor should increases fine particle collection. Whilst FL3 results weakly support this hypothesis, data from FL5 suggests otherwise. Overall, this suggests that the effect of the disruptor for very fine particles is minimal.

4.3.2 Proximal Stubs

In addition to FL5 and FL3, in which all stubs were flown in a proximal cloud to look at the effect of the disruptor, three flights were flown where SEM stubs were deployed to exclusively look at proximal ash clouds. FL15 (Figure 4.12), FL16 (Figure 4.13) and FL8 (Figure 4.14) all had one proximal stub deployed in flight, collecting ash samples close to the summit of the volcano. The stub from FL15 was exposed for 179 s, the one from FL16 for 135 s and the one from FL8 for 11 s. When processed in the SEM a 1 mm square was imaged close to the edge of all three stubs (as seen in Figure 4.9, (c) and (d)), due to a disruptor having been present on flights 15 and 16.

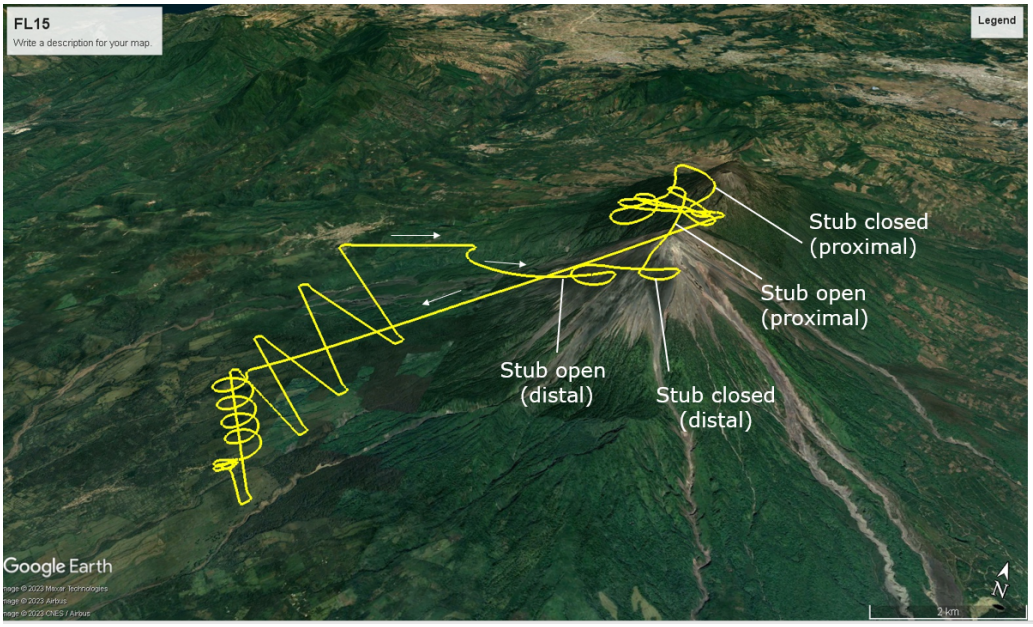

Figure 4.12: *The yellow line shows the UAV flight path for FL15, highlighting where stub was exposed, both at a proximal and distal location.*

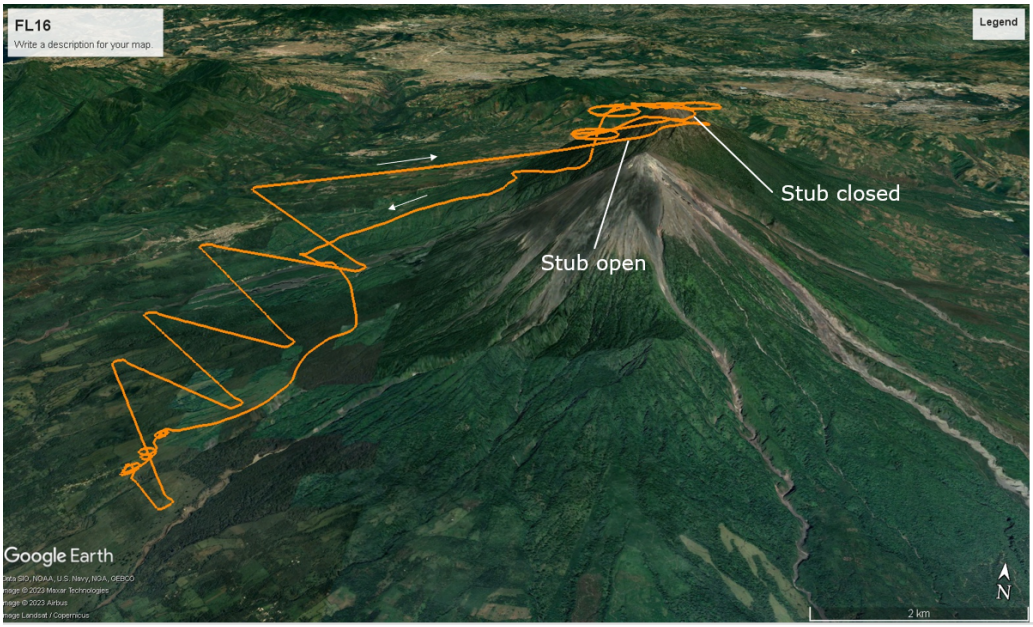

Figure 4.13: *The orange line shows the UAV flight path for FL16, highlighting where stub was exposed.*

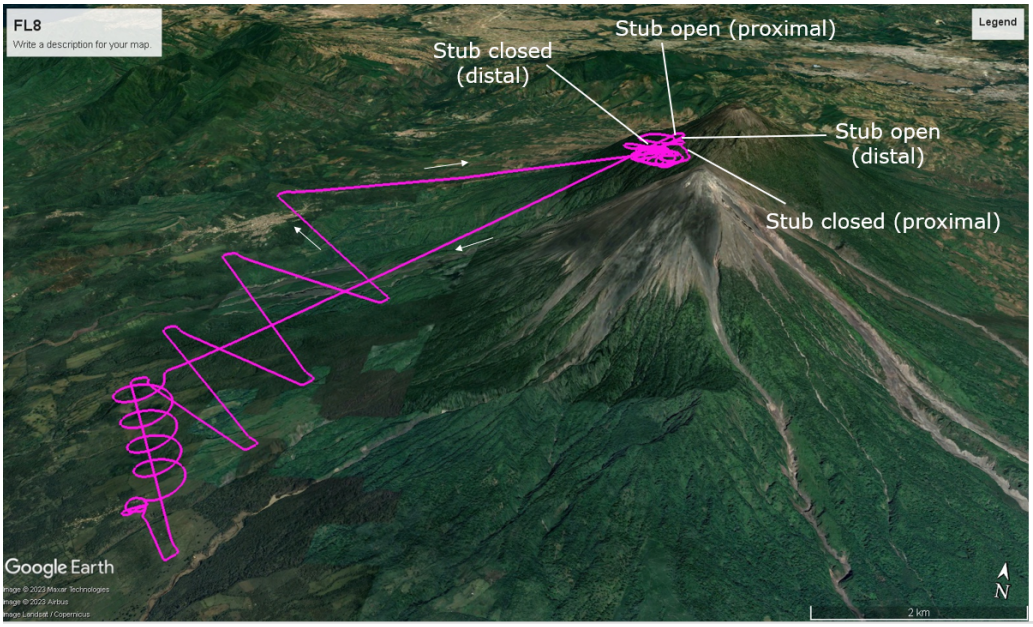

Figure 4.14: *The pink line shows the UAV flight path for FL8, highlighting where stub was exposed, both at a proximal and distal location.*

Flight	No. particles on stub	Mean diameter (μm)	% particles <10μm
FL8	21752	2.12	99.47
FL15	8662	2.04	98.98
FL16	16518	2.28	98.97

Table 4.3: *Particle comparisons between the proximal stubs from flights 8, 15 and 16.*

The number percentage distributions and percentage particle coverage graphs from these stubs are presented in Figure 4.15. The percentage in the 0-1 μm bin for FL15 is slightly increased at a value of 35% compared to 28-29% for flights 8 and 16. The percentage particle coverage is also very similar for FL8 and FL16, with it being almost halved for FL15. This suggests that, although the exposure time for FL15 was longer, the ash cloud may have been more dilute. Alhtough FL8 and FL16 have very diferent exposure times, the number % graphs and, interestingly, the % coverage pie charts are much more similar.

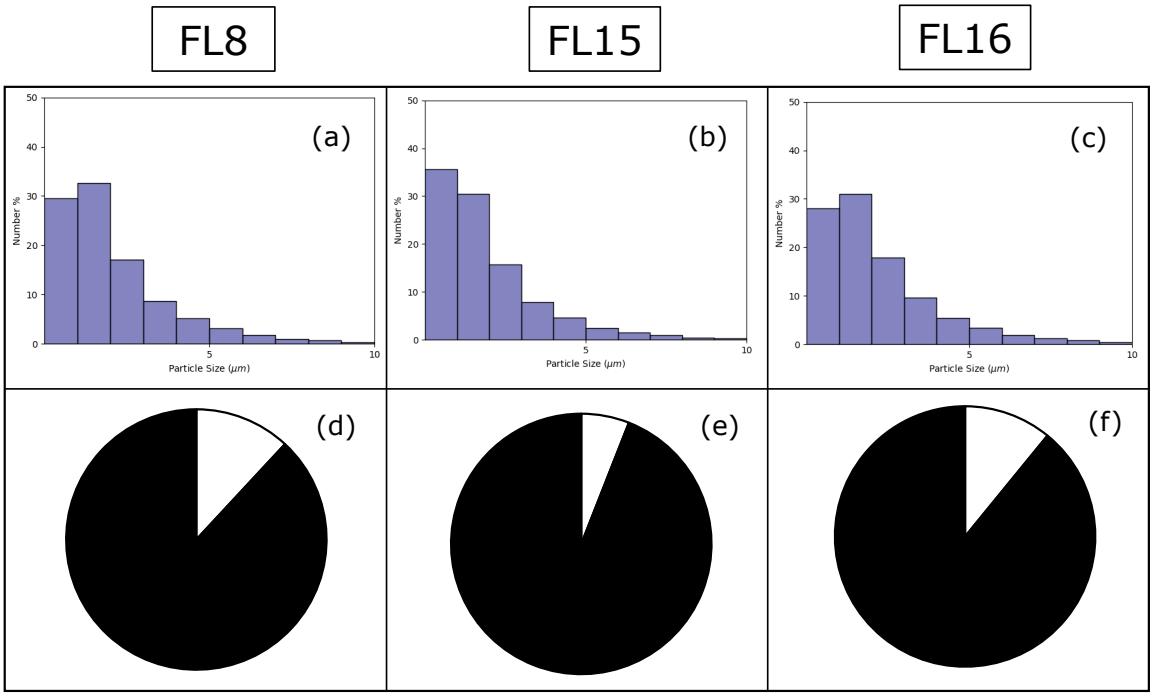

Figure 4.15: *This figure shows the number percentage (a)-(c) and percentage particle coverage (d)-(f) graphs for the proximal flights 8, 15 and 16.*

4.3.3 Distal Stubs

There were three flights where SEM stubs were deployed in a distal ash cloud, with four stubs being exposed. On visual inspection these stubs do not show a strong coating of ash, with the carbon backing of the stub looking almost unchanged from its pre-flight condition. FL15 and FL8 had one distal stub deployed in-flight, whereas FL14 (Figure 4.16) had two distal stubs deployed simultaneously in-flight. During FL15 the stub was exposed intermittently for 84 s and during FL8 the stub was exposed for 21 s. The two simultaneously deployed stubs on FL14 were exposed for 127 s. On analysis in the SEM, there were too few particles present on the stubs from FL14 and FL15 to allow stitching to to be carried out. Figure 4.17, (a) and (b) shows images taken in the SEM of the stubs from FL14 and FL15, where there are very few particles present, and those that are present being >100 μm in size. However, Figure 4.17, (c), shows a SEM image taken of the stub from FL8 and although the particle density is low, there are visibly considerably more particles present than on the images from FL14 and FL15.

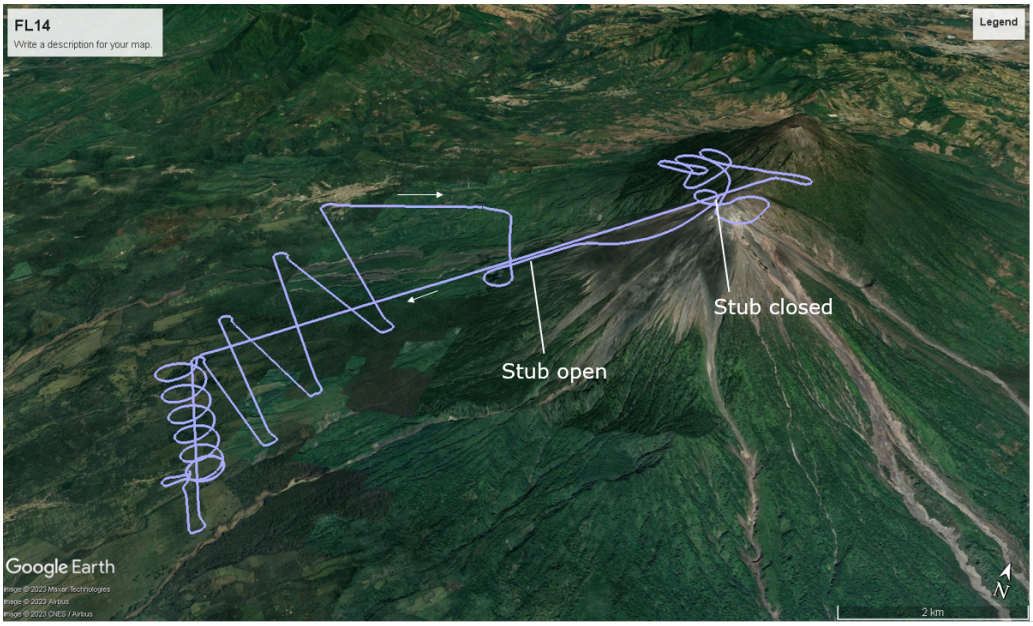

Figure 4.16: *The blue line shows the UAV flight path for FL14, highlighting where stubs were exposed.*

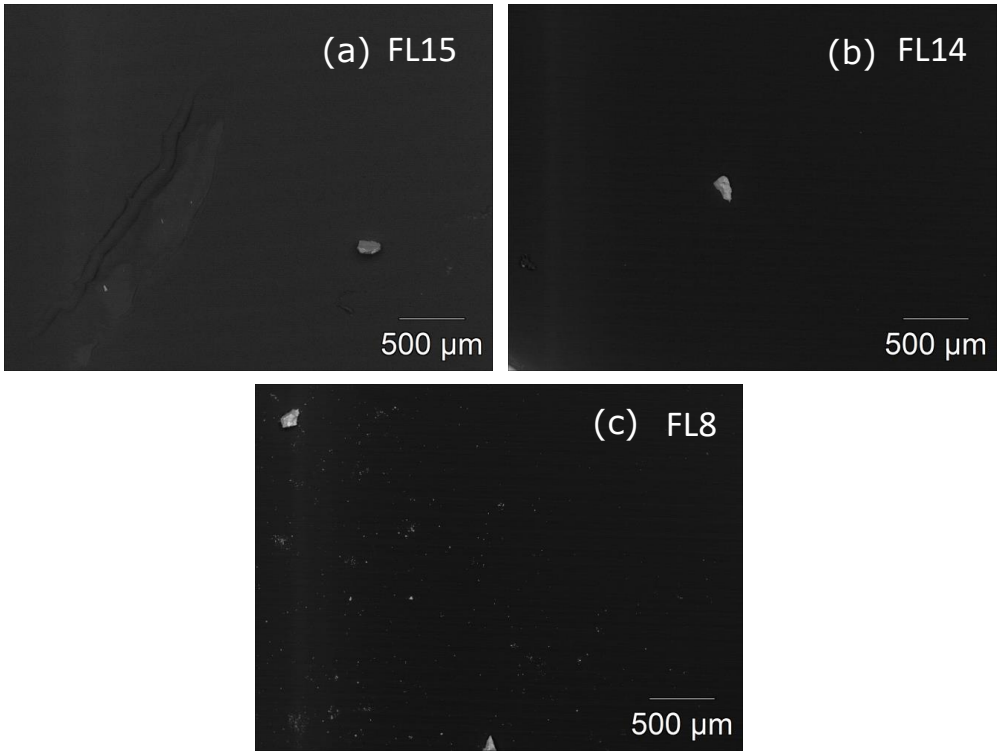

Figure 4.17: *These SEM images show images taken of the distal stubs from (a) FL15, (b) FL14 and (c) FL8. All three images highlight the sparseness of particles with a slightly higher coverage being visible on the image from FL8.*

There were enough particles present on the distal stub from FL8 for the images collected at x1000 magnification to complete stitching in ICE. This allowed a particle number distribution graph to be produced, along with the percentage particle coverage (Figure 4.18). The total number of particles present on the stub is low (1799) when compared to other flights and this is reflected in the percentage particle coverage which is lower than seen on any previous stub, either collected in-situ or during the AB2 experiments in Chapter 3. The number percentage graph shows that 31.5% of particles are <1 μm and a further 26% are between 1-2 μm. However, there are no particles present between 8-9 μm, which has not been seen on any previous stubs, with particles always having been present in every bin.

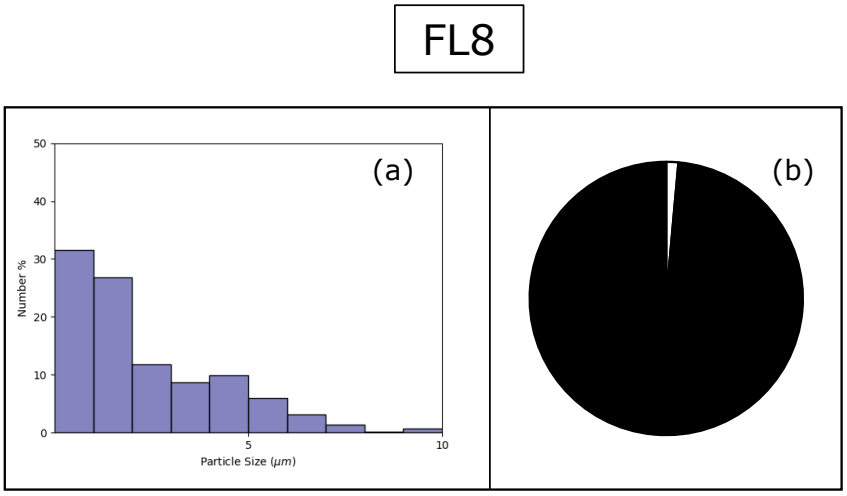

Figure 4.18: *(a) Number percentage graph and (b) percentage particle coverage graph of the distal stub from FL8.*

4.4 PMS5003 Sensor Data Analysis

4.4.1 Overall Flight Analysis

A total of two complete flights (FL14 and FL15) were flown carrying a PMS5003 onboard, collecting in-situ measurements of PM1, PM2.5 and PM10. Looking at the PM10 measurements for FL15 (Figure 4.19 (a)) it can be seen that there is small prolonged spike in PM10 (with a peak of $\sim$ 180 μg/m^3) from 974 s to 1860 s; this is coincident with the final preparation and take off of the UAV, and subsequent climb through the atmospheric boundary layer, which is contaminated with a mixture of remobilised particles, such a soils, pollen, biomass burning and

volcanic ash. The same occurs during FL14 (Figure 4.19 (b)) from 656 s to 1510 s, except this time a peak of only 133 $\mu g/m^3$ is reached and the overall readings stay at a lower level. The singular spike could again be a result of dust being mobilised around take off. In both cases, these continuous low readings are followed by a drop to 0 then small spikes in concentration as the UAV enters a distal ash cloud. When the UAV enters the proximal ash cloud during FL15, closer to the volcano summit, there are discrete spikes as the UAV enters areas of high ash concentration, with values in between dropping to almost 0 $\mu g/m^3$, delimiting very clean air above the boundary layer at $>$ 3500 m.a.s.l. Peaks in concentration occur between 2400 s and 2930 s, reaching a peak of 1762 $\mu g/m^3$ at 2589 s. After 2930 s, there is a singular spike believed to be a result of an encounter with a distal ash cloud followed by more continuous low concentration readings, indicative of the UAV re-entering the boundary layer, before returning to the observatory. FL14 experiences a similar pattern with spikes of high concentration being separated by readings falling to almost 0 $\mu m/m^3$. The maximum value reached during this flight is 2446 $\mu g/m^3$ after 2395 s; this spike however is followed by one other spike of 1058 $\mu g/m^3$ at 2471 s, which is a result of the UAV entering a distal ash cloud. These spikes are then followed by a longer duration of lower readings as the UAV re-enters the boundary layer and returns to the observatory. For FL15, and to a certain extent FL14, the lower concentration time series are broadly symmetrical (although the return flight path is different).

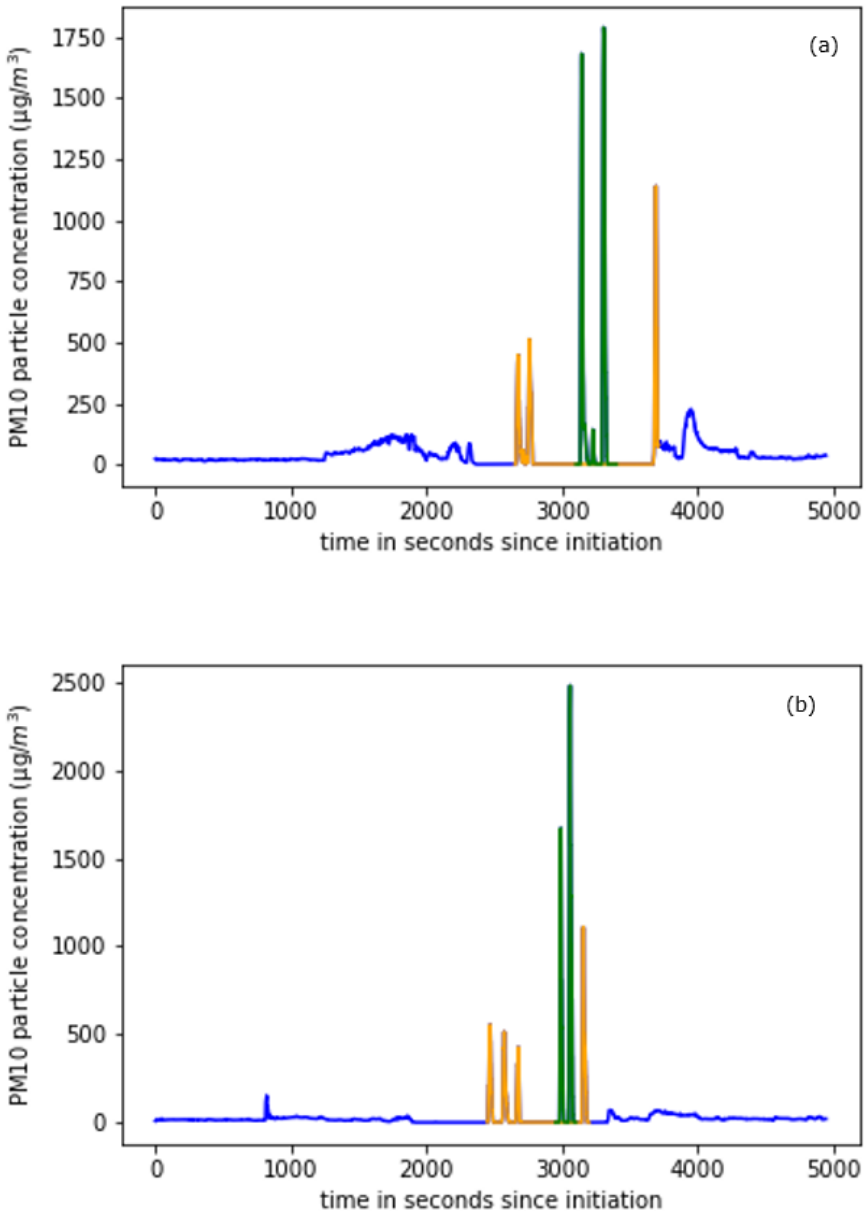

Figure 4.19: *The PM10 data from the PMS5003 for (a) FL15 and (b) FL14 plotted over the entire UAV flight. The blue area highlights where the UAV comes into contact with the boundary layer, the orange area marks contact with the distal ash cloud and the green area is when it is within the proximal cloud.*

4.4.2 Distal and Proximal Ash Clouds

The PMS5003 readings also show that when the distal ash cloud is encountered it contains a higher percentage of fine ash for an equivalent concentration. By initially examining the videos from the flights, the overall flight readings could be separated into areas where the UAV was in

contact with the boundary layer, the distal (dilute) ash cloud and the proximal (concentrated and optically thick) ash cloud. The particulate matter data were then extracted from these areas and plotted against each other to look at the ratios within the different regions (Figure 4.20).

Looking at both flights it can be seen that there are discrete differences in particle size ratios between the boundary layer, the distal ash cloud and the proximal ash cloud. This is slightly more noticeable during FL14, where Figure 4.20 (c) shows a clear difference between the ash in the distal and proximal clouds, with the distal cloud containing a larger proportion of PM1, compared to the ash within the proximal cloud. This trend can also be seen during FL15 in Figure 4.20 (a); the data points between the distal and proximal clouds are slightly less discrete but still show a greater proportion of PM1 within the distal cloud, compared to the proximal cloud. Both flights show distinct evidence for the UAV coming into contact with very fine grained material within the boundary layer, as this data sits clearly on its own and closer to the PM1 axis.

Looking at Figure 4.20 (b) and (d), these show that for both flights there is very little variation across the different regions (boundary, distal, proximal) for PM2.5 and PM10, with the data from the three areas falling into alignment. This potentially also implies that a large proportion of the material present is less than 2.5 μm in size.

The data show that larger particles are present closer to the volcanic vent. The boundary layer particles are consistently relatively higher in PM1 with proximal ash clouds having the highest proportion of PM10. The larger particles might be somewhat depleted in the distal cloud due to fall out and undergoing sedimentation or by aggregation, although the sedimentation rate of PM10 is very slow and aggregates were not observed during flights FL14 and FL15. It is however worth noting that the aggregation processes appears to happen rapidly within meteorological cloud (see Chapter 5) and that that process would remove PM10 preferentially over PM1. Given the proxmial and distal acquisitions where quite close in space and time, but may be sampling different explosive events of slightly different scales, one other consideration is that the initial particle size distribution of different events varies in fine ash content.

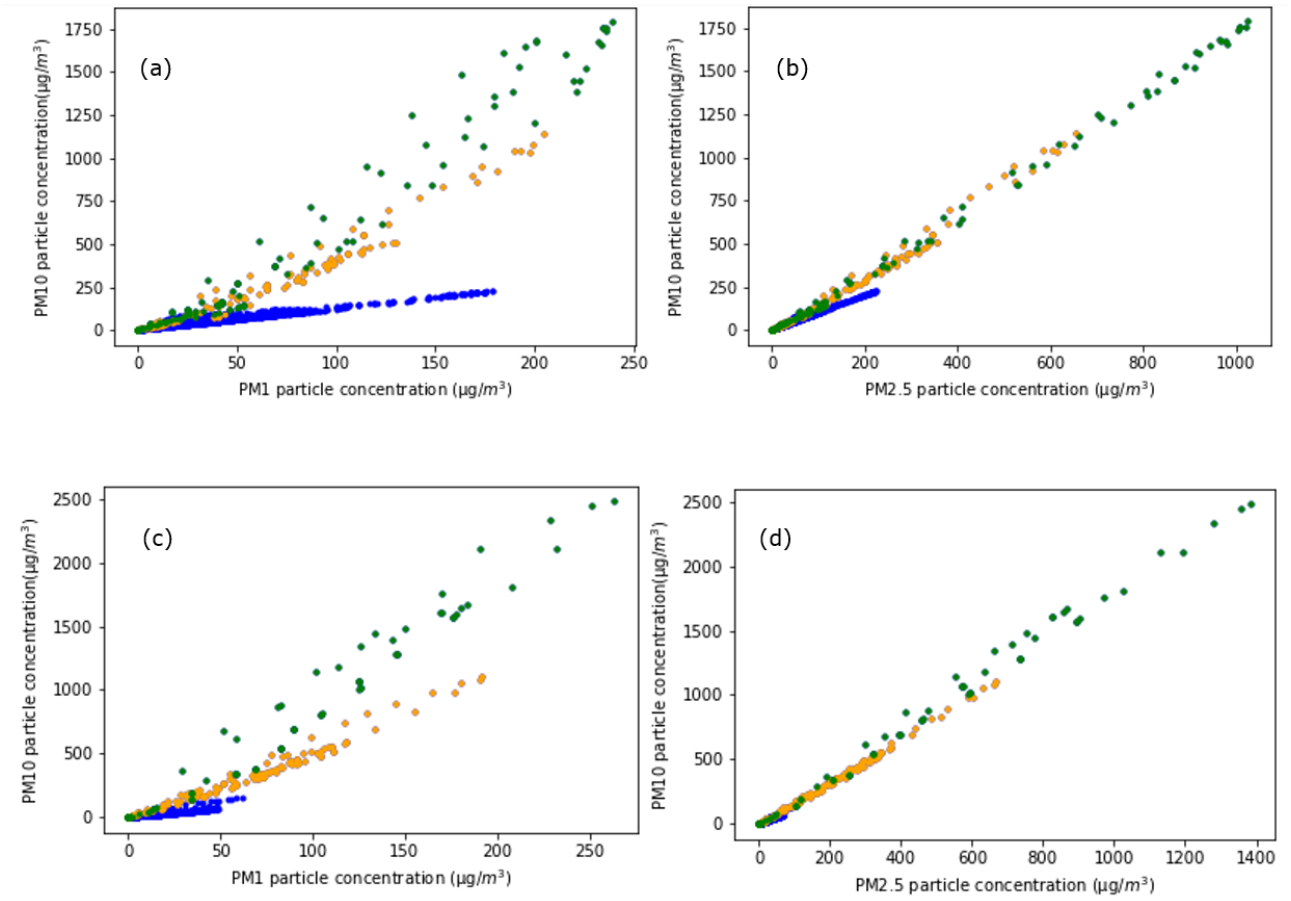

Figure 4.20: *These four plots show PM readings within the boundary layer (blue), the distal ash cloud (orange) and the proximal ash cloud (green). Plots (a) and (c) compare PM10 readings with PM1 readings; plots (b) and (d) compare PM10 readings with PM2.5 readings. Plots (a) and (b) show data from FL15 and plots (c) and (d) from FL14.*

4.5 Discussion

It has been demonstrated that it is possible to both collect in-situ samples of particulate matter and measure real-time concentrations of ash particle samples at close proximity to volcanic vents using UAVs.

4.5.1 Distal versus proximal discussion

The low percentage particle coverage seen on the SEM stub from FL8, which travelled through the distal ash cloud is to be expected; as confirmed by the PMS5003, concentrations are lower in the distal ash cloud. These lower concentrations also contain a larger percentage of PM1

when compared to PM10 than the proximal flights, which is to be expected as smaller particles have the ability to travel greater distances. The stubs from FL14 and FL15 also contained a very minimal coating of ash, with only very disperse, < 100 μm particles being captured. The percentage number distribution from the distal FL8 stub is also unusual as there are no particles between 8-9 μm in size, which has not been observed on any other flight. This could imply that there are processes changing the overall particle size distributions as the cloud disperses over time.

The PMS5003 readings from the proximal clouds show much higher concentrations than the distal readings. The high values also tend to be over short timescales (~ 60 s) as the UAV briefly enters the proximal ash clouds. These spikes are also observed when the UAV enters the distal ash cloud, but the maximum values are significantly lower. The spikes potentially suggest that the ash cloud is still dispersing within the atmosphere, eventually mixing with the boundary layer as well as more broadly in the surrounding atmosphere. The proximal stubs from flights 8, 15 and 16, also show a much greater percentage coverage of particles, when compared to stub from distal FL8.

4.5.2 Further analysis of the effect of the disruptor

Number percentage calculations were carried out for both the disruptor and no disruptor data for flights 3 and 5. This then allowed the collection efficiency correction (Macleod et al., 2022) for the disruptor to be applied in order to work out what the stub would be collecting if 100% of particles were collected. Figure 4.21 shows these data plotted and it can be clearly seen that applying the correction factor significantly increases the collection of particles <1.5 μm.

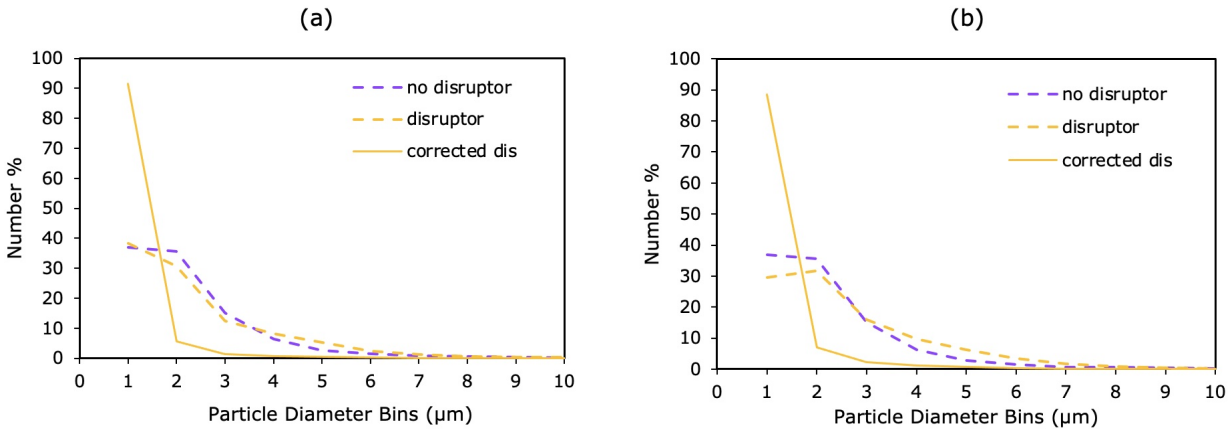

Figure 4.21: *These graphs for (a) FL3 (b) FL5 show the number percentage for each bin plotted for the disruptor and no disruptor data, as well as the corrected percentages for the disruptor stub.*

Although other flights were carried out with disruptors present, it is difficult to make direct comparisons, as the stubs from FL15 were not exposed simultaneously and the stubs from FL14 were unable to be analysed at a magnification of x1000 magnification.

There is mixed evidence surrounding the effectiveness of the disruptor in increasing the proportion of very fine particles collected. Fluid dynamical modelling suggests that due to the disruptor allowing eddies to form, slowing down particles, they should find it easier to stick (Macleod et al., 2022). However, evidence from the stubs that were flown at Volcán de Fuego show that this is not necessarily true and that the disruptor may actually be making only a very negligible difference.

4.5.3 Direct PMS5003 and Stub Comparisons

The data from flights 14 and 15, after some rebinning, allow for a direct comparison between PMS5003 and SEM stub data. The ash cloud concentrations were low enough when the distal stubs were exposed during flights 14 and 15 that an insufficient amount of ash was collected on the SEM stubs to allow for stitching. However, when FL15 entered the proximal cloud, there was enough ash present to permit the creation and stitching of a 1 mm grid taken at x1000 magnification, which allowed further processing.

The percentage mass was then calculated for FL15 for both the stub results and the PMS5003 data. The stub data were re-binned (as described in Chapter 3) to look at PM1,

PM2.5 and PM10, allowing easier comparisons between the two sensors. The PMS5003 data were averaged over the same time as where the stub was exposed.

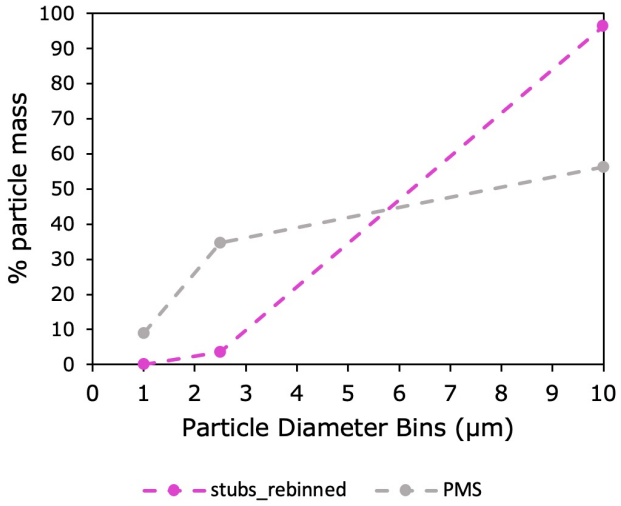

Figure 4.22: *This graphs shows the comparisons in percentage particle mass between the PMS5003 (grey line) and stub (pink line) from the proximal FL15 data.*

Looking at figure 4.22, this shows that again that the stub is still perhaps under sampling very fine particles if the PMS5003's error at sampling ash particles < 3 µm are assumed to be lower. This confirms the first observation from (Macleod et al., 2022) that fine particles are challenging to collect. If the aerodynamic disruptor does increase the likelihood of particle-stub interaction, the data acquired from Fuego suggest this enhancement is small in terms of size fraction and negligible in terms of mass fraction.

4.5.4 Comparisons to AB2

To a first approximation the stubs collected during the field campaign show similar patterns to those exposed to ash in AB2. Exposure time and concentration, reflected as a distance in the AB2 experiments, control coverage, with an optimal coverage sometimes being quite challenging to achieve in the field, given controls, one of which (concentration) is poorly known in real-time. The distal stubs from flights 14 and 15 (Figure 4.17) and the 90 cm exposures from the AB2 experiments demonstrate that, even for long exposures relative to the overall flight time spent at or above summit altitude, there can be insufficient particles collected to perform a robust analysis.

4.5.5 Uncertainties and Improvements for Future Flights

Uncertainties around ash capture onto the SEM stubs were considered in Chapter 3. Although those uncertainties pervade, additional processing and experimental considerations mean that uncertainties should be reconsidered to reflect those additional challenges.

For high coverage stubs the presence of larger particles masking smaller particles leads to separation of individual particles in ImageJ being difficult to carry out. This is highlighted in Figure 4.23, which contains two images from the FL8 (proximal) stub, with (a) showing an area where it is difficult to tell apart the individual particles, and (b) showing a larger particle masking smaller particles underneath. Interestingly, Figure 4.23 also shows good evidence for fragmentation by breaking of bubble walls (a) and fracturing along planes of weakness (b).

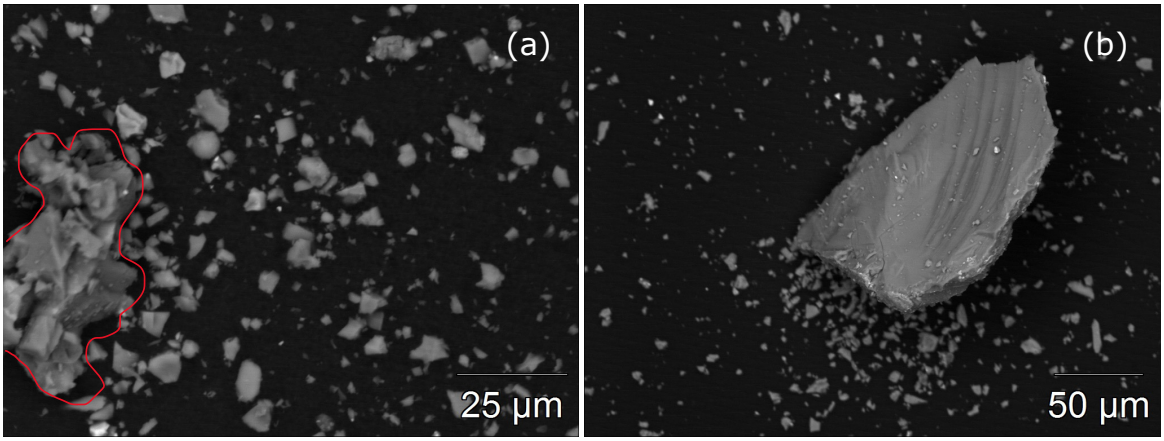

Figure 4.23: *(a) These SEM images show (a) an area (outlined in red) which can be difficult to separate once thresholded, due to overlapping particles and (b) a larger particle sitting on top of a number of smaller particles, meaning they are never counted.*

Further flights could be carried out to again test the efficiency of the disruptor, as the data from flights 3 and 5 are not fully conclusive as to its effectiveness. A variation of exposure times and concentration would broaden the parameter space but indicate under what circumstances, if any, the disruptor improves collection efficiency.

Further flights comparing the PMS5003 and stubs would also be beneficial in order to understand more about the ash which the PMS5003 is sampling. They would also allows further testing and comparison with AB2. Specifically, if the PMS5003 data could be telemetered in real-time then dosage (concentration x exposure time) could be tuned for better processing. Too little ash and the stitching of SEM frames doesn't work and too much ash increases errors

due to the need for manual separation of ash grains and masking effects.

If functioning real-time sensors were available on commercial jets, they could provide extremely valuable in-flight data to pilots, allowing them to be aware of particulates they are potentially flying through and to take any precautionary action. The Skywalker X8s are very slow moving compared to commercial jet aircraft, which is good for data collection but makes it harder to draw conclusions as to whether these sampling methods would be effective at higher speeds. It would be possible to design an inlet system capable of slowing down the speed of approaching air before it reaches the sensors.

4.6 Conclusions

UAV flights over Volcán de Fuego in January 2022 collected novel in-situ PM data, close to an erupting volcano. These data, collected via a PMS5003 simultaneously exposed with SEM stubs, allows new insights into how to monitor ongoing processes within volcanic plumes. A disruptor, placed in front of an SEM stub whilst collecting ash samples mid-flight, was also tested to analyse if its presence increased very fine particle collection.

The following conclusions can be drawn from this chapter:

- Particle coverage on the SEM stubs can be extremely low in distal ash clouds. Only images from FL8 were able to be stitched together with the stubs from flights 14 and 15 containing too low a particle density (Figure 4.17) to allow image stitching and further processing to be carried out. The percentage particle coverage from FL8 (Figure 4.18 (b)) is the lowest seen across all the stubs processed during the AB2 experiments and the UAV flights.

- The stubs from all the proximal flights were able to undergo image stitching and show a considerably greater percentage particle coverage (Figure 4.15 (d), (e) and (f)), than the distal stub from FL8. There was also consistency between FL8 and FL16, with both their particle number concentration graphs and percentage particle coverage charts showing similarity.

- The OPC based approach was more effective at capturing differences in particle size and concentration across the UAV flights, with readings showing strong evidence for a discrete

boundary layer in the atmosphere; whilst still delimiting between the distal and proximal ash clouds (Figures 4.19 and 4.20).

- There is mixed evidence surrounding the effectiveness of the disruptor, with the number percentage in the <1 μm bin increasing whilst the disruptor is present for FL3, but decreasing whilst the disruptor is present during FL5 (Figure 4.11). The mean particle size across the stub is also always higher when the disruptor is present (Table 4.2).

Chapter 5

In-situ Observation of Ash Aggregates in Volcanic Ash Clouds

5.1 Introduction

Aggregation occurs when volcanic ash particles, formed as a result of magma fragmentation, stick together during transport to form a larger structure. The nomenclature around this process is somewhat unclear with Brown et al. (2012) proposing a scheme to describe them based upon their structure, in order to move away from previous schemes which use size. Aggregates can have a range of shapes which are often dependent on how the individual particles form and are held together, with formation processes are often described as "wet" or "dry". Broadly, Wet involves the sticking of ash particles through the surface tension of water and dry formation occurring due to electrostatic forces (James et al., 2003).

After the 1980 eruption of Mount St Helens, ash aggregates were observed in the form of poorly sorted clusters and travelled distances of up to 644 km (Sorem, 1982). They were mainly composed of grains in the 10-20μm range, however there were also smaller particles than this present on top of the larger grains; these aggregates are thought to have been able to travel large distances due to their porous nature giving them a lower density then an individual particle of a similar size Sorem (1982). Furthermore, aggregation has been used to account for second thickening of deposits at Mount St Helens (Carey and Sigurdsson, 1982; Armienti et al., 1988).

Aggregates have also been observed in ash deposits from the 2009 eruption of Redoubt volcano, with samples having been collected at a minimum of 15 km from the vent (Wallace

et al., 2013). These aggregates which varied in size up to a diameter of 10 mm, were found extensively within the deposits and are thought to account for a large volume of fine ash falling out prematurely (Wallace et al., 2013).

The Brown et al. (2012) classification scheme subdivides aggregates into two categories: Accretionary Pellets (AP) and Particle Clusters (PC). Although Brown et al. (2012) move away from categorisation of accretions by size and formation mechanism, it is generally accepted that these categories are broadly differentiated by how the particles within the aggregate stick together; with AP having stronger bonds involving water and PC being associated with electrostatic forces (Vecino et al., 2022).

AP and PC are then further differentiated into six subcategories, based upon their internal structure only (i.e. independent of mechanism). PC(1) tends to consist of poorly bonded particles which often fall apart on impact and PC(2) are an individual particle which is covered in smaller particles, some of which are observed in the stubs of previous flights (see Chapter 4) but not discussed further here. PC(3), also called cored clusters, is a category of aggregate suggested by (Bagheri et al., 2016) which form when a central core particle is coated in finer particles; however, due to their fragile nature, they have not been observed in deposits, only captured in-situ on adhesive tape. AP(1) are poorly sorted and fragile whereas AP(2) have a core of generally larger (often poorly sorted) particles with a finer particle rim and AP(3) are liquid water drops containing poorly sorted ash (Brown et al., 2012).

There are generally four ways particles can continue to grow as a result of interaction with water: wetting and nucleation, layering, coalescence, and slurrying (Van Eaton et al., 2012). Wetting and nucleation involves two potential mechanisms where either a single larger droplet coats particles or the individual ash particles develop a rim of liquid water; layering is when particles bond to the outside of an already formed structure; coalescence is when malleable particle bundles held together by liquid water collide to form a larger structure; and slurrying occurs when aggregates become increasingly malleable to the point where they behave like a fluid (Figure 5.1).

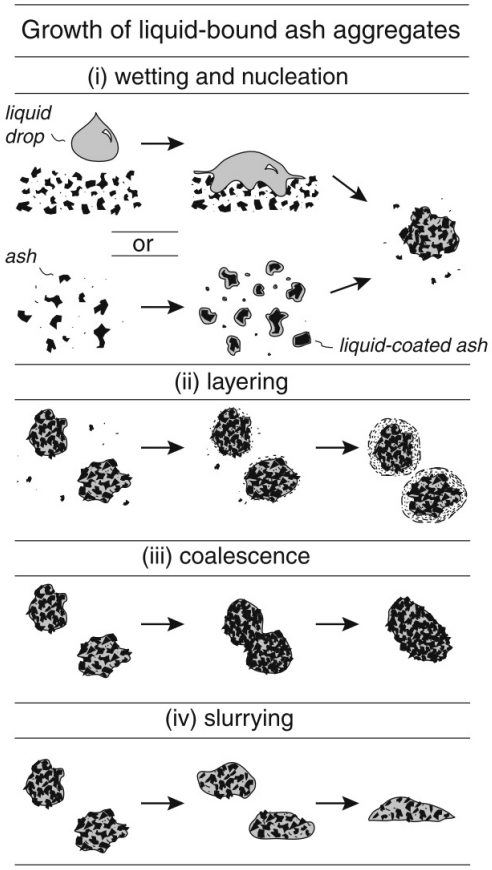

Figure 5.1: *Mechanisms of aggregate growth through four different stages: wetting and nucleation, layering, coalescence and slurrying (Van Eaton et al., 2012)*

Despite being poorly understood in parts, aggregation is nevertheless an important mechanism within ash clouds, as particles sticking together to form a larger structure can change the speed at which sedimentation occurs and hence change the overall lifetime of volcanic ash in the atmosphere. Not considering the aggregation of fine ash (<63 μm) can result in over estimation of distal particle transport and under estimation of sedimentation close to the eruption source (Rose and Durant, 2011), with it generally being believed that aggregation decreases the lifetime of fine ash in the atmosphere (Durant, 2015). Recently, however, there has been some debate about whether aggregation always decreases residence time. A rafting effect, where the core particle in a cored cluster travels further as a result of being part of an aggregate, has been proposed based upon modelling of PC(3) type aggregates (Rossi et al., 2021).

Incorporating aggregation into ash dispersion models is a challenging process, due to aggregate formation being dependent on how the plume and meteorological conditions develop

over time, with more simplistic approaches only considering what percentages of the deposited ash size distributions can be considered as having undergone aggregation (Folch, 2012). Earlier schemes looked at accounting for aggregation when modelling ash deposition by simply assuming that a certain proportion of individual ash particles of a known size range had been incorporated into aggregates (Cornell et al., 1983).

The NAME model, used by the London Volcanic Ash Advisory Centre, currently does not consider aggregation when carrying out ash dispersion models in operational mode; it instead treats the particle diameter as constant throughout the simulation (Devenish et al., 2012). Recently however, the first aggregation scheme which looks at how the grain size changes as a result of aggregation occurring within the ash cloud was developed by Beckett et al. (2022). They found that when they integrated this scheme with NAME it was influenced by the density of the aggregates, with an ash cloud from Eyjafjallajökull volcano, with a high enough concentration to impact aircraft, having a 2% lower extent when aggregate density is considered the same as the individual particles, but up to a 1.1 times larger extent if the density of the whole aggregate is lower than the particles by which it is made up.

Overall, aggregation is an important but poorly understood process in volcanic ash clouds, which has the potential to considerably influence the trajectory of individual ash particles, before and during sedimentation.

This chapter presents new small-scale aggregates, collected within eight minutes of an eruption at Volcán de Fuego in Guatemala. They were captured via a SEM stub which was flown onboard an UAV, close to the summit of the volcano. This capturing on the stub enabled the individual aggregates to be further analysed to look at overall shape and size, as well as individual particle size. Understanding the formation of these quickly generated aggregates can give a further understanding of process occurring in ash clouds during the earliest part of the ash particles lifetime in the atmosphere.

5.2 Data Collection

The aggregate bearing stubs were collected on the 13th of January 2022 during a field campaign to Guatemala. They were captured above Volcan de Fuego when there was an abundance of meteorological cloud present near the summit, as can be seen in Figure 5.2 (b). This image also shows (in the red circle) ash from an eruption mixing with the cloud present at the summit,

almost immediately after being ejected from the volcano. The UAV used to collected the particles was a fixed-wing Skywalker X8, as described in Chapter 4. Figure 5.2 (a) shows the flight path taken by the UAV, starting at the Fuego Volcano Observatory and gradually reaching a height greater than the height of Fuego's summit (3,800m asml). Two SEM stubs were exposed to the airflow, in the proximal volcanic cloud, with the location this happened at being marked on the flight path. Both stubs were released for a total of 35.5 seconds and travelled 623 metres, with the drone moving at an average speed of 18.76 m/s. Where the eruption began in also marked on the flight-path and the stubs were exposed 7 minutes and 23 seconds after this explosion. After the 35.5 seconds the stubs were returned to their housing in the fuselage where they were protected from coming into contact with any further particles. Once on the ground again the stubs were removed from the UAV and placed into a sealed chamber, which was used for transport to Bristol.

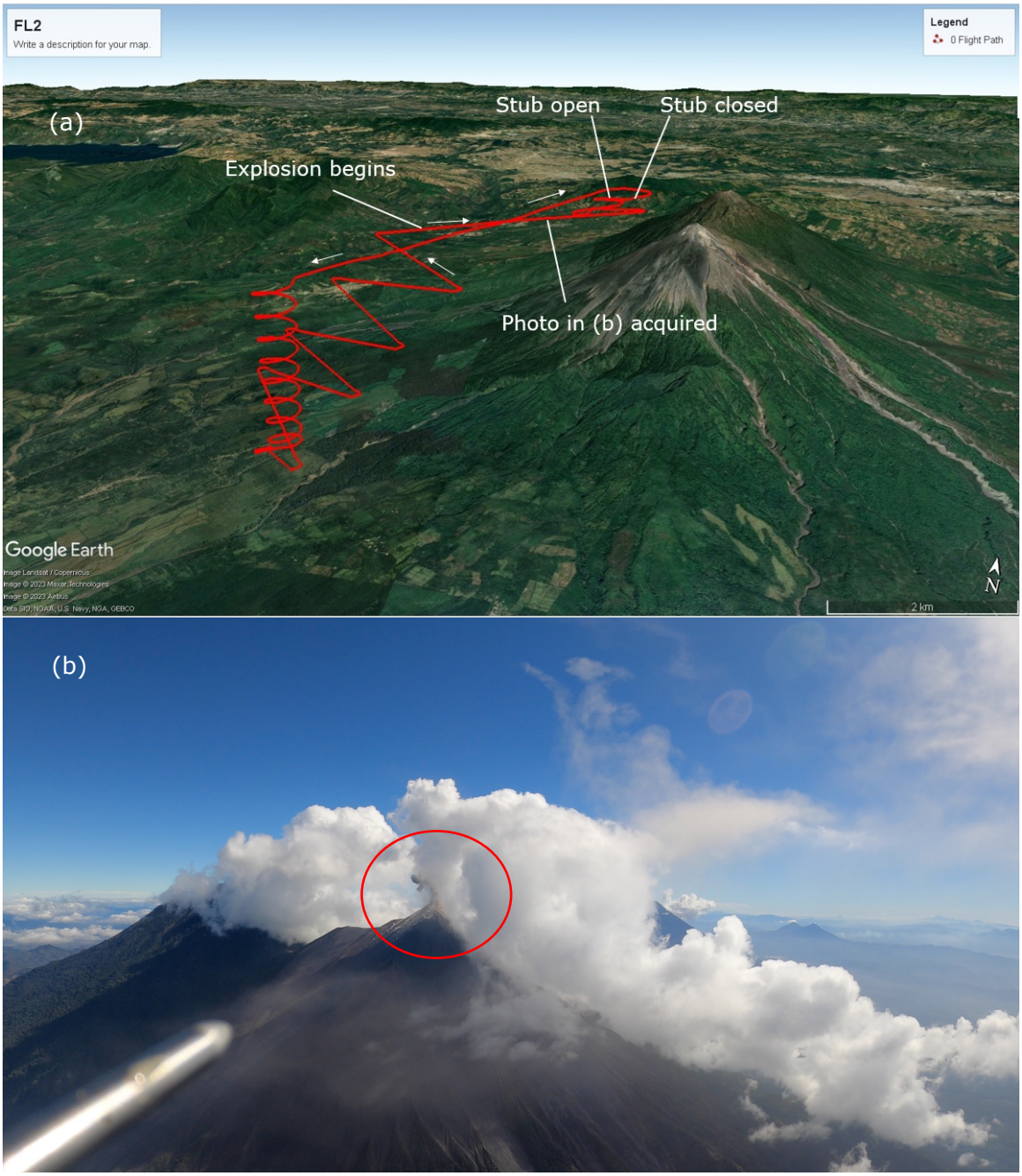

Figure 5.2: *(a) Flight path (red line) taken by the UAV on the 13th of January 2022, highlighting where the stubs were exposed. The point where the explosion begins is also highlighted as well as where the photo in (b) was taken. (b) In flight image showing the presence of meteorological cloud surrounding Fuego's summit on the day, inside the red circle it is possible to see an ash cloud begin to mix with the atmosphere.*

5.3 Methods

5.3.1 SEM Images

When the stubs collected in flight were visually inspected, two appeared to contain signficant differences when compared to over thirty previous flights (Macleod et al., 2022). On return to Bristol these two stubs (Flight 2) were imaged in full, using a Hitachi S-3500N SEM at 35x magnification (Figure 5.3), and this revealed aggregates ranging in size from approximately 500-1100μm. It can be seen that these stubs look very different from those imaged in Figure 4.9. The SEM was then used again to image individual aggregates which displayed good preservation and minimal contamination, with those being selected highlighted in Figure 5.5. There was a disruptor present in front of Figure 5.3 (i) during collection, which can be seen visually by the shadow present running down the centre of the stub. Other areas on the two fully imaged stubs potentially show evidence for incomplete aggregation or poor preservation. This poorer preservation could occur possibly as a result of the aggregate "disintegrating" on impact with the stub.

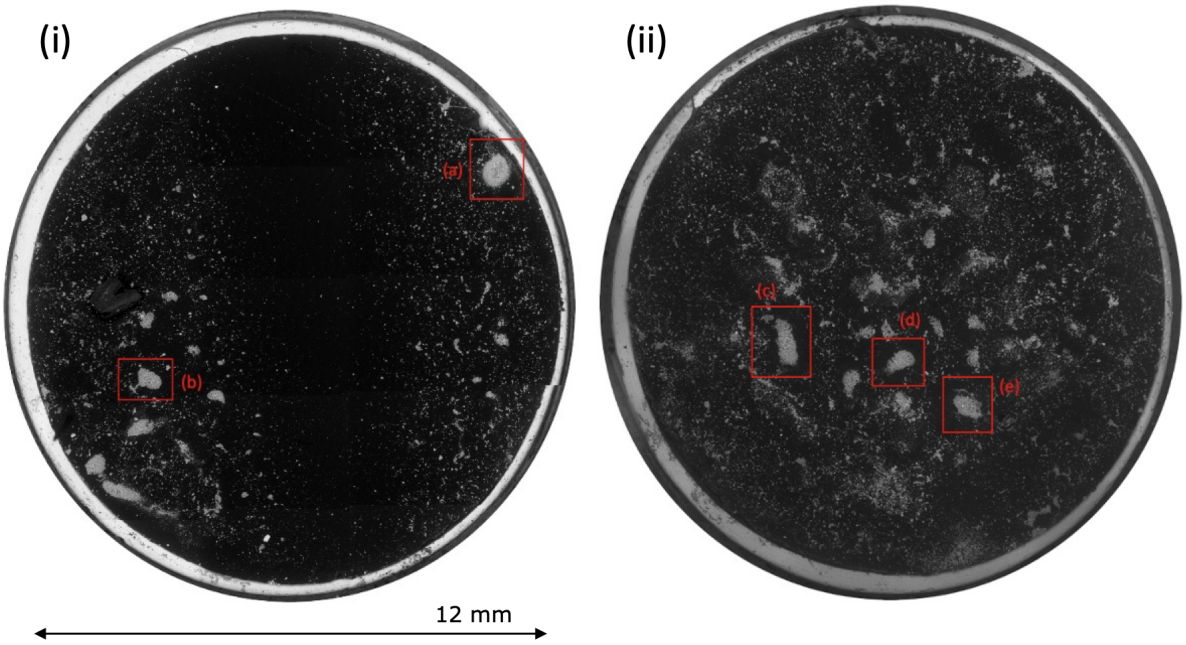

Figure 5.3: *(i) An image of the stub which had a disruptor present, creating the shadow seen through its centre. Aggregates (a) and (b) are highlighted by red boxes on this stub, with one either side of the shadow (ii) The stub with no disruptor present, with aggregates (c), (d) and (e) being highlighted by red boxes.*

5.3.2 Image Processing

The selected aggregates were then analysed in ImageJ to look at particle size and shape. This was done by first increasing the brightness of the image followed by thresholding, to create a black and white image. The centroid was then calculated by outlining and creating a mask of the whole aggregate. Depending on the diameter of the aggregate 4 or 5 boxes of 70 x 110 microns were then drawn, starting from the centroid, and continuing to the aggregates' edge. The direction in which to leave the centroid was chosen based on the longest available axis. The particles within these boxes were separated from each other by using the pencil tool in ImageJ and under visual inspection, with any particles touching the edge of a box being excluded. The macro from Liu et al. (2015) was then run within ImageJ on each box in order to calculate a number of particle properties, including the particle area which was used to look at particle size across the 4 or 5 boxes. Figure 5.4 (a) shows one aggregate with the red rectangular box highlighting the area which was selected to be subdivided into five smaller boxes; with (b) showing this area once it has been thresholded, ready to be divided into five individual boxes.

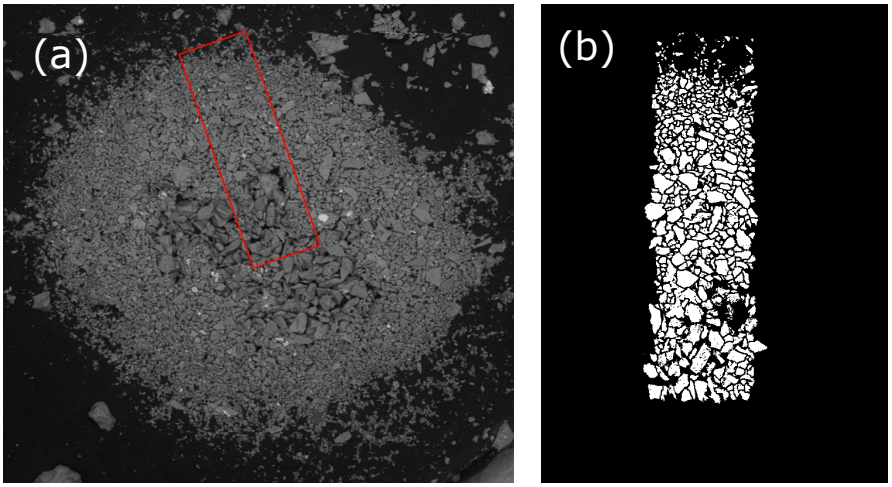

Figure 5.4: *(a) This SEM image of an aggregate shows the area (red rectangular box) which was selected for further processing. (b) This is an image of that selected area having been thresholded.*

5.4 Results

By visually examining the SEM images of the individual aggregates it can be seen that they vary in appearance and shape. Looking at Figure 5.5; aggregate (a), for example, shows a

rounded shape with a clearly defined courser centre leading to increasingly fine particles away from its centre, whereas aggregate (b) has a more sub-rounded shape and a tail of particles leaving its rim. This tail could be a result of the aggregate hitting the stub at an oblique angle, compared to a direct hit which might preserve a more rounded or complete shape. Aggregate (c) has an almost rectangular shape, but there is still a clearly defined coarser middle section. It is difficult to define which aggregate is the largest as (a), being round in shape, has the largest diameter, but (c) has the longest individual axis. The rim seen around the edge of aggregate (e) could also be evidence of the aggregate's continued growth, with it hitting the stub before another ash particle layer has had a chance to develop.

There was also evidence for proto-aggregates on these stubs, which are generally poorly sorted and do not have such a distinct shape. These could also be aggregates that had begun formation but have hit the stub before further development into the aggregates seen in Figure 5.5. However, although there is some particle clustering seen on the stubs from the flights in Chapter 4, nothing on this scale or of this nature is observed on any other stubs flown through an ash cloud at Fuego. Aggregate (e) also shows evidence of a band of unattached particles around its edge; these could be part of another layer which was in the process of forming when the aggregate hit the stub.

These 2D images also do not highlight the 3D shape of the aggregates. Aggregate (a) (Figure 5.5) is clearly prominent above the flat surface of the stub implying that before impact it would have potentially been spherical in shape and the centre of the aggregate is now being exposed. The centre could have become exposed as a result of impact, or because of air flow in-flight removing the top layer of particles. Aggregates (b) - (e) show less relief in profile, making it harder to ascertain their original 3D shape.

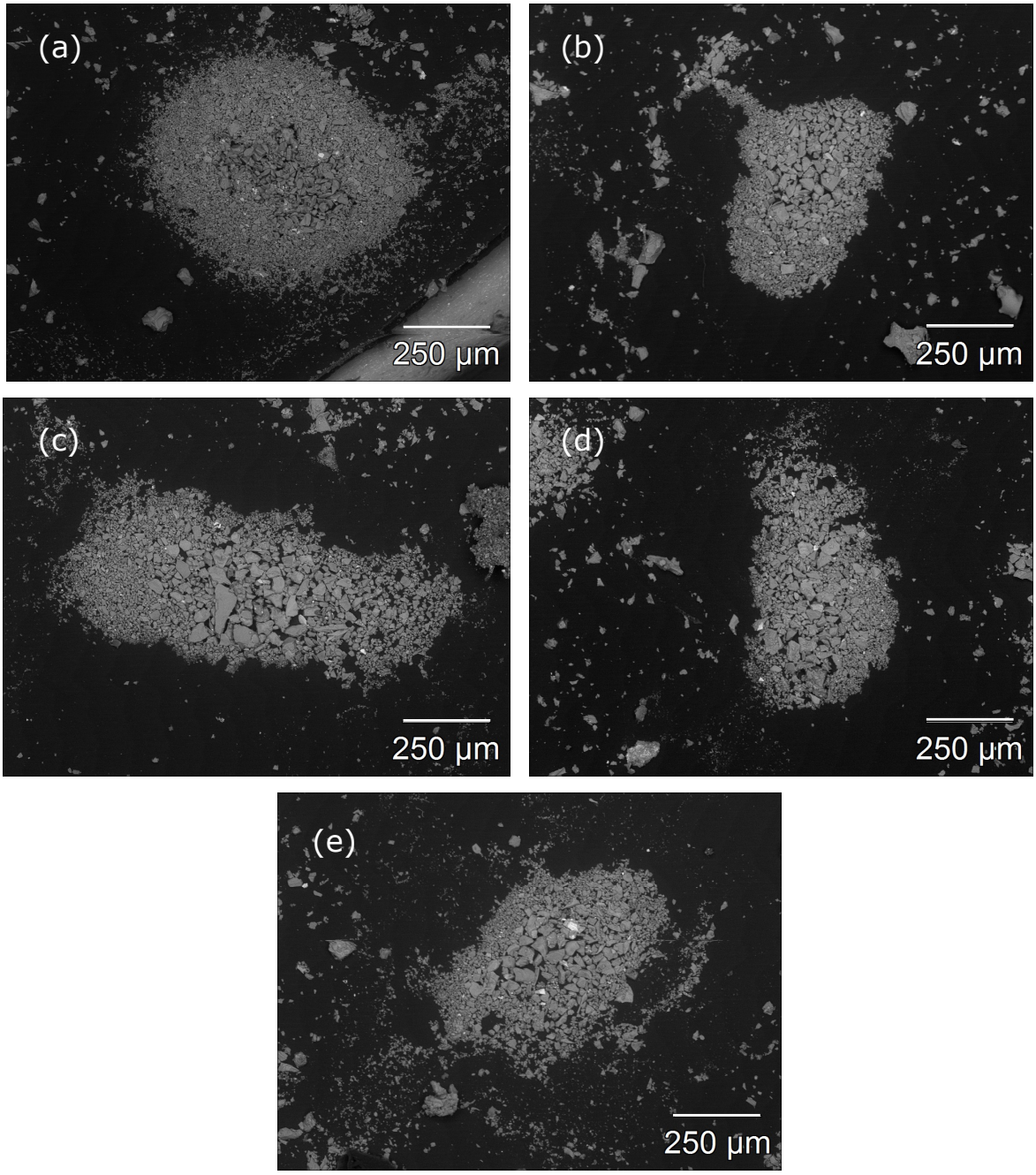

Figure 5.5: *These five ((a) - (e)) SEM images show the well-preserved aggregates on the two stubs which were selected for further analysis. There is a large variation in shape across these five examples with aggregate (a) being the most circular and aggregate (c) showing a more rectangular shape.*

5.4.1 Individual Particle Size

The area equivalent diameter was calculated for each individual ash particle, by the same methods described in chapter 3. This diameter was then plotted, using box and whiskers charts, against distance from the centre of each aggregate (Figure 5.6). The distance was taken from the centre of each individual sub-divided box. The maximum individual ash particle size across all the aggregates is 43.3 μm, with the minimum being 1.7 μm. There is variation in the data for each aggregate, but generally particle size decreases with distance from the centre. Aggregate (a) is the best example of this as the mean particle size consistently decreases across the 5 boxes and there is a low spread of data within the interquartile ranges at each distance. The other aggregates show a larger spread in the data, with (b), (d) and (e), all showing an increase in mean particle size between 40 and 120 μm from the centre, before decreasing to the rim. Outliers are present for all aggregates, indicating that there are particles outside the general data trends and indicating potential variation. This increase observed in aggregates (b), (d) and (e) could be showing evidence for a double centre or perhaps the formation of an imperfect aggregate which would struggle to grow larger.

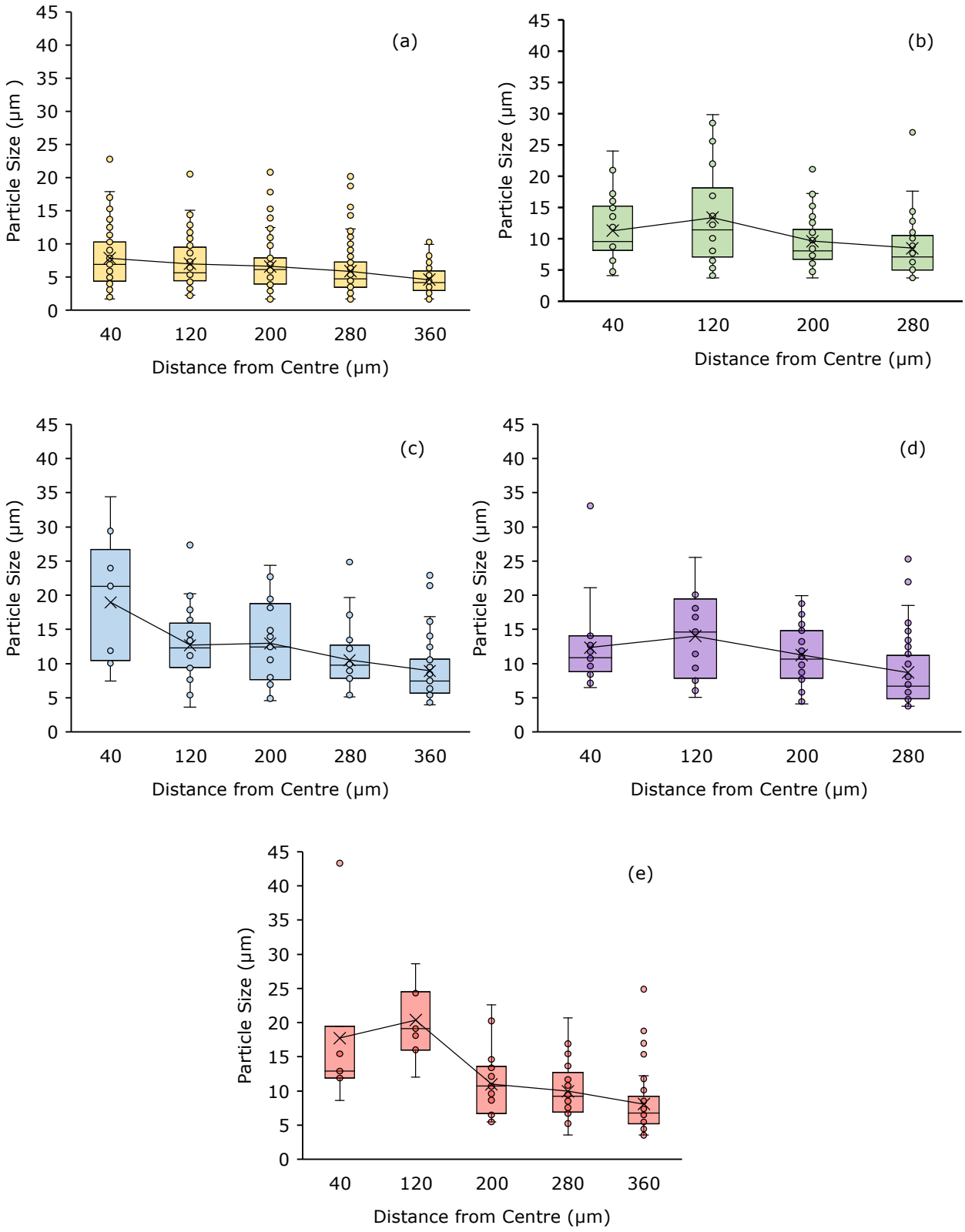

Figure 5.6: *These box and whiskers charts use the area equivalent diameter to show changes in each aggregate's ((a) - (e)) individual particle size from centre to rim.*

Particle size distributions were also plotted for all the individual very fine particles across the section of the aggregate analysed (Figure 5.7). As in chapter 3, these diameter values were then plotted in 1 μm bins, from 0-10 μm. These showed that there were no particles < 1 μm in size present in any of the aggregates, with only aggregate (a) containing particles within the 1-3 μm range. Aggregate (a) is also unique in that 88% of particles present are < 10 μm in size, compared to only ∼50% for the other four aggregates. There are no obvious trends though across the five aggregates, with each particle number percentage distribution taking a different shape. Form factor was also looked at but was not shown to contain any particular trends, just large variation across all aggregates for all distances from the centre.

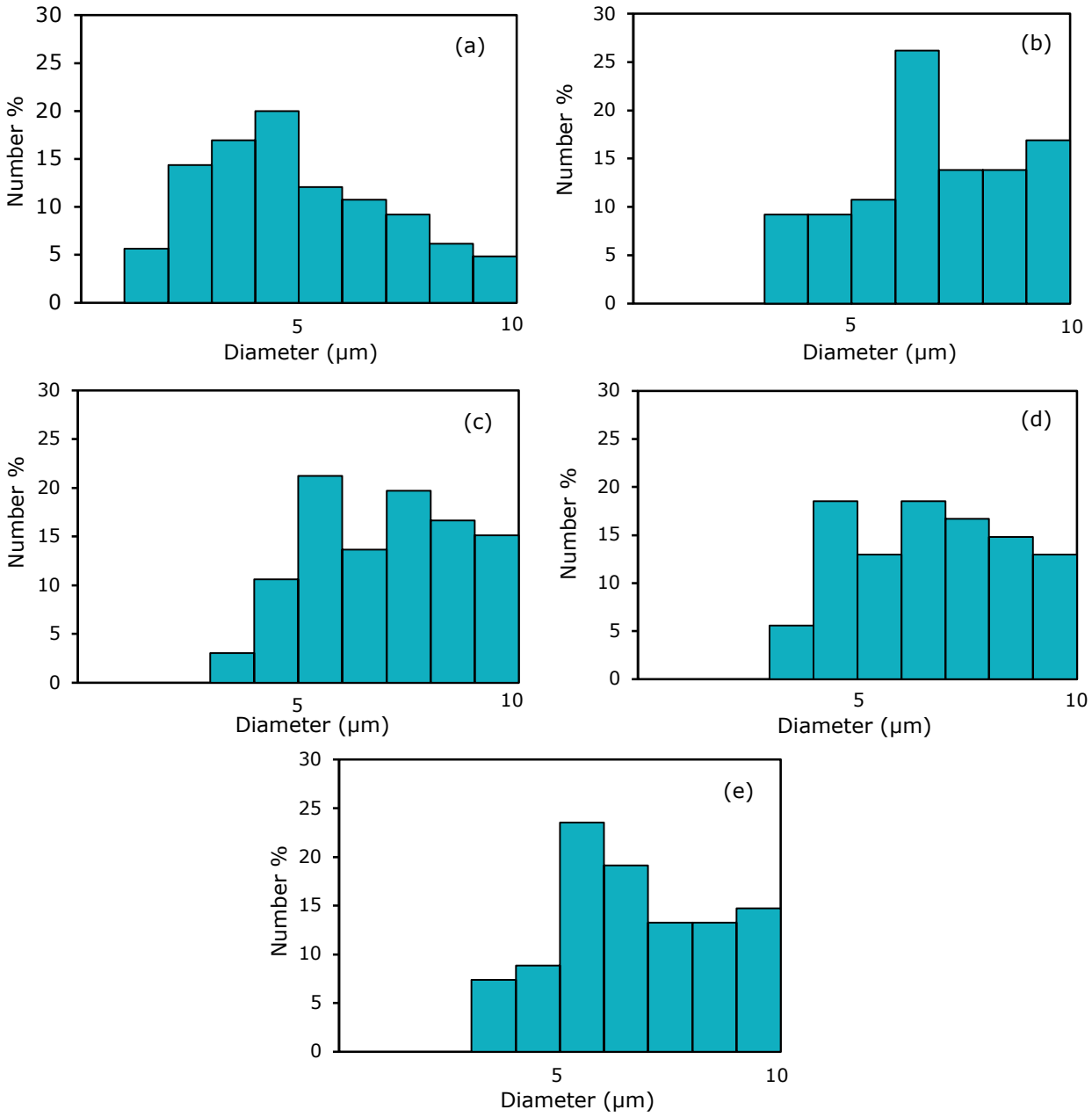

Figure 5.7: *The number percentage distributions for aggregates (a-e)*

5.5 Discussion

The aggregates presented constitute a unique set of observations of what is occurring within the first eight minutes of an ash cloud's lifetime. Whilst they are consistent with previous examples of volcanic ash aggregates collected from fallout and deposits, aggregates have never before been collected this close to the vent or this soon after an eruption. The aggregates appear mostly closely related to AP(2) type (Brown et al., 2012), given their concentric form

and sorting.

Aggregates were collected after the eruption of Eyjafjallajökull in 2010, with one example showing a similarity to the samples collected at Fuego, with a coarser centre and a finer rim (Bonadonna et al., 2011). However the Eyjafjallajökull examples are all smaller than those present in this chapter and were sampled at a much greater distance from the vent (9.6-56 km) (Bonadonna et al., 2011). Bagheri et al. (2016) sampled aggregates 3.7 km away from at Sakurajima volcano via fallout collection on adhesive tape; however, through numerical inversions they say these aggregates potentially formed within seconds of the ash cloud entering the atmosphere. Although the aggregates sampled by Bagheri et al. (2016) also formed quickly after an eruption, they are different in shape and composition to those examined in this chapter; their shape is less well defined and they are referred to as cored clusters as they lack the distinct particle size grading observed in the aggregates from Fuego (Figure 5.6). Timing of the aggregates presented in this chapter can be uniquely constrained due to the UAV being in the air when an eruption occurred; there is no other example where aggregates have been captured directly in an ash cloud using this these techniques. Further sampling of ash around Fuego may help to constrain whether these aggregates are growing larger and being deposited, or whether they are not preserved.

Water is implicated in the formation of these aggregates due to meteorological cloud being present on the day of their collection, an unusual event during the early part of the day in the dry season, and over thirty previous flights carried out on clear days at Volcán de Fuego having never collected in-situ aggregates (Macleod et al., 2022). On previous flights this meteorological cloud is usually avoided or flights suspended when it forms, but on this particular day an exception was made, which led to the collection of aggregates. The relative humidity on collection was likely above 100% due to cloud being present (Twohy et al., 2009); the ash particles could also act as condensation particles, encouraging further cloud formation. At relative humidity above 71% ash particles are always thought to undergo wet aggregation; below this threshold, electrostatic forces dominate (Telling et al., 2013). Visual inspection of the stubs also shows evidence for liquid having being present. Around some aggregates there are water marks present, suggesting that evaporation has potentially occurred after collision. The aggregates have most likely formed by the wetting of original larger individual ash particles which have then stuck together to form a core. These larger particles in turn attracted progressively smaller particles, to form the outer shell. The average size of orographic water droplets

($\sim$ 5-15 μm (Simmel et al., 2005)) will be on order the same size as the individual ash particle and therefore much smaller than the overall aggregates, which supports this hypothesis as it would not be possible for the entire aggregate to be suspended in one water droplet. The water may be forming on the surface of the ash particles as droplets which then spread to create a film Mueller et al. (2017), but again it is most likely not possible for many ash particles to be suspended in one large water droplet. This process of wetting is occurring very quickly though, as the aggregates were captured within 8 minutes of an eruption.

Van Eaton et al. (2012) and Mueller et al. (2016) propose aggregate formation in this way, through a theoretical approach and laboratory experiments respectively. Figure 5.8 shows a potential method of formation, based upon previous work, where suspended individual ash particles become coated with liquid water, and then begin to agglomerate together. This agglomeration is dependent on particle size, where initially larger particles preferentially sticking together; once the aggregate reaches a diameter of approx. 300 μm, creating the core, (as seen in Figure 5.6) this critical size then begins to preferentially allow the adherence of particles which are increasingly smaller in size, expelling larger particles on collision, following the mechanism postulated by Mueller et al. (2016). The reduction in the size fraction of all aggregates (a-e) in Figure 5.7 supports this hypothesis. This can be further explained by the fact that larger particles, having a greater kinetic energy, will struggle to stick to the core once it reaches the aforementioned critical size, due to the fact that the collision with the core will be too energetic for the relatively thin layer of water coating the particle.

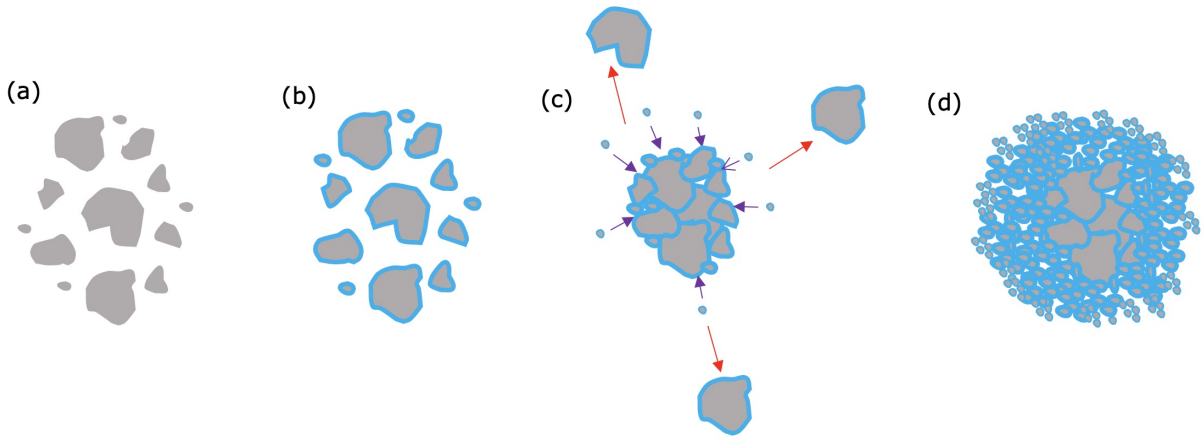

Figure 5.8: *This diagram (adapted from both Van Eaton et al. (2012) and Mueller et al. (2016) shows the proposed formation process for these observed aggregates. (a) Dry particles do not interact strongly until (b) wetting (a thin film of water coats the particles) where firstly (c) coarse, less well sorted code and then (d) a shell of finer particles is formed*

Perhaps the abundance of small particles present in aggregate (a) indicated that it began formation closer to the volcanic vent, or had been present in the atmosphere longer before collection, allowing increasingly fine particles to adhere to its outer rim. Interesting, in the same aggregate there is evidence of a double core, suggesting that coalescence of cores, as proposed by (Van Eaton et al., 2012) has also been observed.

Aggregation could be hindered by evaporation of water off the ash particles or incomplete coating of water; due to the particles still being at a high temperature after the recent eruption (Lathem et al., 2011). This could be why some proto-aggregates are seen, with their growth being stopped by the water film evaporating from the individual particles.

The aggregation of smaller particles to form a larger structure has the potential to significantly influence ash dispersion models, as these smaller particles would have travelled much further, falling out of suspension at a later point. They also effect the overall density of the ash cloud, likely precipitating more rapid fallout. Given that the individual particles in the aggregates are small ≤ 20 μm and in the form of AP(2) they are are unlikely to be rafted. This typically requires particles in a PC(3)-type configuration (Rossi et al., 2021).

These examples also highlight the potential variation in aggregate shape which, like the individual ash particles they are composed of, could impact the distances they are likely to travel. This also shows that weather is likely impacting the possibility of aggregate formation, with some aggregation probably always taking place, but perhaps there is greater number

of small particles forming aggregates when ash is erupted into meteorological cloud near a volcano's summit.

5.6 Conclusions

UAV flights over Volcán de Fuego in January 2022 collected in-situ aggregates less than four minutes after an eruption. Aggregates on this scale, collected this quickly and in-situ, have never been seen before, showing that important processes are occurring close to the summit of the volcano. The aggregates show a general trend of decreasing particle size from core to rim; with evidence for double centres and therefore coalescence in at least some of the accretions. Aggregates not only fine, but also increase in sorting as a function of distance from the centriod with a distinct change observed at a diameter of $\sim$ 300 μm (Figure 5.6). This change could also be indicative of their formation, which is hypothesised to be a result of the ash particles interacting with water, with the aggregate core preferentially allowing increasingly small particles to adhere, creating the observed fine rim.

Aggregation is currently not considered in operational forms of ash dispersion models, despite having been shown to improve forecasts (Beckett et al., 2015), with schemes with the ability to be incorporated into operational models only recently having been developed (Beckett et al., 2022). These aggregates have also highlighted the importance of considering meteorological conditions when incorporating aggregation into dispersion models. These small-scale aggregates are almost certainly not forming, and have never been observed, on days when the summit of the volcano is clear of cloud.

Overall, these aggregates demonstrate the importance of continuing research into how these structures form due to their importance in improving ash dispersion models. They also offer important new insights into rapid aggregate formation close to the summit's of active volcanoes.

Chapter 6

Summary, Conclusions and Future Work

6.1 Thesis Summary

By analysing the literature, chapter 2 highlights the problems around how to detect and quantify volcanic ash in relation to hazards to aviation. There have been numerous encounters of aircraft with volcanic ash, but there is still no in-situ information about the particulate matter aircraft are flying through to pilots. The limitations of dispersion models are also discussed, with many factors influencing the potential lifetime of volcanic ash in the atmosphere, post an ash-rich eruption from a volcano.

In Chapter 3 the ability to create an ash cloud box in the laboratory was demonstrated, with it being capable of testing various sensors. AB2 has been characterised, and an ash circulation model proposed to help understand the patterns observed. However, there are challenges involved with the methods developed including contamination of the stubs post exposure. Nevertheless, a test environment that mimics at least some environmental conditions, has demonstrated its importance when planning and executing UAV flights into ash clouds in the field, particularly around sensor testing and calibration.

Chapter 4 shows the use of these sensors at an active volcano, where in-situ particle concentrations and particle samples were collected using UAVs, using the sensors tested in chapter 3. Several scientific questions were addressed including (1) how the particle size distribution changes as a function of time by looking at the comparing distal and proximal ash clouds, (2) how an aerodynamic disruptor affects collection of ash and a comparison of real-time

(OPC-based) and time averaged (collection-based) methodologies.

Finally, Chapter 5 examines newly found in-situ aggregates, collected close to the summit of Volcán de Fuego, during a flight where meterological and volcanic ash clouds interacted directly. The aggregates are thought to form as a result of cloud droplet interaction with the individual ash particles as they have never been see on any of more than thirty flights in clean, dry air. A mechanism of formation is proposed after discussion of particle size and sorting as a function of distance from the centroid of the aggregate. These aggregates highlight the importance of continuing to collect in-situ data at active volcanoes and their incorporation into dispersion models.

Overall these three chapters show how both laboratory and field techniques can be combined to further our understanding of volcanic ash clouds.

6.2 Conclusions

The following main conclusions can be drawn from the the work within this thesis:

- Characterising AB2 showed that with increasing wind tunnel duration there is increasing particle percentage coverage (Figure 3.11). Fine ash is also expelled first when the wind tunnel is initially switched on which was shown by the particle number percentages from the stubs in Figure 3.12. The PMS5003 readings help to constrain the movement of ash within the box, leading to an ash circulation diagram (Figure 3.20), which proposes that after ash leaves the wind tunnel it interacts with the sides of AB2 before hitting the back wall and recirculating to a distance of approximately 60 cm.

- In-situ ash particles were collected at Volcan de Fuego in both proximal and distal ash clouds via SEM stubs, with the proximal clouds showing a much higher concentration of ash. PMS5003 readings were capable of distinguishing between the proximal and distal ash clouds as well as the atmospheric boundary layer (Figure 4.19 and Figure 4.20). A disruptor, believed to enhance fine particle (<1 μm) collection, in front of the SEM stubs was also found to produce mixed results when used during the UAV flights. More flights to collect in-situ ash particles are needed to fully test the disruptor's capabilities.

- Volcanic ash aggregates formed within 8 minutes of an eruption at Volcan de Fuego (Figure 5.5). Due to meteorological cloud being present above the volcano on the day of

collection they are believed to have formed as a result of the particles becoming coated in a thin film of water. This water film resulted in initially larger ash particles agglomerating together followed by preferential collection of increasingly fine particles (Figure 5.8).

6.3 Future Work

The closure of airspace across Europe as a result of the Eyjafjallajokull eruption in 2010 have led to advances in our understanding of the interaction of volcanic ash and with civil and military aviation. Specifically, it drove the need to understand how volcanic ash damaged jet engines and, critically, prompted the need to understand the make-up of volcanic clouds more completely. This, in turn, drove a requirement for understanding the dose, rather than the concentration of ash in the atmosphere. This then precipitated the need for on-wing sensors that could measure concentration as a function of time.

However, and as with previous encounters with volcanic ash, it is very easy to become complacent when there is no immediate threat, therefore work must continue to be carried out in order to protect those on board planes as well as preventing economic catastrophe. Understanding ash clouds is a complex time-dependent problem with many factors influencing particle transportation and deposition.

Lining the AB2 with waterproof paint and introducing a humidifier could be used to try generate small scale aggregates in the laboratory. Further experiments could also be run with both the SEM stubs and PMS5003 in AB2 to continuing constraining how ash is moving within its interior. Comparison between multiple 1 mm areas on each SEM stub would also be useful to validate that this area is representative of the particle distribution across the stub as a whole.

Due to the lack of visibility of particularly fine grained (<4 μm) volcanic ash for pilots when in the cockpit, careful consideration should be given to real-time detection and pilot warning. Fitting all aircraft with sensors would be an invaluable way of understanding more about the transportation of ash (along with other particulates), and increasing in-flight safety as pilots would instantly be aware they had flown through a potentially damaging dose, allowing them to take action accordingly. This would also be beneficial to the airline industry as it would provide continuous monitoring of air entering the engine, helping when monitoring engine health.

One challenge with on wing-sensors is the possibility they might detect particles other than just ash. This work is potentially relevant and these techniques could also be used when looking at desert dust which is a hazard effecting both commercial and military aircraft on a regular basis. This would be beneficial to our understanding of the atmosphere, and climate more broadly, and may help aircraft avoid other dangerous environments.

The next challenge would also be to sample larger eruptions than those observed at Fuego. However, sampling Plinian ash clouds close to the source is challenging due to dangerous and turbulent conditions and longer eruption repose times. If it was possible to sample these large ash clouds in-situ close to the source using UAVs as well as at greater distances (kilometers away) this would provide invaluable information about ongoing processes within the ash cloud. PM readings and samples could also be compared with samples collected on the ground in similar locations to where UAVs were flown. This type of sampling also requires good temporal constraints as fully equipped UAVs need to be ready to quickly sample a plume when a large Plinian eruption occurs.

6.4 Final Remarks

The fortuitous collection of the small-scale in-situ aggregates highlights the importance of using UAVs at volcanoes and testing them in new environments. The high concentrations seen by the PMS5003 also highlight how little ash is required in the atmosphere to stall a jet engine.

The methods described in Chapters 3 and 4 could also be used to develop a pathway for sensor testing prior to exposure to an active volcano when used in the field. This could involve robust testing in AB2, to ensure smooth deployment when in potentially remote and time sensitive locations.

Overall, this thesis aims to provide new insights into methods for characterising volcanic ash in relation to aircraft hazard. It does this through both laboratory techniques and the collection of in-situ data via UAVs at an active volcano.

Appendix A

This PhD was completed as part of the EPSEC Centre for Doctoral Training in Aerosol Science. As part of this training scheme, the first nine months of the program was spent completing modules covering various aerosol science topics. This was followed by a three month sabbatical (June-August 2020) at The University of Manchester, where a research project titled "Factors affecting Particle Number and Mass Concentrations at the Manchester FIRS Site from November 2019 – February 2020" was completed, under the supervision of Dr Paul Williams. This project was written up as a report and is included in its entirety below.

Factors affecting Particle Number and Mass Concentrations at the Manchester FIRS Site from November 2019 – February 2020

Abstract

Particle number and mass concentrations at the FIRS site from November 2019 to February 2020 are analysed in this report. Local and regional effects are considered, with both wind speeds measured on site and air mass origins being examined, to better understand potential larger scale influences on concentrations observed at the site. Air masses were classified into four categories: Polar, Tropical, Arctic and Continental. These classifications were then examined according to averaged CPC, SMPS, PM1 and PM10 concentrations. Arctic air was shown to have the largest CPC number concentration of 13210 particles/cm^3, whereas tropical had the lowest with 9106 particles/cm^3. Large differences between the CPC and SMPS data also indicate that there is a high proportion of particles less than 15 nm present at the site, which could indicate that new particle formation is occurring. Local wind speeds show a spike in number concentration to the South-West across all four months, apart from November. Mass concentrations, however, showed a different pattern with a spike in the PM1 data to the South-East and more widespread concentrations of PM10 particles. It seems to be a combination of

factors affecting concentrations at the site, with evidence for large scale air masses having an impact as well as local wind speeds.

Introduction

Aerosol number and mass concentrations can vary at a site due to both regional and local effects (Beddows et al., 2014). They can also be an indicator of pollution levels at urban sites (Mönkkönen et al., 2004). Particle concentrations are also important to measure as they can have an adverse effect on human health (Rodríguez et al., 2008; Atkinson et al., 2010; Strak et al., 2010), resulting in consequences such as increasing cases of cancer, asthma and cardiovascular diseases (Anderson et al., 2012; Sánchez-Soberón et al., 2015; Khaniabadi et al., 2016).

The data used in the study was collected at the FIRS site, located to the South-East of Manchester, approximately 4 km from the city centre (Figure 6.1). This area, although being more suburban, is still surrounded by many busy main roads and is only 10 km from Manchester Airport.

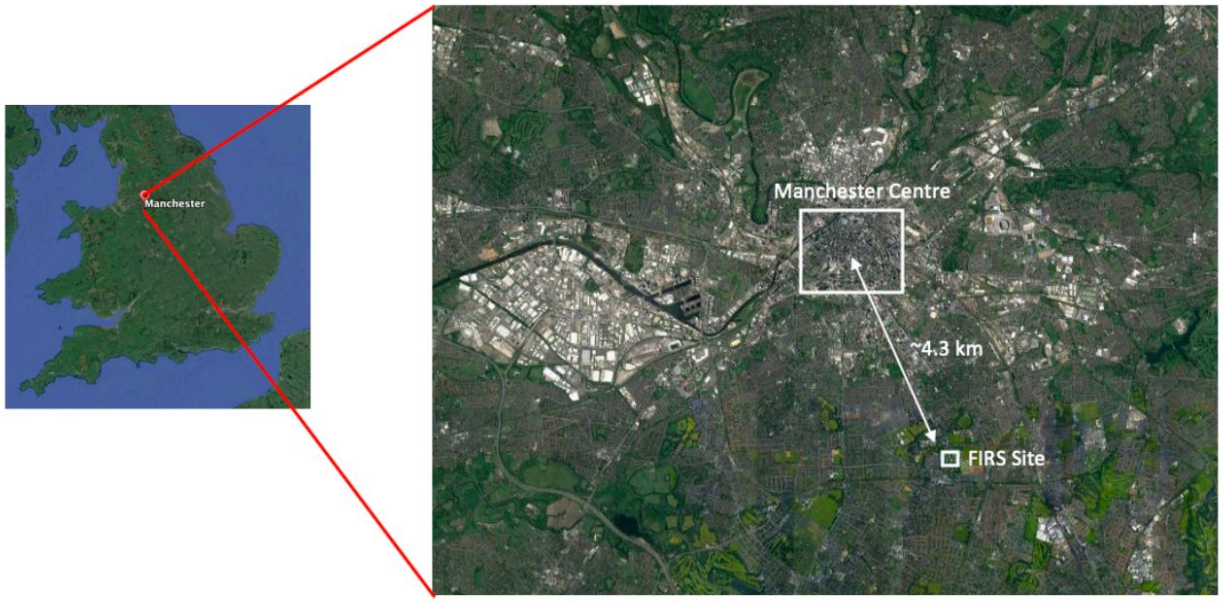

Figure 6.1: *Maps taken from Google Earth showing the location of the FIRS site relative to Manchester City Centre, and the rest of the UK. It is situated approximately 4.3 km from the city centre in a South-East direction.*

Particulate matter (PM) concentrations are used to understand the mass of aerosol

affecting a particular site and are often used to indicate air quality in urban areas (Cohen et al., 2005; Petkova at al., 2013). PM1 is defined as a particle with an aerodynamic diameter smaller than 1 µm and PM10 smaller than 10 µm (Talbi et al., 2018). Due to these particles having a range of compositions they can have an adverse effect on human health along with acting as cloud condensation nuclei (CCN) (Spracklen et al., 2008).

Traffic can also create primary aerosols in the form of ultrafine particles (particles ¡100 nm) which although may not account for a large amount of particulate mass, are important as they have the potential to reach deep within the lungs (Gao et al., 2009; Allan et al., 2010) and potentially enter the bloodstream. They can also grow to become CCN (Pierce and Adams, 2007), eventually effecting the climate as they can alter radiation being absorbed and reflected (Williamson et al., 2019). This means it is important to examine both number and mass concentrations when looking at the air quality of a region (Penttinen et al., 2001), as the ultrafine particles may only be observed in number concentrations (Aalto et al., 2005), but have the potential to be a health hazard.

These concentrations at the FIRS site can be affected by vehicle emissions as well as regional and local weather patterns. Air masses, depending on their origin and where they have travelled, can bring conditions both favourable and unfavourable for new particle formation (NPF). Generally, NPF is more likely when conditions are cooler, the air has not passed over land masses and has travelled quickly to the site (Nilsson et al., 2001; Komppula et al., 2006).

The data discussed in this study has not been previously analysed and hence any observations noted, and conclusions reached concerning this site and timeframe are new.

Experimental/Modelling/Computational Details

The particle concentrations were measured using a TSI 3750 Condensation Particle Counter (CPC) and a TSI 3082 Scanning Mobility Particle Sizer (SMPS), with the SMPS consisting of a long Differential Mobility Analyser (DMA) and a 3750 CPC. Both the machines are connected to a PM2.5 inlet system and air flow is dried to ¡40% relative humidity before sampling. The CPC counts particles in the size range of 7 nm to 2-3 µm and the SMPS measures a smaller range of 15.1nm to 661.2 nm. The PM data measurements were made with a Pala FIDAS 200E aerosol spectrometer.

Data processing was carried out mainly using Microsoft excel and the openair package in R, but Aerosol Instrument Manager (AIM) software was also used to export the raw SMPS

files. In openair the polarPlot function was used to plot the graphs seen in Figures 5 and 7, with other functions such as timeVariation being used to generate diurnal plots along with averaging functions in order to analyse the data over days. For the plots which encompass day and night, openair uses the known sunrise and sunset times for the city selected.

Following the study carried out by Bousiotis et al., 2019, the air masses were classified into four categories: Polar, Tropical, Arctic and Continental. Figure 6.2 shows a diagram adapted from Bousiotis et al., 2019, illustrating the origin of the Polar, Arctic, Continental and Tropical air masses. Polar air has come from the northern Atlantic, Tropical from the centre of the Atlantic, Continental from the East of the U.K. and Arctic from the northern latitudes above the U.K. In general, air masses which have passed over land, before reaching the Manchester site, have a lower chance of NPF events occurring, as the air is less clean (Kristensson et al., 2008; Bousiotis et al., 2019).

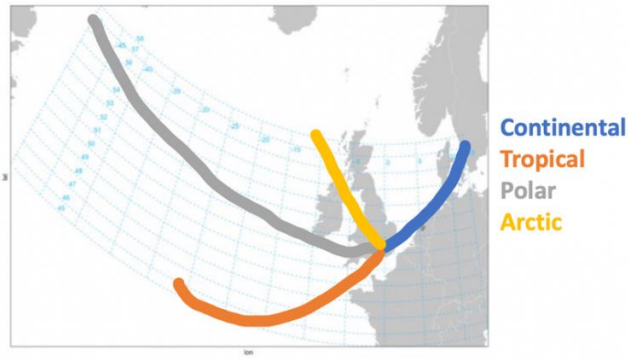

Figure 6.2: *Diagram adapted from Bousiotis et al., 2019 showing the origin of each air mass. Once the back trajectories were generated in HYSPLIT, they were compared to this diagram to determine which classification they should receive.*

This was done by first using HYSPLIT online to carry out back trajectory analysis with the majority of trajectories generated stretching back three days. On days when the trajectory origin was not clear, the HYSPLIT back trajectories were increased to five days in order to see more clearly where the air mass originated. Figure 6.3, created in Excel, shows the proportion of each air mass over the four months, showing Polar to be dominant with Continental, Tropical and Arctic sharing similar proportions. Air masses which have passed over the Atlantic have been shown to be dominant in previous studies (Birmili et al., 2001; Bousiotis et al., 2019).

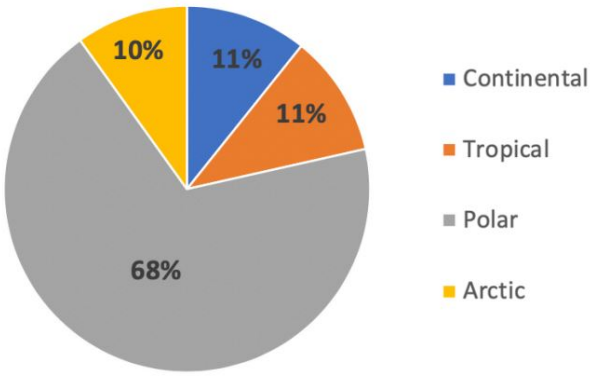

Figure 6.3: *This pie chart shows the proportion of each air mass across the four months. It can be seen that Polar occurs the most frequently, while Continental, Tropical and Arctic occur less but share very similar proportions.*

Results and Discussion

To begin to build up a picture of what was affecting number and mass concentrations at the FIRS site, values were averaged for the CPC, SMPS, PM1 and PM10 concentrations along with wind speed across the four different air mass types (Figure 6.4). This allows comparisons to be made between the air masses and see on the more regional scale what is affecting particle and mass concentrations. It can be seen that the Tropical air mass brings the lowest number of particles according to both the CPC (9106 (#/cm^3)) and SMPS (1934 (#/cm^3)). However, it brings a higher PM1 mass concentration (10.08 (μg/m^3)) than any of the other air masses and the second highest PM10 concentration (14.28 (μg/m^3)). Figure 3 shows the proportions of each air mass across the four months being examined, with Polar clearly being the dominating source. The data shows that on average, CPC concentrations are always significantly higher than SMPS, which could be an indicator of NPF as the CPC is detecting greater numbers of smaller particles. As expected, PM10 is also continuously higher than PM1 with a lower ration between the two when compared to SMPS/CPC, indicating there is a difference between the two but it less pronounced than the number concentrations.

Air Mass	CPC (#/cm³)	CPC STDV	SMPS (#/cm³)	SMPS STDV	SMPS/CPC	PM1 (µg/m³)	PM1 STDV	PM10 (µg/m³)	PM10 STDV	PM1/PM10	Wind Speed (m/s)
Continental	11344	3118.53	4672	1237.99	0.3370	8.10	3.37	12.67	4.37	0.6306	1.0
Tropical	9106	2514.52	1934	523.17	0.2409	10.08	5.75	14.28	5.55	0.6564	1.2
Polar	12596	4699.96	2605	1971.57	0.2016	6.15	6.23	12.13	7.09	0.4473	1.8
Arctic	13210	5703.84	3822	2116.84	0.2705	8.51	6.25	15.55	6.12	0.5157	1.4

Figure 6.4: *This table shows the air masses classified according to the averaged CPC, SMPS, PM1 and PM10 concentrations.*

When the CPC and SMPS concentrations were closer together in value the SMPS size distributions seemed to show a larger mode, indicating that the particles being generated had generally increased in size. The 22nd and 24th of January where the concentrations were closer in value also appear to coincide with Tropical air masses, which are suggested to bring warmer air and allow particles to grow to a larger size as they have travelled over land masses.

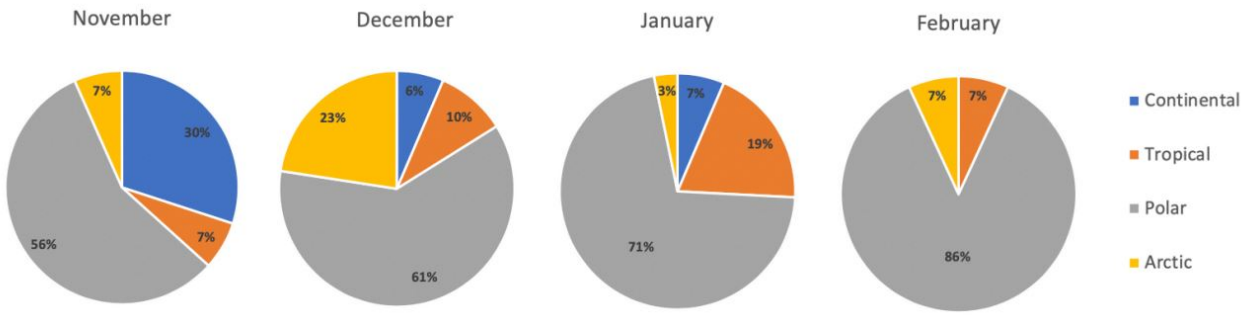

Figure 6.5: *These pie charts show the proportions of each air mass (Continental, Tropical, Polar, Arctic) occurring in each month from November to December. The most common air mass is clearly Polar, which occurs over 50% of the time for each month.*

Looking at the CPC concentrations with local windspeeds, it can be seen that they vary with wind speed and direction across the four months (Figure 6.6). All four months show high concentrations in the centre as this is where wind speed is zero and the instrument is recording. December, January and February all show higher concentrations stretching out to the South-West, whereas November lacks this trend, with more even concentrations at lower windspeeds. The concentrations also vary across the day and night, with lower concentrations being recorded during the night, usually closer to the monitoring station, potentially due to decreased traffic on the roads and lower wind speeds generally once the sun sets. One potential reason for the South-West spike in concentrations is particles from Manchester Airport which

is located 10 km away on a bearing of 205o. Another possibility is that the spike is a result of local traffic at the traffic lights located at the intersection of Wilbraham Road and Wilmslow Road.

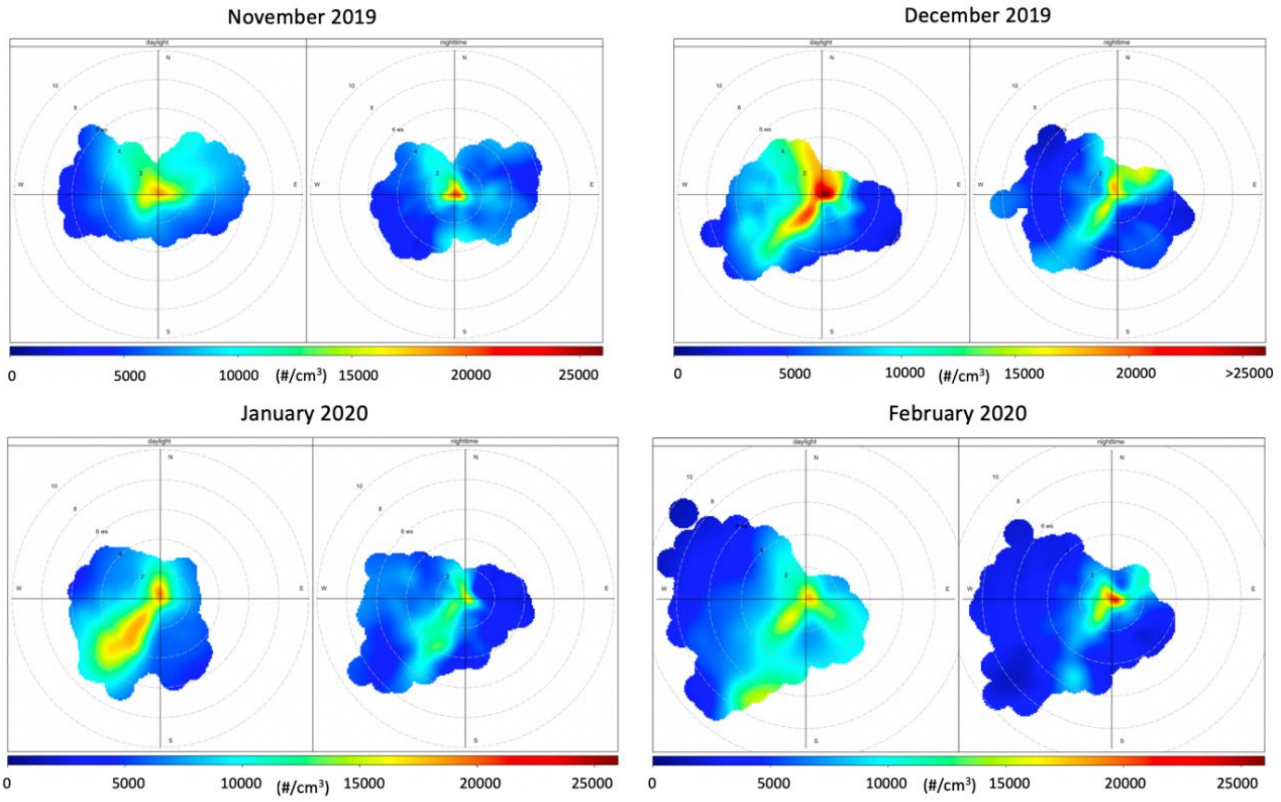

Figure 6.6: *These plots show the variations in number concentrations, measured by the CPC, along with wind speed and direction across the four months. The scale shows the wind speed increase by 2 m/s, as each circle radiates out. The left-hand plots for each CPC graph show the daytime concentrations and the right-hand the night-time.*

Examining data from November more closely shows that although the majority of air masses were still Polar, there was a much higher influence from Continental air masses when compared to the other three months. This could result in more particles coming from the East, preventing the South-West spike seen during the other months, where other air masses are more prevalent.

There is also a diurnal trend seen in the CPC data (Figure 6.7), with spikes observed during rush-hours; first around 6 am and then again at about 6 pm. The number concentrations are also generally lower during the night, just before dawn, when there would be less traffic on the road.

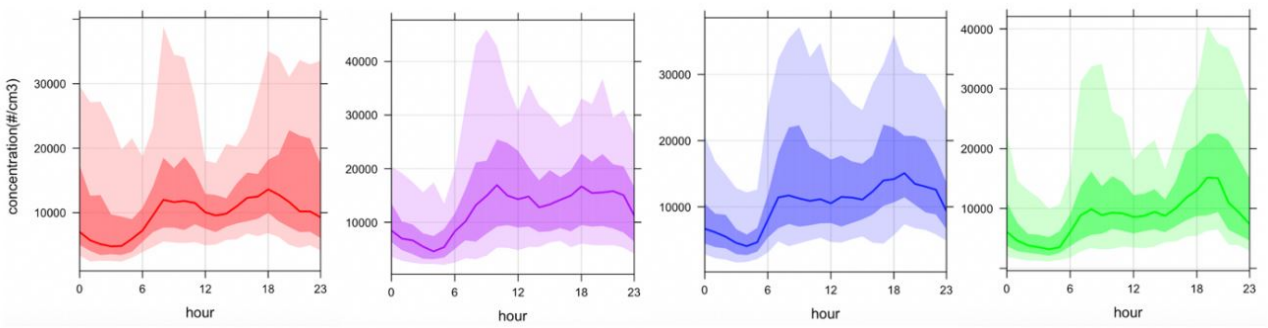

Figure 6.7: *These four graphs show the average CPC particles concentrations per hour across the four months as follows: November (red), December (purple), January (blue), February (green). Two spikes can be seen for each month – once around 6 am and another around 6 pm, along with concentrations generally being lower during the night.*

The PM1 and PM10 data was also examined more closely and showed a different pattern than the CPC concentrations when plotted with windspeed and direction. The differences between PM1, PM10 as well as day and night can be seen in Figure 6.8. In the PM1 daytime plot it can be seen that there is a strong concentration coming from the South-East; this is also noticeable in the daytime PM10 plot however as the concentration does not appear to be much stronger it can be assumed that the majority of mass responsible for this observation is coming from the PM1 particles. During the night this signal from the South-East shifts more towards the East and again does not change much between the PM1 and PM10 plots, indicating that most of the mass creating this pattern is coming from the PM1 particles. Looking at the PM10 graphs it can be seen that the concentration is spread more widely across wind direction, possibly indicating there are more variable sources for the larger particles between PM1 and PM10.

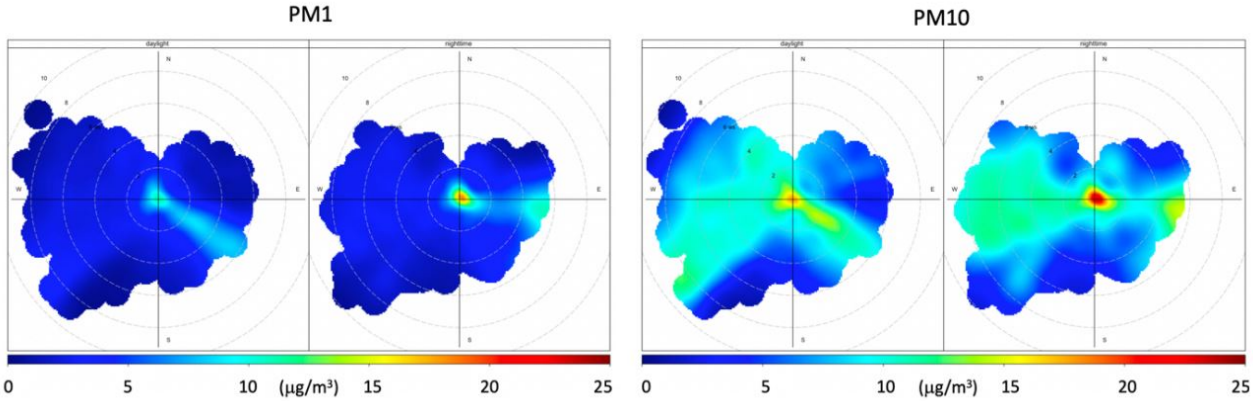

Figure 6.8: *Plots showing PM1 and PM10 combined with wind speed and wind direction, encompassing data from November 2019 – February 2020. The scale shows wind speed increasing by 2 m/s as each circle radiates out. The left-hand plots for each PM graph show the daytime concentrations and the right-hand the night-time.*

There are a few areas within the data where there is a possibility for errors and data is missing. When the wind speed is low, the wind direction can be unreliable due to the fact that at low wind speeds the wind arrow has a tendency to spin and quickly change 180°, as the wind is not strong enough to hold it in one direction. The missing data includes no recorded SMPS data for November, along with no wind speed and direction data between the 20th and 25th of November. CPC data was also missing on the 24th of February, with two more days of SMPS data also absent on the 28th and 29th of February.

The lower number of Tropical, Continental and Arctic air masses recorded also means that this data is less accurate as there is a smaller number of concentrations over which to average when classifying. There are also potentially errors associated with assigning the air mass classification due to it being done by eye, and it sometimes being difficult to decide on the origin.

Conclusions

Particle number and mass concentrations are being affected by a number of factors at the FIRS site in Manchester. Number concentrations appear to be dominated by smaller particles, potentially indicating the NPF is occurring or there is a source of small particles in the area. The main source of these particles seems to be from the South-West, which is especially Figure 6.8: Plots showing PM1 and PM10 combined with wind speed and wind direction, encompassing data from November 2019 – February 2020. The scale shows wind speed increasing by 2 m/s as

each circle radiates out. The left-hand plots for each PM graph show the daytime concentrations and the right-hand the night-time. dominant during January, noticeable during December and February but not evident during November.

By looking at the air masses according to average CPC, SMPS, PM1 and PM10 concentrations it can be seen that when there is a Tropical origin there are lower numbers of particles being counted by the CPC with Arctic air bringing the largest number concentrations.However, classifying the air masses over a longer time scale would also help to improve the accuracy of the data, as currently there were a lot fewer days with Tropical, Continental and Arctic air masses when compared to Polar. Local weather conditions also seem to be affecting CPC concentrations at the site with high readings coming from the South-West, indicating there is potentially a source of particles in this direction.

The PM1 mass concentrations, however, are coming from a South-East direction, with PM10 concentrations showing this trend but also spreading out more generally around the site. This could imply that larger particles are coming from the East, either from a different source or being transported from the continent. The Tropical air mass average records the highest PM1 mass concentrations at 10.08 $\mu g/m^3$, with the Arctic air mass average being the highest PM10 value at 15.95 $\mu g/m^3$.

Future work could also include comparisons with data from the Covid-19 period, to see if a reduction of traffic on the roads is affecting number and mass concentrations. More pollutants such as NOx and black carbon could also be examined in further studies in order to fully understand what is influences particles at the FIRS site.

Aalto, P., Hämeri, K., Paatero, P., Kulmala, M., Bellander, T., Berglind, N., Bouso, L., Castano Vinyals, G., Sunyer, J., Cattani, G. and Marconi, A., 2005. Aerosol particle number concentration measurements in five European cities using TSI-3022 condensation particle counter over a three-year period during health effects of air pollution on susceptible subpopulations. Journal of the Air & Waste Management Association, 55(8), pp.1064-1076.

Allan, J.D., Williams, P.I., Morgan, W.T., Martin, C.L., Flynn, M.J., Lee, J., Nemitz, E., Phillips, G.J., Gallagher, M.W. and Coe, H., 2010. Contributions from transport, solid fuel burning and cooking to primary organic aerosols in two UK cities. Atmos. Chem. Phys, 10(2), pp.647-668.

Anderson, J.O., Thundiyil, J.G. and Stolbach, A., 2012. Clearing the air: a review of the effects of particulate matter air pollution on human health. Journal of Medical Toxicology, 8(2), pp.166-175.

Atkinson, R.W., Fuller, G.W., Anderson, H.R., Harrison, R.M. and Armstrong, B., 2010. Urban ambient particle metrics and health: a time-series analysis. Epidemiology, pp.501-511.

Beddows, D., Dall'Osto, M., Harrison, R.M., Kulmala, M., Asmi, A., Wiedensohler, A., Laj, P.G., Fjæraa, A.M., Sellegri, K., Birmili, W. and Bukowiecki, N., 2014. Variations in tropospheric submicron particle size distributions across the European continent 2008-2009.

Birmili, W., Wiedensohler, A., Heintzenberg, J. and Lehmann, K., 2001. Atmospheric particle number size distribution in central Europe: Statistical relations to air masses and meteorology. Journal of Geophysical Research: Atmospheres, 106(D23), pp.32005-32018.

Bousiotis, D., Dall'Osto, M., Beddows, D.C., Pope, F.D. and Harrison, R.M., 2019. Analysis of new particle formation (NPF) events at nearby rural, urban background and urban roadside sites. Atmospheric Chemistry and Physics, 19(8), pp.5679-5694.

Cohen, A.J., Ross Anderson, H., Ostro, B., Pandey, K.D., Krzyzanowski, M., Künzli, N., Gutschmidt, K., Pope, A., Romieu, I., Samet, J.M. and Smith, K., 2005. The global burden of disease due to outdoor air pollution. Journal of Toxicology and Environmental Health, Part A, 68(13-14), pp.1301-1307.

Gao, J., Wang, T., Zhou, X., Wu, W. and Wang, W., 2009. Measurement of aerosol number size distributions in the Yangtze River delta in China: Formation and growth of particles under polluted conditions. Atmospheric Environment, 43(4), pp.829-836.

Khaniabadi, Y.O., Goudarzi, G., Daryanoosh, S.M., Borgini, A., Tittarelli, A. and De Marco, A., 2017. Exposure to PM 10, NO 2, and O 3 and impacts on human health. Environmental science and pollution research, 24(3), pp.2781-2789.

Komppula, M., Sihto, S., Korhonen, H., Lihavainen, H., Kerminen, V., Kulmala, M. and Viisanen, Y., 2006. New particle formation in air mass transported between two measurement sites in Northern Finland. Atmospheric Chemistry and Physics, 6(10), pp.2811-2824.

Kristensson, A., Dal Maso, M., Swietlicki, E., Hussein, T., Zhou, J., Kerminen, V.M. and Kulmala, M., 2008. Characterization of new particle formation events at a background site in Southern Sweden: relation to air mass history. Tellus B: Chemical and Physical Meteorology, 60(3), pp.330-344.

Mönkkönen, P., Uma, R., Srinivasan, D., Koponen, I.K., Lehtinen, K.E.J., Hämeri, K., Suresh, R., Sharma, V.P. and Kulmala, M., 2004. Relationship and variations of aerosol number and PM10 mass concentrations in a highly polluted urban environment—New Delhi, India. Atmospheric Environment, 38(3), pp.425-433.

Nilsson, E.D., Paatero, J. and Boy, M., 2001. Effects of air masses and synoptic weather on aerosol formation in the continental boundary layer. Tellus B, 53(4), pp.462-478.

Penttinen, P., Timonen, K.L., Tiittanen, P., Mirme, A., Ruuskanen, J. and Pekkanen, J., 2001. Ultrafine particles in urban air and respiratory health among adult asthmatics. European respiratory journal, 17(3), pp.428-435.

Petkova, E.P., Jack, D.W., Volavka-Close, N.H. and Kinney, P.L., 2013. Particulate matter pollution in African cities. Air Quality, Atmosphere & Health, 6(3), pp.603-614.

Pierce, J. and Adams, P., 2007. Efficiency of cloud condensation nuclei formation from ultrafine particles. Atmospheric Chemistry and Physics, 7(5), pp.1367-1379.

Rodríguez, S., Cuevas, E., González, Y., Ramos, R., Romero, P.M., Pérez, N., Querol, X. and Alastuey, A., 2008. Influence of sea breeze circulation and road traffic emissions on the relationship between particle number, black carbon, PM1, PM2. 5 and PM2. 5–10 concentrations in a coastal city. Atmospheric Environment, 42(26), pp.6523-6534.

Sánchez-Soberón, F., Rovira, J., Mari, M., Sierra, J., Nadal, M., Domingo, J.L. and Schuhmacher, M., 2015. Main components and human health risks assessment of PM10, PM2. 5, and PM1 in two areas influenced by cement plants. Atmospheric Environment, 120, pp.109-116.

Spracklen, D.V., Carslaw, K.S., Kulmala, M., Kerminen, V.M., Sihto, S.L., Riipinen, I., Merikanto, J., Mann, G.W., Chipperfield, M.P., Wiedensohler, A. and Birmili, W., 2008. Contribution of particle formation to global cloud condensation nuclei concentrations. Geophysical

Research Letters, 35(6).

Strak, M., Boogaard, H., Meliefste, K., Oldenwening, M., Zuurbier, M., Brunekreef, B. and Hoek, G., 2010. Respiratory health effects of ultrafine and fine particle exposure in cyclists. Occupational and environmental medicine, 67(2), pp.118-124.

Talbi, A., Kerchich, Y., Kerbachi, R. and Boughedaoui, M., 2018. Assessment of annual air pollution levels with PM1, PM2. 5, PM10 and associated heavy metals in Algiers, Algeria. Environmental Pollution, 232, pp.252-263.

Williamson, C.J., Kupc, A., Axisa, D., Bilsback, K.R., Bui, T., Campuzano-Jost, P., Dollner, M., Froyd, K.D., Hodshire, A.L., Jimenez, J.L. and Kodros, J.K., 2019. A large source of cloud condensation nuclei from new particle formation in the tropics. Nature, 574(7778), pp.399-403

Appendix B

```
import matplotlib.pyplot as plt
import pandas as pd
import numpy as np
import statistics
from statistics import mean

df=pd.read_csv()
Area =df['Area']
length = (Area.shape[0])
print("The number of particles is")
print(length)
diameter = np.sqrt((4*Area)/np.pi)
print('The max diameter is')
print(max(diameter))
print('The min diameter is')
print(min(diameter))
print('The mean diameter is')
print(mean(diameter))

bin0 = (sum(diameter <=1))
bin1 = (sum((diameter >1) & (diameter <= 2)))
bin2 = (sum((diameter >2) & (diameter <= 3)))
bin3 = (sum((diameter >3) & (diameter <= 4)))
bin4 = (sum((diameter >4) & (diameter <= 5)))
bin5 = (sum((diameter >5) & (diameter <= 6)))
bin6 = (sum((diameter >6) & (diameter <= 7)))
```

```
bin7 = (sum((diameter >7) & (diameter <= 8)))
bin8 = (sum((diameter >8) & (diameter <= 9)))
bin9 = (sum((diameter >9) & (diameter <= 10)))

list = [bin0, bin1, bin2, bin3, bin4, bin5, bin6, bin7, bin8, bin9]
print('The number of particle below ... value in each bin is')
print(list)
total_parts = sum(list)
print(total_parts)
X = [1, 2, 3, 4, 5, 6, 7, 8, 9,10]
Y = list[:]
plt.bar(X,Y, color=(0.2, 0.2, 0.6, 0.6), align= 'edge', width = -1, edgecolor
= "black")
plt.margins(x=0)
plt.ylim(0, 50)
plt.xlabel("Particle Size ($\mu m$)")
plt.ylabel("Number %")
plt.xticks([5,10])
plt.show()
```

Bibliography

Antoine, R., Lopez, T., Tanguy, M., Lissak, C., Gailler, L., Labazuy, P., and Fauchard, C. (2020). Geoscientists in the Sky: Unmanned Aerial Vehicles Responding to Geohazards. *Surveys in Geophysics*, 41(6):1285–1321.

Armienti, P., Macedonio, G., and Pareschi, M. T. (1988). A numerical model for simulation of tephra transport and deposition: applications to May 18, 1980, Mount St. Helens eruption. *Journal of Geophysical Research*, 93(B6):6463–6476.

Bagheri, G., Rossi, E., Biass, S., and Bonadonna, C. (2016). Timing and nature of volcanic particle clusters based on field and numerical investigations. *Journal of Volcanology and Geothermal Research*, 327:520–530.

Bandy, A. R., Maroulis, P. J., Wilner, L. A., and Torres, A. L. (1982). Estimates of the fluxes of NO, SO2, H2S, CS2 and OCS from Mt. St. Helens deduced from in situ plume concentration measurements. *Geophysical Research Letters*, 9(9):1097–1100.

Beckett, F., Rossi, E., Devenish, B., Witham, C., and Bonadonna, C. (2022). Modelling the size distribution of aggregated volcanic ash and implications for operational atmospheric dispersion modelling. *Atmospheric Chemistry and Physics*, 22(5):3409–3431.

Beckett, F. M., Witham, C. S., Hort, M. C., Stevenson, J. A., Bonadonna, C., and Millington, S. C. (2015). Sensitivity of dispersion model forecasts of volcanic ash clouds to the physical characteristics of the particles. *Journal of Geophysical Research*, 120(22):11,636–11,652.

Beckett, F. M., Witham, C. S., Leadbetter, S. J., Crocker, R., Webster, H. N., Hort, M. C., Jones, A. R., Devenish, B. J., and Thomson, D. J. (2020). Atmospheric dispersion modelling at the London VAAC: A review of developments since the 2010 eyjafjallajökull volcano ash cloud. *Atmosphere*, 11(4):352.

Bolić, T. and Sivčev, Ź. (2011). Eruption of Eyjafjallajökull in Iceland. *Transportation Research Record: Journal of the Transportation Research Board*, 2214(1):136–143.

Bonadonna, C., Genco, R., Gouhier, M., Pistolesi, M., Cioni, R., Alfano, F., Hoskuldsson, A., and Ripepe, M. (2011). Tephra sedimentation during the 2010 Eyjafjallajökull eruption (Iceland) from deposit, radar, and satellite observations. *Journal of Geophysical Research: Solid Earth*, 116(12):12202.

Bonali, F. L., Tibaldi, A., Marchese, F., Fallati, L., Russo, E., Corselli, C., and Savini, A. (2019). UAV-based surveying in volcano-tectonics: An example from the Iceland rift. *Journal of Structural Geology*, 121:46–64.

Brosch, E. (2022). Volcanic Ash and Small Uncrewed Aerial Vehicle (sUAV) Interaction: In-situ Observations and Laboratory Experiments on Aircraft Failure. *Frontiers in Earth Science*, 10.

Brown, R. J., Bonadonna, C., and Durant, A. J. (2012). A review of volcanic ash aggregation. *Physics and Chemistry of the Earth*, 45-46:65–78.

Budd, L., Griggs, S., Howarth, D., and Ison, S. (2011). A fiasco of volcanic proportions? Eyjafjallajökull and the closure of European airspace. *Mobilities*, 6(1):31–40.

Cadle, R. D., Lazrus, A., Huebert, B., Heidt, L., Rose, W., Woods, D., Chuan, R., Stoiber, R., Smith, D., and Zielinski, R. (1979). Atmospheric implications of studies of Central American volcanic eruption clouds. *Journal of Geophysical Research*, 84(C11):6961–6968.

Carey, S. N. and Sigurdsson, H. (1982). Influence of particle aggregation on deposition of distal tephra from the May 18, 1980, eruption of Mount St. Helens volcano. *Journal of Geophysical Research*, 87(B8):7061–7072.

Casadevall, T. J. (1994). The 1989-1990 eruption of Redoubt Volcano, Alaska: impacts on aircraft operations. *Journal of Volcanology and Geothermal Research*, 62(1-4):301–316.

Chaharlang, R., Hajjari, E., Baghal, S. M., and Siahpoosh, M. (2019). Premature damage of the second stage nozzle guide vanes of a gas turbine made of Inconel 738LC. *Engineering Failure Analysis*, 105:803–816.

Christmann, C., Nunes, R., Schmitt, A., and Guffanti, M. (2017). Flying into volcanic ash clouds: an evaluation of hazard potential. *The North Atlantic Treaty Organization, Vilnius, Lithuania*, page 1028.

Chuan, R. L., Woods, D. C., and Mccormick, M. P. (1981). Characterization of aerosols from eruptions of Mount St. Helens. *Science*, 211(4484):830–832.

Civil Aviation Authority (2015). Managing ash in UK airspace.

Civil Aviation Authority (2023). Introduction to drone flying and the UK rules.

Clarkson, R. and Simpson, H. (2017). Maximising Airspace Use During Volcanic Eruptions: Matching Engine Durability against Ash Cloud Occurrence. *Proceedings of the NATO STO AVT-272 Specialists Meeting on: Impact of Volcanic Ash Clouds on Military Operations, Vilnius, Lithuania*, pages 15–17.

Clarkson, R. J., Majewicz, E. J., and Mack, P. (2016). A re-evaluation of the 2010 quantitative understanding of the effects volcanic ash has on gas turbine engines. *Proceedings of the Institution of Mechanical Engineers, Part G: Journal of Aerospace Engineering*, 230(12):2274–2291.

Cornell, W., Carey, S., and Sigurdsson, H. (1983). Computer simulation of transport and deposition of the campanian Y-5 ash. *Journal of Volcanology and Geothermal Research*, 17(1-4):89–109.

Dacre, H. F., Grant, A. L., and Johnson, B. T. (2013). Aircraft observations and model simulations of concentration and particle size distribution in the Eyjafjallajökull volcanic ash cloud. *Atmospheric Chemistry and Physics*, 13(3):1277–1291.

David, T., Hine, D., Schellenberg, B., Goudarzi, H., Rendall, T., Wood, K., Bolós-Fernández, J., and Richardson, T. (2021). Cascade open aircraft project: University of bristol vtol drone development. In *AIAA Scitech 2021 Forum*, pages 1–18.

Davison, C. R. and Rutke, T. A. (2014). Assessment and characterization of volcanic ash threat to gas turbine engine performance. *Journal of Engineering for Gas Turbines and Power*, 136(8).

De Beni, E., Cantarero, M., and Messina, A. (2019). UAVs for volcano monitoring: A new approach applied on an active lava flow on Mt. Etna (Italy), during the 27 February–02 March 2017 eruption. *Journal of Volcanology and Geothermal Research*, 369:250–262.

De Wagter, C., Ruijsink, R., Smeur, E. J., van Hecke, K. G., van Tienen, F., van der Horst, E., and Remes, B. D. (2018). Design, control, and visual navigation of the DelftaCopter VTOL tail-sitter UAV. *Journal of Field Robotics*, 35(6):937–960.

Dellino, P., Gudmundsson, M. T., Larsen, G., Mele, D., Stevenson, J. A., Thordarson, T., and Zimanowski, B. (2012). Ash from the Eyjafjallajökull eruption (Iceland): Fragmentation processes and aerodynamic behavior. *Journal of Geophysical Research: Solid Earth*, 117(1):0–04.

Devenish, B. J., Francis, P. N., Johnson, B. T., Sparks, R. S., and Thomson, D. J. (2012). Sensitivity analysis of dispersion modeling of volcanic ash from Eyjafjallajökull in May 2010. *Journal of Geophysical Research Atmospheres*, 117(6).

Dunn, M. G. (2012). Operation of gas turbine engines in an environment contaminated with volcanic ash. *Journal of Turbomachinery*, 134(5).

Durant, A. J. (2015). Toward a realistic formulation of fine-ash lifetime in volcanic clouds. *Geology*, 43(3):271–272.

Eliasson, J., Watson, I. M., and Weber, K. (2016). In Situ Observations of Airborne Ash From Manned Aircraft. In *Volcanic Ash: Hazard Observation*, pages 89–98. Elsevier.

Farlow, N. H., Oberbeck, V. R., Snetsinger, K. G., Ferry, G. V., Polkowski, G., and Hayes, D. M. (1981). Size distributions and mineralogy of ash particles in the stratosphere from eruptions of Mount St. Helens. *Science*, 211(4484):832–834.

Flynn, I. T. and Ramsey, M. S. (2020). Pyroclastic density current hazard assessment and modeling uncertainties for Fuego volcano, Guatemala. *Remote Sensing*, 12(17).

Folch, A. (2012). A review of tephra transport and dispersal models: Evolution, current status, and future perspectives. *Journal of Volcanology and Geothermal Research*, 235-236:96–115.

Freret-Lorgeril, V., Donnadieu, F., Eychenne, J., Soriaux, C., and Latchimy, T. (2019). In situ terminal settling velocity measurements at Stromboli volcano: Input from physical characterization of ash. *Journal of Volcanology and Geothermal Research*, 374:62–79.

Giehl, C., Brooker, R. A., Marxer, H., and Nowak, M. (2017). An experimental simulation of volcanic ash deposition in gas turbines and implications for jet engine safety. *Chemical Geology*, 461:160–170.

Gislason, S. R., Hassenkam, T., Nedel, S., Bovet, N., Eiriksdottir, E. S., Alfredsson, H. A., Hem, C. P., Balogh, Z. I., Dideriksen, K., Oskarsson, N., Sigfusson, B., Larsen, G., and Stipp, S. L. (2011). Characterization of Eyjafjallajökull volcanic ash particles and a protocol for rapid risk assessment. *Proceedings of the National Academy of Sciences of the United States of America*, 108(18):7307–7312.

Gordon, K. D., Cole, J. W., Rosenberg, M. D., and Johnston, D. M. (2005). Effects of volcanic ash on computers and electronic equipment. *Natural Hazards*, 34(2):231–262.

Gudmundsson, M. T., Pedersen, R., Vogfjörd, K., Thorbjarnardóttir, B., Jakobsdóttir, S., and Roberts, M. J. (2010). Eruptions of Eyjafjallajökull Volcano, Iceland. *Eos, Transactions American Geophysical Union*, 91(21):190.

Guffanti, M., Casadevall, T. J., and Budding, K. (2011). Encounters of aircraft with volcanic ash clouds: A compilation of known incidents, 1953-2009. In *The Threat of Volcanic Ash to Aviation*, pages 17–39.

Guffanti, M., Mayberry, G. C., Casadevall, T. J., and Wunderman, R. (2009). Volcanic hazards to airports. In *Natural Hazards*, volume 51, pages 287–302.

Guffanti, M. and Tupper, A. (2015). Volcanic Ash Hazards and Aviation Risk. In *Volcanic Hazards, Risks and Disasters*, pages 87–108. Elsevier.

Harvey, N. J., Huntley, N., Dacre, H. F., Goldstein, M., Thomson, D., and Webster, H. (2018). Multi-level emulation of a volcanic ash transport and dispersion model to quantify sensitivity to uncertain parameters. *Natural Hazards and Earth System Sciences*, 18(1):41–43.

Hirtl, M., Arnold, D., Baro, R., Brenot, H., Coltelli, M., Eschbacher, K., Hard-Stremayer, H., Lipok, F., Maurer, C., Meinhard, D., Mona, L., D. Mulder, M., Papagiannopoulos, N.,

Pernsteiner, M., Plu, M., Robertson, L., Roki, K., Scherllin-Pirscher, B., Sievers, K., Sofiev, M., Som De Cerff, W., Steinheimer, M., Stuefer, M., Theys, N., Uppstu, A., Wagenaar, S., Winkler, R., Wotawa, G., Zobl, F., and Zopp, R. (2020). A volcanic-hazard demonstration exercise to assess and mitigate the impacts of volcanic ash clouds on civil and military aviation. *Natural Hazards and Earth System Sciences*, 20(6):1719–1739.

Hornby, A., Gazel, E., Bush, C., Dayton, K., and Mahowald, N. (2023). Phases in fine volcanic ash. *Scientific Reports*, 13(1).

Horwell, C. J. (2007). Grain-size analysis of volcanic ash for the rapid assessment of respiratory health hazard. *Journal of Environmental Monitoring*, 9(10):1107–1115.

Hufford, G. L., Salinas, L. J., Simpson, J. J., Barske, E. G., and Pieri, D. C. (2000). Operational implications of airborne volcanic ash. *Bulletin of the American Meteorological Society*, 81(4):745–755.

Igarashi, Y., Girina, O., Osiensky, J., and Moore, D. (2018). International Coordination in Managing Airborne Ash Hazards: Lessons from the Northern Pacific. In *Advances in Volcanology*, pages 529–547.

James, M. R., Carr, B. B., D'Arcy, F., Diefenbach, A. K., Dietterich, H. R., Fornaciai, A., Lev, E., Liu, E. J., Pieri, D. C., Rodgers, M., Smets, B., Terada, A., von Aulock, F. W., Walter, T. R., Wood, K. T., and Zorn, E. U. (2020). Volcanological applications of unoccupied aircraft systems (UAS): Developments, strategies, and future challenges. *Volcanica*, 3(1):64–114.

James, M. R., Lane, S. J., and Gilbert, J. S. (2003). Density, construction, and drag coefficient of electrostatic volcanic ash aggregates. *Journal of Geophysical Research: Solid Earth*, 108(B9):2435.

Johnson, B., Turnbull, K., Brown, P., Burgess, R., Dorsey, J., Baran, A. J., Webster, H., Haywood, J., Cotton, R., Ulanowski, Z., Hesse, E., Woolley, A., and Rosenberg, P. (2012). In situ observations of volcanic ash clouds from the FAAM aircraft during the eruption of Eyjafjallajökull in 2010. *Journal of Geophysical Research Atmospheres*, 117(8).

Johnson, R. W. and Casadevall, T. J. (1994). Aviation safety and volcanic ash clouds in the Indonesia-Australia region. In *Volcanic ash and aviation safety: Proceedings of the First*

International Symposium on Volcanic Ash and Aviation Safety, pages 191–197. US Geological Survey Bulletin 2047.

Johnston, S. J., Basford, P. J., Bulot, F. M., Apetroaie-Cristea, M., Easton, N. H., Davenport, C., Foster, G. L., Loxham, M., Morris, A. K., and Cox, S. J. (2019). City scale particulate matter monitoring using LoRaWAN based air quality IoT devices. *Sensors*, 19(1):209.

Jones, A. (2004). Atmospheric dispersion modelling at the Met Office. *Weather*, 59(11):311–316.

Jones, A., Thomson, D., Hort, M., and Devenish, B. (2007). The U.K. Met Office's Next-Generation Atmospheric Dispersion Model, NAME III. In *Air Pollution Modeling and Its Application XVII*, pages 580–589.

Jordan, B. R. (2019). Collecting field data in volcanic landscapes using small UAS (sUAS)/drones. *Journal of Volcanology and Geothermal Research*, 385:231–241.

Kazahaya, R., Shinohara, H., Ohminato, T., and Kaneko, T. (2019). Airborne measurements of volcanic gas composition during unrest at Kuchinoerabujima volcano, Japan. *Bulletin of Volcanology*, 81(2).

Kienle, T., Dean, K. G., Garbeil, H., and Rose, W. I. (1990). Satellite surveillance of volcanic ash plumes, application to aircraft safety. *Eos, Transactions American Geophysical Union*, 71(7):266.

Langmann, B., Folch, A., Hensch, M., and Matthias, V. (2012). Volcanic ash over Europe during the eruption of Eyjafjallajökull on Iceland, April-May 2010. *Atmospheric Environment*, 48:1–8.

Lathem, T. L., Kumar, P., Nenes, A., Dufek, J., Sokolik, I. N., Trail, M., and Russell, A. (2011). Hygroscopic properties of volcanic ash. *Geophysical Research Letters*, 38(11).

Liang, Y. and Xu, J. (2021). The impact of volcanic ash on the safety of aviation industry: Review of China's current situation. In *Geological Society Special Publication*, volume 510, pages 253–262. Geological Society of London.

Liu, E. J., Cashman, K. V., Miller, E., Moore, H., Edmonds, M., Kunz, B. E., Jenner, F., and Chigna, G. (2020). Petrologic monitoring at Volcán de Fuego, Guatemala. *Journal of Volcanology and Geothermal Research*, 405:107044.

Liu, E. J., Cashman, K. V., and Rust, A. C. (2015). Optimising shape analysis to quantify volcanic ash morphology. *GeoResJ*, 8:14–30.

Liu, E. J., Wood, K., Mason, E., Edmonds, M., Aiuppa, A., Giudice, G., Bitetto, M., Francofonte, V., Burrow, S., Richardson, T., Watson, M., Pering, T. D., Wilkes, T. C., McGonigle, A. J., Velasquez, G., Melgarejo, C., and Bucarey, C. (2019). Dynamics of Outgassing and Plume Transport Revealed by Proximal Unmanned Aerial System (UAS) Measurements at Volcán Villarrica, Chile. *Geochemistry, Geophysics, Geosystems*, 20(2):730–750.

Lyons, J. J., Waite, G. P., Rose, W. I., and Chigna, G. (2010). Patterns in open vent, strombolian behavior at Fuego volcano, Guatemala, 2005-2007. *Bulletin of Volcanology*, 72(1):1–15.

Macleod, J., Wood, K., Rendall, T., Watson, M., Allen, C., Reader, M., Lucas, J., and Richardson, T. (2022). Design of a collector for sampling volcanic ash using unmanned aerial systems. *Journal of Aerosol Science*, 169:106119.

Masic, A., Bibic, D., Pikula, B., Blazevic, A., Huremovic, J., and Zero, S. (2020). Evaluation of optical particulate matter sensors under realistic conditions of strong and mild urban pollution. *Atmospheric Measurement Techniques*, 13(12):6427–6443.

Mastin, L., Pavolonis, M., Engwell, S., Clarkson, R., Witham, C., Brock, G., Lisk, I., Guffanti, M., Tupper, A., Schneider, D., Beckett, F., Casadevall, T., and Rennie, G. (2022). Progress in protecting air travel from volcanic ash clouds. *Bulletin of Volcanology*, 84(1):1–9.

Mastin, L. G., Guffanti, M., Servranckx, R., Webley, P., Barsotti, S., Dean, K., Durant, A., Ewert, J. W., Neri, A., Rose, W. I., Schneider, D., Siebert, L., Stunder, B., Swanson, G., Tupper, A., Volentik, A., and Waythomas, C. F. (2009). A multidisciplinary effort to assign realistic source parameters to models of volcanic ash-cloud transport and dispersion during eruptions. *Journal of Volcanology and Geothermal Research*, 186(1-2):10–21.

Mazzocchi, M., Hansstein, F., and Ragona, M. (2010). The 2010 volcanic ash cloud and its financial impact on the European airline industry. *CESifo Forum*, 11(2):92–100.

McConville, A. and Richardson, T. (2023). High-altitude vertical wind profile estimation using multirotor vehicles. *Frontiers in Robotics and AI*, 10:1112889.

McGonigle, A. J., Aiuppa, A., Giudice, G., Tamburello, G., Hodson, A. J., and Gurrieri, S. (2008). Unmanned aerial vehicle measurements of volcanic carbon dioxide fluxes. *Geophysical Research Letters*, 35(6).

Millington, S. C., Saunders, R. W., Francis, P. N., and Webster, H. N. (2012). Simulated volcanic ash imagery: A method to compare NAME ash concentration forecasts with SEVIRI imagery for the Eyjafjallajkull eruption in 2010. *Journal of Geophysical Research Atmospheres*, 117(5):0–17.

Mock, J. C., Johnson, J. B., Pineda, A., Bejar, G., and Roca, A. (2023). UAV-Based Quantification of Dynamic Lahar Channel Morphology at Volcán de Fuego, Guatemala. *Remote Sensing*, 15(15):3713.

Mueller, S. B., Ayris, P. M., Wadsworth, F. B., Kueppers, U., Casas, A. S., Delmelle, P., Taddeucci, J., Jacob, M., and DIngwell, D. B. (2017). Ash aggregation enhanced by deposition and redistribution of salt on the surface of volcanic ash in eruption plumes. *Scientific Reports*, 7:45762.

Mueller, S. B., Kueppers, U., Ayris, P. M., Jacob, M., and Dingwell, D. B. (2016). Experimental volcanic ash aggregation: Internal structuring of accretionary lapilli and the role of liquid bonding. *Earth and Planetary Science Letters*, 433:232–240.

Müller, D., Hess, K. U., Kueppers, U., Lokachari, S., Dingwell, D. B., Wolf, G., Rokicki, P., and Nowotnik, A. (2021a). Rheological and chemical interaction between volcanic ash and thermal barrier coatings. *Surface and Coatings Technology*, 412:127049.

Müller, D., Hess, K. U., Kueppers, U., Lokachari, S., Dingwell, D. B., Wolf, G., Rokicki, P., and Nowotnik, A. (2021b). Rheological and chemical interaction between volcanic ash and thermal barrier coatings. *Surface and Coatings Technology*, 412:127049.

Naismith, A. K., Matthew Watson, I., Escobar-Wolf, R., Chigna, G., Thomas, H., Coppola, D., and Chun, C. (2019). Eruption frequency patterns through time for the current (1999–2018) activity cycle at Volcán de Fuego derived from remote sensing data: Evidence for an accelerating cycle of explosive paroxysms and potential implications of eruptive activity. *Journal of Volcanology and Geothermal Research*, 371:206–219.

Nguyen, N. H., Nguyen, H. X., Le, T. T. B., and Vu, C. D. (2021). Evaluating Low-Cost Commercially Available Sensors for Air Quality Monitoring and Application of Sensor Calibration Methods for Improving Accuracy. *Open Journal of Air Pollution*, 10(01):1–17.

Ohminato, T., Kaneko, T., Koyama, T., Watanabe, A., Kanda, W., Tameguri, T., and Kazahaya, R. (2017). Observations using an unmanned aerial vehicle in an area in danger of volcanic eruptions at Kuchinoerabu-jima Volcano, southern Kyushu, Japan. *Journal of Natural Disaster Science*, 38(1):85–104.

Osman, S., Beckett, F., Rust, A., and Snee, E. (2020). Sensitivity of volcanic ash dispersion modelling to input grain size distribution based on hydromagmatic and magmatic deposits. *Atmosphere*, 11(6).

Pearson, D. and Brooker, R. (2020). The accumulation of molten volcanic ash in jet engines; simulating the role of magma composition, ash particle size and thermal barrier coatings. *Journal of Volcanology and Geothermal Research*, 389:106707.

Pering, T. D., Liu, E. J., Wood, K., Wilkes, T. C., Aiuppa, A., Tamburello, G., Bitetto, M., Richardson, T., and McGonigle, A. J. (2020). Combined ground and aerial measurements resolve vent-specific gas fluxes from a multi-vent volcano. *Nature Communications*, 11(1).

Petersen, G. N. (2010). A short meteorological overview of the Eyjafjallajökull eruption 14 April-23 May 2010. *Weather*, 65(8):203–207.

Pieri, D., Diaz, J. A., Bland, G., Fladeland, M., Madrigal, Y., Corrales, E., Alegria, O., Alan, A., Realmuto, V., Miles, T., and Abtahi, A. (2013). In situ observations and sampling of volcanic emissions with NASA and UCR unmanned aircraft, including a case study at turrialba volcano, Costa rica. *Geological Society Special Publication*, 380(1):321–352.

Poulidis, A. P., Phillips, J. C., Renfrew, I. A., Barclay, J., Hogg, A., Jenkins, S. F., Robertson, R., and Pyle, D. M. (2018). Meteorological Controls on Local and Regional Volcanic Ash Dispersal. *Scientific Reports*, 8(1).

Prata, A. J. and Tupper, A. (2009). Aviation hazards from volcanoes: The state of the science. *Natural Hazards*, 51(2):239–244.

Prata, F. and Rose, B. (2015). Volcanic ash hazards to aviation. In *The Encyclopedia of Volcanoes*, pages 911–934. Academic Press.

Przedpelski, Z. J. and Casadevall, T. J. (1994). VOLCANIC ASH AND AVIATION SAFETY. In *Volcanic Ash and Aviation Safety: Proceedings of the First International Symposium on Volcanic Ash and Aviation Safety*, number 2047, page 129. US Government Printing Office.

Reichardt, U., Ulfarsson, G. F., and Pétursdóttir, G. (2018). Volcanic ash and aviation: Recommendations to improve preparedness for extreme events. *Transportation Research Part A: Policy and Practice*, 113:101–113.

Riley, C. M., Rose, W. I., and Bluth, G. J. S. (2003). Quantitative shape measurements of distal volcanic ash. *Journal of Geophysical Research: Solid Earth*, 108(B10):2504.

Rolls Royce (1996). Rolls Royce - The Jet Engine (5th edition).

Rose, W. I., Cadle, R. D., Heidt, L. E., Friedman, I., Lazrus, A. L., and Huebert, B. J. (1980). Gas and hydrogen isotopic analyses of volcanic eruption clouds in Guatemala sampled by aircraft. *Journal of Volcanology and Geothermal Research*, 7(1-2):1–10.

Rose, W. I. and Durant, A. J. (2011). Fate of volcanic ash: Aggregation and fallout. *Geology*, 39(9):895–896.

Rose, W. I., Self, S., Murrow, P. J., Bonadonna, C., Durant, A. J., and Ernst, G. G. (2008). Nature and significance of small volume fall deposits at composite volcanoes: Insights from the October 14, 1974 Fuego eruption, Guatemala. *Bulletin of Volcanology*, 70(9):1043–1067.

Rossi, E., Bagheri, G., Beckett, F., and Bonadonna, C. (2021). The fate of volcanic ash: premature or delayed sedimentation? *Nature Communications 2021 12:1*, 12(1):1–9.

Saxby, J., Beckett, F., Cashman, K., Rust, A., and Tennant, E. (2018). The impact of particle shape on fall velocity: Implications for volcanic ash dispersion modelling. *Journal of Volcanology and Geothermal Research*, 362:32–48.

Saxby, J., Rust, A., Beckett, F., Cashman, K., and Rodger, H. (2020a). Estimating the 3D shape of volcanic ash to better understand sedimentation processes and improve atmospheric dispersion modelling. *Earth and Planetary Science Letters*, 534.

Saxby, J., Rust, A., Cashman, K., and Beckett, F. (2020b). The importance of grain size and shape in controlling the dispersion of the Vedde cryptotephra. *Journal of Quaternary Science*, 35(1-2):175–185.

Sayahi, T., Butterfield, A., and Kelly, K. E. (2019). Long-term field evaluation of the Plantower PMS low-cost particulate matter sensors. *Environmental Pollution*, 245:932–940.

Schellenberg, B., Richardson, T., Richards, A., Clarke, R., and Watson, M. (2019a). On-Board Real-Time Trajectory Planning for Fixed Wing Unmanned Aerial Vehicles in Extreme Environments. *Sensors*, 19(19):4085.

Schellenberg, B., Richardson, T., Watson, M., Greatwood, C., Clarke, R., Thomas, R., Wood, K., Freer, J., Thomas, H., Liu, E., Salama, F., and Chigna, G. (2019b). Remote sensing and identification of volcanic plumes using fixed-wing UAVs over Volcán de Fuego, Guatemala. *Journal of Field Robotics*, 36(7):1192–1211.

Schmitt, A. R. and Kuenz, A. (2015). A reanalysis of aviation effects from volcano eruption of Eyjafjallajökull in 2010. In *AIAA/IEEE Digital Avionics Systems Conference - Proceedings*, pages 1B31–1B37. Institute of Electrical and Electronics Engineers Inc.

Schumann, U., Weinzierl, B., Reitebuch, O., Schlager, H., Minikin, A., Forster, C., Baumann, R., Sailer, T., Graf, K., Mannstein, H., Voigt, C., Rahm, S., Simmet, R., Scheibe, M., Lichtenstern, M., Stock, P., Rüba, H., Scauble, D., Tafferner, A., Rautenhaus, M., Gerz, T., Ziereis, H., Krautstrunk, M., Mallaun, C., Gayet, J. F., Lieke, K., Kandler, K., Ebert, M., Weinbruch, S., Stohl, A., Gasteiger, J., Gro, S., Freudenthaler, V., Wiegner, M., Ansmann, A., Tesche, M., Olafsson, H., and Sturm, K. (2011). Airborne observations of the Eyjafjalla volcano ash cloud over Europe during air space closure in April and May 2010. *Atmospheric Chemistry and Physics*, 11(5):2245–2279.

Simmel, M., Diehl, K., and Wurzler, S. (2005). Numerical simulation of the microphysics of an orographic cloud: Comparison with measurements and sensitivity studies. *Atmospheric Environment*, 39(23-24):4365–4373.

Simon, D. L., Csank, J., and Rinehart, A. (2015). Vehicle Integrated Propulsion Research (VIPR) Gas Path Diagnostics and Volcanic Ash Ingestion Test Results. Technical report.

Song, W., Lavallee, Y., Hess, K. U., Kueppers, U., Cimarelli, C., and Dingwell, D. B. (2016). Volcanic ash melting under conditions relevant to ash turbine interactions. *Nature Communications*, 7.

Song, W., Yang, S., Fukumoto, M., Lavallée, Y., Lokachari, S., Guo, H., You, Y., and Dingwell, D. B. (2019). Impact interaction of in-flight high-energy molten volcanic ash droplets with jet engines. *Acta Materialia*, 171:119–131.

Sorem, R. K. (1982). Volcanic ash clusters: Tephra rafts and scavengers. *Journal of Volcanology and Geothermal Research*, 13(1-2):63–71.

Stix, J., de Moor, J. M., Rüdiger, J., Alan, A., Corrales, E., D'Arcy, F., Diaz, J. A., and Liotta, M. (2018). Using Drones and Miniaturized Instrumentation to Study Degassing at Turrialba and Masaya Volcanoes, Central America. *Journal of Geophysical Research: Solid Earth*, 123(8):6501–6520.

Stohl, A., Prata, A. J., Eckhardt, S., Clarisse, L., Durant, A., Henne, S., Kristiansen, N. I., Minikin, A., Schumann, U., Seibert, P., Stebel, K., Thomas, H. E., Thorsteinsson, T., Tørseth, K., and Weinzierl, B. (2011). Determination of time-and height-resolved volcanic ash emissions and their use for quantitative ash dispersion modeling: The 2010 Eyjafjallajökull eruption. *Atmospheric Chemistry and Physics*, 11(9):4333–4351.

Telling, J., Dufek, J., and Shaikh, A. (2013). Ash aggregation in explosive volcanic eruptions. *Geophysical Research Letters*, 40(10):2355–2360.

Terada, A., Morita, Y., Hashimoto, T., Mori, T., Ohba, T., Yaguchi, M., and Kanda, W. (2018). Water sampling using a drone at Yugama crater lake, Kusatsu-Shirane volcano, Japan. *Earth, Planets and Space*, 70(1).

Terkildsen, K. H., Schultz, U. P., and Jensen, K. (2021). Safely Flying BVLOS in the EU with an Unreliable UAS. In *2021 International Conference on Unmanned Aircraft Systems, ICUAS 2021*, pages 591–601.

Tmušić, G., Manfreda, S., Aasen, H., James, M. R., Gonçalves, G., Ben-Dor, E., Brook, A., Polinova, M., Arranz, J. J., Mészáros, J., Zhuang, R., Johansen, K., Malbeteau, Y., de Lima, I. P., Davids, C., Herban, S., and McCabe, M. F. (2020). Current practices in UAS-based environmental monitoring. *Remote Sensing*, 12(6).

Turnbull, K., Johnson, B., Marenco, F., Haywood, J., Minikin, A., Weinzierl, B., Schlager, H., Schumann, U., Leadbetter, S., and Woolley, A. (2012). A case study of observations of

volcanic ash from the Eyjafjallajökull eruption: 1. in situ airborne observations. *Journal of Geophysical Research Atmospheres*, 117(3).

Twohy, C. H., Coakley, J. A., and Tahnk, W. R. (2009). Effect of changes in relative humidity on aerosol scattering near clouds. *Journal of Geophysical Research Atmospheres*, 114(5).

Ulfarsson, G. F. and Unger, E. A. (2011). Impacts and Responses of Icelandic Aviation to the 2010 Eyjafjallajökull Volcanic Eruption. *Transportation Research Record: Journal of the Transportation Research Board*, 2214(1):144–151.

Van Eaton, A. R., Muirhead, J. D., Wilson, C. J., and Cimarelli, C. (2012). Growth of volcanic ash aggregates in the presence of liquid water and ice: An experimental approach. *Bulletin of Volcanology*, 74(9):1963–1984.

Vecino, M. C., Rossi, E., Freret-Lorgeril, V., Fries, A., Gabellini, P., Lemus, J., Pollastri, S., Poulidis, A. P., Iguchi, M., and Bonadonna, C. (2022). Aerodynamic characteristics and genesis of aggregates at Sakurajima Volcano, Japan. *Scientific Reports*, 12(1):2044.

Vogel, A., Diplas, S., Durant, A. J., Azar, A. S., Sunding, M. F., Rose, W. I., Sytchkova, A., Bonadonna, C., Krüger, K., and Stohl, A. (2017). Reference data set of volcanic ash physicochemical and optical properties. *Journal of Geophysical Research: Atmospheres*, 122(17):9485–9514.

Wakeford, Z. E., Chmielewska, M., Hole, M. J., Howell, J. A., and Jerram, D. A. (2019). Combining thermal imaging with photogrammetry of an active volcano using UAV: an example from Stromboli, Italy. *Photogrammetric Record*, 34(168):445–466.

Wallace, K. L., Schaefer, J. R., and Coombs, M. L. (2013). Character, mass, distribution, and origin of tephra-fall deposits from the 2009 eruption of Redoubt Volcano, Alaska-Highlighting the significance of particle aggregation. *Journal of Volcanology and Geothermal Research*, 259:145–169.

Wang, Z., Delp, W. W., and Singer, B. C. (2020). Performance of low-cost indoor air quality monitors for PM2.5 and PM10 from residential sources. *Building and Environment*, 171:106654.

Waythomas, C. F., Dorava, J. M., Miller, T. P., Neal, C. A., and McGimsey, R. G. (1997). Preliminary volcano-hazard assessment for Redoubt Volcano, Alaska. Technical report, US Geological Survey.

Weber, K., Eliasson, J., Vogel, A., Fischer, C., Pohl, T., van Haren, G., Meier, M., Grobéty, B., and Dahmann, D. (2012). Airborne in-situ investigations of the Eyjafjallajökull volcanic ash plume on iceland and over north-western Germany with light aircrafts and optical particle counters. *Atmospheric Environment*, 48:9–21.

Webley, P. and Mastin, L. (2009). Improved prediction and tracking of volcanic ash clouds. *Journal of Volcanology and Geothermal Research*, 186(1-2):1–9.

Weinzierl, B., Sauer, D., Minikin, A., Reitebuch, O., Dahlkötter, F., Mayer, B., Emde, C., Tegen, I., Gasteiger, J., Petzold, A., Veira, A., Kueppers, U., and Schumann, U. (2012). On the visibility of airborne volcanic ash and mineral dust from the pilot's perspective in flight. *Physics and Chemistry of the Earth*, 45-46:87–102.

Wilkins, K. L., Watson, I. M., Kristiansen, N. I., Webster, H. N., Thomson, D. J., Dacre, H. F., and Prata, A. J. (2016). Using data insertion with the NAME model to simulate the 8 May 2010 Eyjafjallajökull volcanic ash cloud. *Journal of Geophysical Research*, 121(1):306–323.

Wilson, G., Wilson, T., Cole, J., and Oze, C. (2012). Vulnerability of laptop computers to volcanic ash and gas. *Natural Hazards*, 63(2):711–736.

Witham, C., Hort, M., Thomson, D., Leadbetter, S., Devenish, B., Webster, H., Beckett, F., and Kristiansen, N. (2012). The current volcanic ash modelling setup at the London VAAC. *UK Meteorological Office Internal Report*.

Witham, C. S., Hort, M. C., Potts, R., Servranckx, R., Husson, P., and Bonnardot, F. (2007). Comparison of VAAC atmospheric dispersion models using the 1 November 2004 Grimsvötn eruption. *Meteorological Applications*, 14(1):27–38.

Wood, K., Richardson, T., Schellenberg, B., Greatwood, C., Watson, M., Thomas, H., Naismtih, A., Liu, E., Freer, J., Thomas, R., and Chigna, G. (2018). UAV based detection and measurement of volcanic plumes at Volcán de Fuego, Guatemala. Technical report.

Woodhouse, M. J., Hogg, A. J., Phillips, J. C., and Sparks, R. S. (2013). Interaction between volcanic plumes and wind during the 2010 Eyjafjallajökull eruption, Iceland. *Journal of Geophysical Research: Solid Earth*, 118(1):92–109.